Scales of variability of atmospheric aerosols

Natalie Weigum

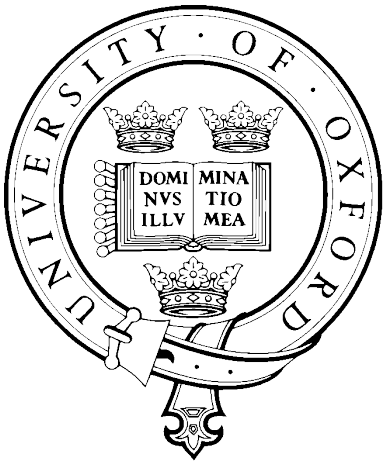

Submitted for the degree of Doctor of Philosophy in Physics
Michaelmas Term 2014

Atmospheric, Oceanic and Planetary Physics
Department of Physics
University of Oxford

Scales of variability of atmospheric aerosols

Natalie Weigum, Lincoln College
Submitted for the degree of Doctor of Philosophy in Physics, Michaelmas Term 2014

Abstract

Aerosols have a significant effect on the global radiation budget through their interactions with radiation and clouds. However, estimates of their effect are the dominant source of uncertainty in current estimates of total anthropogenic effect on climate. A major cause of this uncertainty is the high degree of variability of aerosol properties and processes that affect their lifetime. Prediction of the aerosol effect on climate depends on the ability of three-dimensional numerical models to accurately estimate aerosol properties. However, a limitation of traditional grid-based models is their inability to resolve variability on scales smaller than a grid box. Past research has shown that significant aerosol variability exists on scales smaller than these grid-boxes, which can lead to discrepancies between observations and aerosol models.

This thesis uses a synthesis of aerosol observations, global climate model (GCM) data, and a new aerosol modelling technique implemented within a regional-scale model to quantify the important scales of aerosol variability and the extent to which different sub-grid scale processes contribute to discrepancies in aerosol modelling.

Analysis of black carbon (BC) plumes from aircraft observations shows that BC plumes represent a large portion of total BC mass and typically exist on scales of 65–100 km. Comparison of observed plume scales to those simulated by GCMs at multiple resolutions show that GCMs overestimate the scales of along-flight-track variability by 64% at the highest resolution. Variability is shown to be greater near sources than in remote regions, indicating that models may benefit from higher resolutions in regions of high emissions. Additionally, GCMs at all resolutions show higher variability in the latitudinal direction than the longitudinal direction, suggesting that capturing latitudinal variability may result in greater improvements in aerosol modelling.

This work additionally presents a novel technique to allow one to isolate the effect of aerosol variability from other sources of variability within the model. Processes most affected by neglecting aerosol sub-grid variability are gas-phase chemistry and aerosol uptake of water through the aerosol/gas equilibrium reactions. The inherent non-linearities in these processes result in large changes in aerosol parameters when aerosol and gaseous species are artificially mixed over large spatial scales. These changes in aerosol and gas concentrations are exaggerated by convective transport, which transports these altered concentrations to altitudes where their effect is more pronounced. Future aerosol model development should focus on accounting for the effect of sub-grid variability on these processes at global scales in order to improve model predictions of the aerosol effect on climate.

Acknowledgements

There are many people who deserve to be acknowledged for their contribution to this thesis, whether it was through specific input and guidance or indirectly through their support. Although I cannot name everyone, I would like to mention a few people for whom I am extremely grateful.

Firstly, I would like to thank my supervisor, Philip Stier. He has not only provided an abundance of supervisory guidance over the years, but has also taught me how to critically evaluate my own research. I always appreciated his willingness to meet with me whenever necessary and his detailed feedback!

I would also like to thank Nick Schutgens, who acted as a post-doctoral supervisor and performed several model simulations on my behalf. My numerous visits to his office were necessary for both the completion of this thesis and the maintenance of my sanity. I would like to thank Zak Kipling, who also performed model simulations on my behalf and who was always willing to help me when I encountered computational ineptitude. This acknowledgement section would certainly not be complete without thanking my officemate of three years, Ed Gryspeerdt. He was always willing to act as a sounding board for ideas/frustration, a distraction from stress, and a friend. My final year without him just wasn't the same! I would also like to thank the other members of our group for their input over the years: Sarah Taylor, Bethan White, Dan Partridge, Laurent Labbouz, Rosalind West, and Til Wagner. Thanks to Lucy, Jane, Andy, and James for their coffee time chats and post-work pub trips.

The administration staff in both my department and my college have been invaluable, with a special thanks to Sarah Harrington and Carmella Elan-Gaston.

Outside of the department, I was fortunate to have family and friends both near and far to support me through my PhD. Thanks to my Lincoln crew — Lizzie, Jackie, Mo, and Bostrom — for sticking it out with me; Seana for always providing the best advice; and my parents, Denise and Dave, whose love and support were always an email/skype call away. Lastly, I would like to thank Galen. Whether it was letting me rant about the pains of writing, taking time to learn about my project, or simply making me smile over the course of this stressful period, this thesis is all the better for it.

Natalie Weigum, December 2014, Oxford

Ah scales, I love scales!!

Louis CK

Contents

List of Figures

List of Tables

Chapter 1

Introduction

1.1 Aerosols and climate

Atmospheric aerosols are small (∼3 nm to 100 μm in diameter) solid or liquid particles suspended in the air. These particles interact with many facets of the climate system and are known to have a significant effect on the global radiation budget. Aerosols originate from a multitude of both natural and anthropogenic sources, and as a result, they encompass a wide range of microphysical properties. These properties influence their effect on the global radiation budget, which continues to contribute the largest uncertainty to estimates of the anthropogenic effect on climate change [*Boucher et al.*, 2013]. Accurately describing these aerosol effects on both a global and local scale is essential for determining the response of the climate to anthropogenic influences.

Compared to greenhouse gases whose lifetimes range from decades to thousands of years, aerosols have relatively short lifetimes in the troposphere, on the order of 4 to 7 days [*Textor et al.*, 2006]. This short lifetime results in aerosols having a highly variable distribution in space and time, making it difficult to quantify their impact on the climate. Prediction of the aerosol effect on climate depends on the ability of three-dimensional numerical models to accurately estimate their atmospheric concentrations and microphysical properties. These models in turn rely on high resolution in

situ measurements and globally expansive satellite retrievals to evaluate and improve aerosol simulations.

This chapter provides an introductory overview of aerosols, their effect on the climate system, as well as a description of the key processes that affect aerosols over the course of their lifetime. In the latter part of the chapter, a summary of the previous literature on aerosol variability is provided, including research into the sources and scales of variability and the impact of neglecting sub-grid variability in aerosol modelling. Finally, the chapter concludes with the aims of this thesis along with a summary of how each chapter addresses these aims.

1.1.1 Microphysical properties

Aerosol particles come in a variety of sizes, chemical compositions, and mixing states. Aerosol diameters typically range from a few nanometers to approximately 100 μm and are often categorised by the following modes: nucleation (3 nm to 0.01 μm), Aitken (0.01 μm to 0.1 μm), accumulation (0.1 μm to 1 μm), coarse (1 μm to 10 μm) and giant ($> 10\mu$m). The initial size of the particle depends on the mechanism by which it is emitted into or produced in the atmosphere. Often aerosols with diameters less than 2.5 μm are referred to as 'particulate matter 2.5' or $PM_{2.5}$. Aerosols with diameters less than 10 μm are collectively referred to as PM_{10}.

Aerosol particles are composed of a variety of chemical species, with the most common constituents being sulphate, nitrate, ammonium, black carbon, organic carbon, dust, sea-salt, and biogenic matter. A single aerosol particle may be composed of one or more chemical species; the degree of mixing of chemical components is called the mixing state. At one extreme, each aerosol component can be assumed to be physically separated from the other components; this is called an external mixture. At the other extreme, the aerosol particles can be assumed to be internally mixed as a homogeneous mixture having the chemical and physical characteristics of the average of all contributing components. The real aerosol mixing state is expected to lie somewhere

between these two limits. These properties are important as they affect the lifetime of aerosols as well as their interaction with other particles, clouds, and radiation.

1.1.2 Aerosol effects on climate

Following the framework of the newly published fifth assessment report from the International Panel on Climate Change (AR5), the effects of aerosols on climate can be categorised into forcings, rapid adjustments, and feedbacks. As defined by *Boucher et al.* [2013], forcings associated with agents such as greenhouse gases and aerosols act on global mean surface temperature through the global radiative budget. Rapid adjustments arise when forcing agents, by altering flows of energy internal to the system, affect cloud cover or other components of the climate system and thereby alter the global radiation budget indirectly. Feedbacks are associated with changes in climate variables that are mediated by a change in global mean surface temperature; they amplify or dampen global temperature changes via their impact on the radiative budget. In the context of these definitions, the impact of aerosols on radiative forcing can be divided into two main categories: aerosol-radiation interactions and aerosol-cloud interactions.

Aerosol-radiation interactions

Aerosols interact directly with incoming solar radiation by scattering and absorption. According to the AR5, the total effective radiative forcing due to aerosol-radiation interactions at the top of the atmosphere (TOA) is -0.45 $\pm$ 0.5 Wm^{-2}, corresponding to a net cooling of the Earth [*Boucher et al.*, 2013]. This net effect is due to a combination of scattering aerosols, which exert a negative radiative forcing, and of partially absorbing aerosols, which may exert a negative or positive TOA radiative forcing depending on the underlying surface albedo [*Myhre et al.*, 2013b; *Haywood and Boucher*, 2000]. The effect is negative over dark surfaces such as oceans or dark forests, and positive over bright surfaces such as desert, snow and ice, or if the aerosol

is above cloud. The interaction of aerosols with radiation depends largely on the radiative properties of aerosols, which are determined by their size distribution, shape, mixing state, and chemical composition. Aerosol optical depth (AOD) is the column-integrated extinction due to aerosols and is a useful property for quantifying aerosol-radiation effects.

Rapid adjustments to the climate system also arise due to forcing from aerosol interactions with radiation. Absorption modifies the thermal structure of the atmosphere, thus altering local atmospheric stability and cloud cover. In a review of semi-direct effects arising from absorbing aerosols, *Koch and Del Genio* [2010] describe a number of rapid adjustments due to aerosol absorption, which depend on the altitude of the aerosol relative to clouds and on cloud type. Absorption by aerosols embedded in a cloud layer heats the layer and causes a reduction in cloud cover. Absorbing aerosols below cloud may increase convection and cloud cover by enhancing vertical motions below the cloud. Aerosol absorption above cloud generally stabilises the underlying layer and tends to enhance stratocumulus clouds by strengthening the inversion and reducing cloud-top entrainment of overlying dry air. However, absorption below cumulus clouds may reduce cloud cover by decreasing evaporation from the surface, thereby decreasing moisture available for cloud formation. These rapid adjustments due to absorbing aerosol result in a net negative radiative forcing.

Aerosol-cloud interactions

Cloud formation commonly takes place in rising air, which expands and cools, allowing for the activation of aerosol particles into cloud droplets and ice crystals when the air is supersaturated (a more detailed explanation of aerosol activation is included in Section 1.2.2). Aerosols can affect the formation of clouds through their ability to act as cloud condensation nuclei (CCN) and ice nuclei (IN). An increase in aerosol concentration can lead to an increase in the number of CCN. At a constant liquid water path this leads to a greater number of smaller droplets, corresponding to an enhancement in

cloud albedo [*Twomey*, 1974]. This cloud albedo effect results in more shortwave radiation being reflected back to space and therefore acts as a negative forcing.

Adjustments due to increased CCN and cloud albedo are more complicated. The traditional view is that a higher aerosol concentration can lead to an increase in the presence of smaller cloud droplets, which are less efficient at producing precipitation and may act to increase cloud lifetime [*Albrecht*, 1989]. This notion is based on the reasoning that droplet concentrations depend on the number of CCN; that development of precipitation is influenced by droplet concentration; and that precipitation decreases cloud amount. While evidence exists for the first step, conflicting results have been shown in terms of the influence of droplet concentration on precipitation [e.g. *Christensen and Stephens*, 2011] and of the impact precipitation has on cloud amount. In some studies, it has been suggested that increased aerosol concentrations promote the development of deep convective clouds and invigorate precipitation [*Rosenfeld et al.*, 2008]. Other studies have shown evidence that aerosol-perturbed clouds cycle through stages of increased and decreased cloud water amount [*Sandu et al.*, 2008; *Lee*, 2012].

The total effective radiative forcing due to aerosols including both radiation and cloud interactions is estimated as -0.9 (-1.9 to -0.1) Wm^{-2}, which counteracts approximately one third of the positive radiative forcing caused by greenhouse gases [*Boucher et al.*, 2013].

1.1.3 Measuring aerosol properties

Measurements of aerosols are important to describe the distribution in time and space of aerosol species and to understand the mechanisms behind important aerosol interactions in the atmosphere. Common measurement platforms include ground-based stations, aircraft campaigns, and satellite retrievals. Different platform types offer their own advantages and disadvantages, and a complementary combination of these platforms is typically used.

Ground-based measurements can provide high temporal resolution of aerosol prop-

erties and allow for characterisation of the temporal evolution of aerosols at a particular point in space. Ground-based platforms employ a myriad of different instruments allowing for measurements of aerosol mass, number, size, and optical properties. Networks of ground-based sensors (e.g. AERONET) offer some of the most accurate measurements of AOD available. Their main disadvantage is they are limited in spatial coverage to the location of the station.

Aircraft campaigns are unique in that they can target specific aerosol events or areas where interesting aerosol microphysics occurs. They are also able to provide information on the vertical profile of aerosols. An aircraft typically uses several instruments to measure a variety of properties, similar to ground-based platforms. While aircraft campaigns are able to cover long horizontal and vertical transects, their spatial coverage is again limited to the location of the campaign.

Satellite retrievals are the only available measurement platform able to provide globally expansive measurements of aerosol properties, e.g. AOD and Angström exponent (indicator of aerosol size), extending over several years. Common satellite instruments, like radiometers, often have large two-dimensional coverage but are unable to retrieve vertically-resolved aerosol properties. Other instruments, such as light detection and ranging (lidar), are able to provide vertically resolved aerosol data but have limited horizontal coverage. While satellite measurements are necessary to obtain a global picture of aerosols, they have difficulty distinguishing aerosols of different composition and cannot obtain measurements of particles within clouds.

1.1.4 Simulating aerosol properties

Model simulations of aerosols allow researchers to investigate the effect of aerosols on local, regional, and global spatial scales, and over temporal scales ranging from short-term weather events to long-term climate. Traditional grid-based aerosol models can cover the entire globe or act over a limited area. Global circulation models (GCM) typically have grid spacings on the order of 100 to 400 km and allow for long term

predictions of aerosol-climate interactions. Limited-area, or regional-scale models, have a wide range of grid resolutions from 100 m to 100 km. Because of their limited area, they can incorporate a higher degree of complexity than global models; however, computational restrictions usually limit these simulations to shorter time periods.

Model simulations of aerosols are complicated by uncertainties in the treatment of the numerous physical and chemical processes that affect aerosols over the course of their lifetime. These models rely on parameterisations to make the complexity of the calculations manageable. These parameterisations can result in large uncertainties in model predictions. It is essential to quantify and reduce the uncertainties associated with model-based estimates in order to improve the prediction of the aerosol effect on climate.

1.2 Processes affecting aerosol properties

The life of an aerosol particle begins when it is emitted into the atmosphere or produced within the atmosphere. Once they enter the atmosphere, aerosols are affected by a number of processes including dynamical transport, microphysical ageing, and interactions with cloud systems, until they are finally removed by deposition. The following section describes a number of these important processes.

1.2.1 Sources

An aerosol source refers to any mechanism that introduces new aerosol particles into the atmosphere. Different emission sources affect the initial size and composition of aerosols and therefore dictate their interactions for the rest of their life cycle. Primary aerosol particles are emitted into the atmosphere directly, whereas secondary particles are formed in the atmosphere through chemical reactions of gaseous precursors.

Primary emission of particles

Natural emissions of aerosols include sea-spray, soil and wind-blown dust, volcanic eruptions, natural forest fires, and wind-lifted biological particles such as pollen, spores, bacteria and plant debris. Sea-spray is produced when wind at the ocean's surface or breaking waves cause bubbles of sea water to burst, releasing sea-salt particles and marine organic matter into the atmosphere. This can also lead to dimethyl sulphide emissions by marine phytoplankton, a precursor to sulphate aerosol [*Solomon et al.*, 2007]. Wind can also lift soil and dust from the Earth's surface into the air. The extent of lifting depends on particle size and wind speed. Volcanic eruptions inject large amounts of gases and particles into the atmosphere, sometimes as high as the stratosphere. These particles are mostly composed of inorganic material such as silicate, sulphate, iron and nitrate, and gaseous species including water vapour, and sulphur dioxide, an important precursor in the formation of sulphate particles. Volcanic emissions of sulphate account for 7% of sulphate emissions [*Solomon et al.*, 2007].

Anthropogenic emissions consist of biomass burning and fossil fuel burning by traffic, power plants, and other industrial processes. Biomass burning and natural forest fires emit primarily organic matter and black carbon. Major source areas include West Africa, Asia, and South America. Fossil fuel burning from traffic emissions is a major source of black carbon, particularly in China and India. Industrial processes usually involve burning fossil fuels in combination with inorganic and metal compounds. As a result, industrial practices tend to emit black carbon, organic matter, sulphate via SO_2, and metallic species. Fossil fuel burning from all sources accounts for 64% of black carbon emissions [*Bond et al.*, 2013] and 72% of sulphate emissions [*Solomon et al.*, 2007].

Other significant anthropogenic aerosol sources include ships, which release aerosol precursor gases such as SO_2 and NO_x, and aviation traffic, which emits SO_2, NO_x, volatile organic compounds (VOC), and soot at higher altitudes.

Nucleation

Nucleation is the process by which aerosol mass is formed by clustering of gaseous molecules and is an important source of particles in the atmosphere. Nucleation occurs when gas molecules aggregate to form a cluster which, at a particular radius, condenses to form a liquid droplet. The process of nucleation can be divided into two types: heterogeneous, where nucleation occurs on a foreign substance like an ion or pre-existing aerosol, and homogeneous, where nucleation occurs without the presence of another substance.

The rate of homogeneous nucleation is derived from the change in Gibb's free energy (ΔG_i) of a nucleating gas cluster as follows [*Seinfeld and Pandis*, 2006]:

$$\Delta G_i = 4\pi\sigma r^2 - \frac{4\pi}{3}\frac{kT\ln S}{v_1}r^3 \tag{1.1}$$

where σ is the surface tension of the condensed cluster, r is the radius of the cluster, v_1 is the cluster volume, T is temperature, k is Boltzmann's constant, and S is the saturation ratio, given as the ratio of the partial pressure to the saturation vapour pressure of the nucleating gas.

If S is less than one, ΔG_i is always increasing with r, and therefore it is always more likely for a cluster to evaporate than to grow. This means that homogeneous nucleation only occurs in a supersaturated vapour phase. When S is greater than one, ΔG_i increases until it reaches a maximum at the critical radius, at which point the gas nucleates. This clustering mechanism is shown schematically in the first stages of Figure 1.1.

A common nucleation mechanism included in global climate models is binary nucleation of the sulphuric acid-water system. Sulphuric acid vapour readily nucleates as it has a very low vapour pressure under atmospheric conditions. This mechanism usually occurs in the upper troposphere where temperatures are cooler and tends to drive new particle production in remote areas, like over oceans. At higher temperatures and

over land, particularly in the continental boundary layer, heterogeneous nucleation of sulphuric acid may occur in the presence of ions, ammonia, or organic compounds, but these mechanisms are not as commonly included in models as the aforementioned binary homogeneous nucleation mechanism [*Kazil et al.*, 2010].

Observational studies have shown that nucleation can lead to a significant increase in the number of cloud concentration nuclei and can therefore have a large influence on cloud radiative properties and precipitation rates [*Kulmala et al.*, 2004]. Global models suggest that nucleation is more important in remote continental regions rather than polluted regions where primary particles dominate [*Spracklen et al.*, 2006].

Formation of secondary organic aerosols

Secondary organic aerosols (SOA) are formed in the atmosphere by chemical transformation of organic compounds. In the most commonly studied formation mechanism, mass is transferred to the aerosol phase when low vapour pressure products accumulate from the oxidation of organic gases [*Seinfeld and Pandis*, 2006]. The oxidation products that have sufficiently low volatilities will partition themselves between gas and aerosol phases to maintain equilibrium. Common oxidisers include the hydroxyl radical, ozone, and the nitrate radical.

Measurements have shown that SOAs are major contributors to particle composition throughout the continental boundary layer [*Jimenez et al.*, 2009]. However, the mechanisms behind the formation of SOA and the rates at which they are formed are highly uncertain. As a result, even state-of-the-art organic gas-particle partitioning models fail to reproduce observed SOA concentrations [*Riipinen et al.*, 2011]. Due to these uncertainties, the treatment of SOA in many global climate models is still quite primitive.

Formation of secondary inorganic aerosols

Secondary inorganic aerosols primarily consist of sulphate, nitrate, and ammonium compounds produced from gaseous precursors in the atmosphere. The precursor gases NO_x ($NO + NO_2$) and SO_2 are oxidised to form gaseous nitric acid (HNO_3) and sulphuric acid (H_2SO_4), respectively. These acidic gases are then neutralised by ammonia (NH_3) to produce ammonium sulphate and ammonium nitrate aerosol. Ammonia preferentially neutralises sulphuric acid vapour over nitric acid due to the low saturation vapour pressure of sulphuric acid. This means that ammonium nitrate is only formed if there is sufficient ammonia present to completely neutralise sulphuric acid.

These reactions are dictated by a thermodynamic equilibrium that depends on temperature, relative humidity, and the ambient concentrations of sulphate, total nitrate, and total ammonia [*Seinfeld and Pandis*, 2006]. This thermodynamic system can be an important contributor to total aerosol mass, particularly in regions of high ammonia and nitrate concentrations like Europe, where nitrate constitutes between 1% and 24% of total aerosol mass [*Putaud et al.*, 2010].

1.2.2 Ageing processes

Once emitted into the atmosphere, aerosols undergo a number of transformations that affect their size, composition, and mixing state, and as a result, change the way they interact with clouds and radiation. These processes are shown schematically in Figure 1.1.

Condensation

As discussed in the previous section, gases can condense to produce new particles. In this section, condensation refers to the process of condensational growth when gases condense on the surface of existing particles causing the particle to grow in size, thereby changing the size distribution of the aerosol population. Common condensable vapours

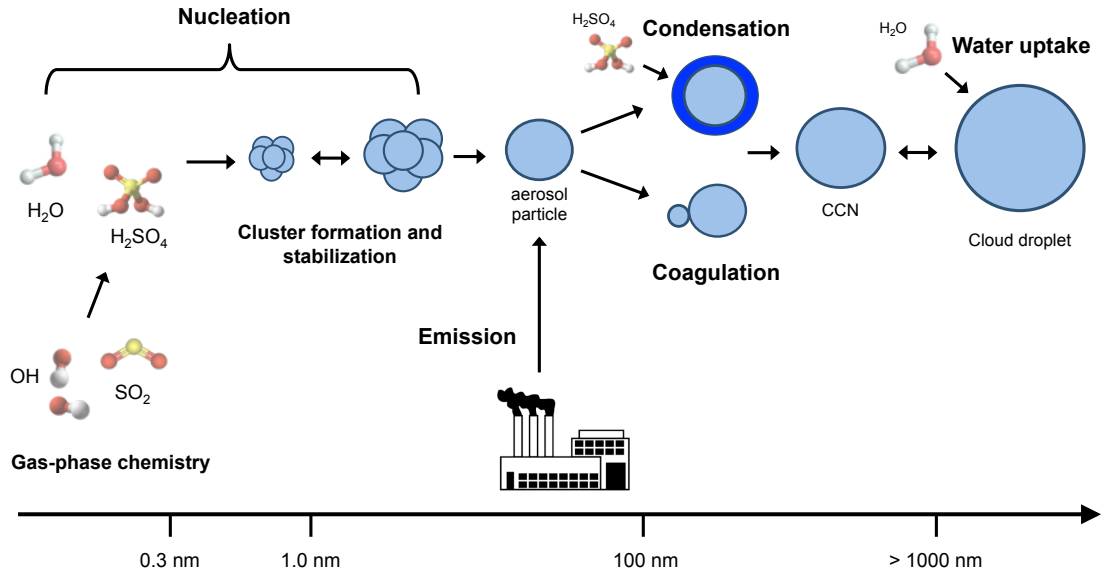

Figure 1.1: Schematic representing the various ageing processes that occur over the lifetime of an aerosol and the impact these processes have on aerosol size.

include sulphuric acid, organic vapours, ammonia, and nitric acid. While condensation of sulphuric acid onto aerosol particles has been incorporated into global models for many years, modelling the condensation of ammonia, nitric acid, and most organic vapours remains a challenge [*Boucher et al.*, 2013].

An aerosol's ability to act as an effective CCN depends on its size and solubility. Condensational growth can therefore significantly impact this ability, not only by changing the size of the aerosol particles, but also by altering their hygroscopicity (ability to take up and retain water). Particles that are hydrophobic will not activate to form cloud droplets. However, when hydrophobic particles like black carbon, accumulate soluble mass via condensation, their ability to act as CCN is enhanced [*Bond et al.*, 2013].

Additionally, condensational growth can affect the optical properties of aerosols. Coating with sulphuric acid and subsequent hygroscopic growth enhances the optical depth of soot aerosols, increasing both scattering and absorption relative to fresh particles [*Zhang et al.*, 2008]. It has also been shown that changing aerosols to a more hydrophilic state can enhance their removal by wet scavenging, thereby decreasing their lifetime and abundance [*Stier et al.*, 2006].

Coagulation

The process of coagulation occurs when two aerosol particles collide and stick together, or *coalesce*, as a result of their turbulent or Brownian motion (random motion of particles suspended in a fluid). Collision and coalescence of particles is most effective in high concentrations of sub micron aerosol populations near sources [*Pierce et al.*, 2009]. Coagulation reduces the number of aerosols in the atmosphere but does not alter the total mass. It is an important process for determining the number concentration of particles that exceed the critical radius required for activation of cloud droplets. Coagulation also increases the degree of internal mixing thereby affecting the evolution of freshly emitted particles through changes in composition [*Riemer and West*, 2013].

Activation

Aerosol activation is the process by which water vapour condenses onto aerosol particles and causes them to grow to form cloud droplets. Without the presence of aerosol particles, warm cloud droplets could only form by homogeneous nucleation (Equation 1.1); however, the supersaturation required to enable the formation of water droplets would be much greater than typical atmospheric conditions.

Cloud droplet formation therefore requires the presence of aerosol particles. The ability of a given particle to act as a nucleus for condensation of water droplets depends on its size, composition, and the local supersaturation. Whereas the curvature of the water surface increases its equilibrium vapor pressure (Kelvin Effect), soluble material dissolved in water can reduce its equilibrium vapour pressure (Raoult's Law). Therefore, the presence of aerosol particles with sufficiently large radii lowers the vapour pressure of water and reduces the supersaturation required for cloud droplet formation. The competition of these two effects is known as Köhler theory and can be visualised as the Köhler curve in Figure 1.2.

The location of the peak supersaturation is at r_c, the critical radius. Below this radius, Raoult's Law is more important than the Kelvin effect, and solution droplets

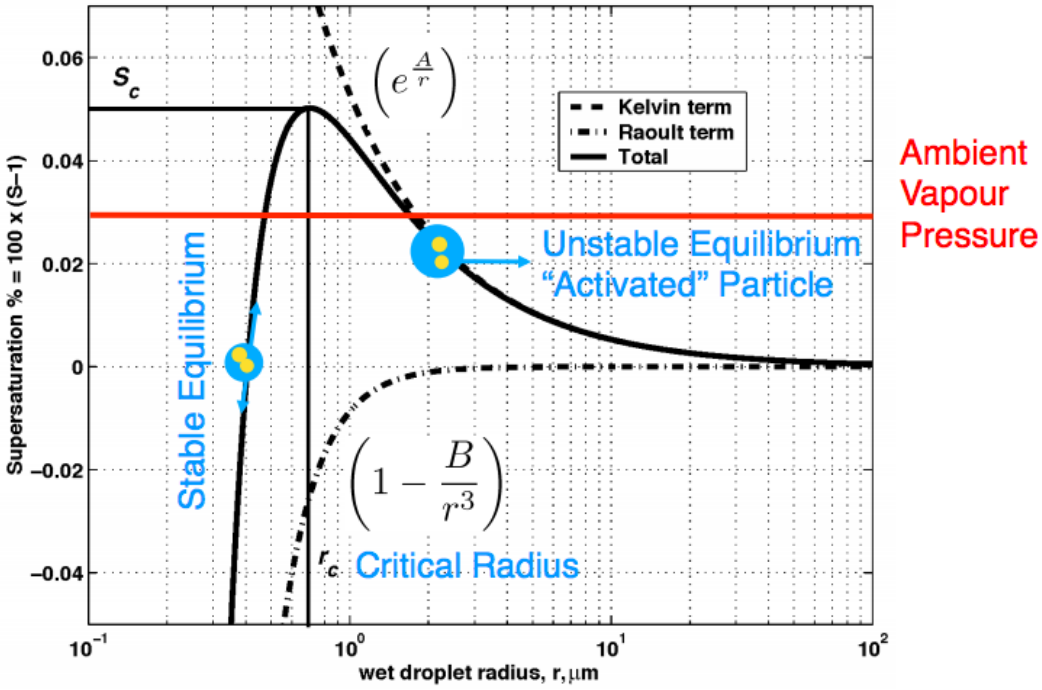

Figure 1.2: Depiction of Köhler theory combining the Kelvin Equation and Raoult's Law, adapted from *Kohler* [1936]. r_c denotes the critical radius and S_c the critical supersaturation, where the particle changes from a stable equilibrium with its environment, to an unstable, "activated" state. 'A' represents a factor containing environmental parameters relating to the Kelvin effect, and 'B' represents a factor containing parameters relating to the mass and degree of dissociation of the solute within the droplet.

are in a stable equilibrium. At radii larger than the critical radius, the Kelvin effect is more important than the Raoult term and the particles grow spontaneously. Droplets with radii larger than the critical radius are said to be "activated". Particles that activate more easily have a greater chance of affecting cloud droplet number concentration and cloud reflectivity [*Seinfeld and Pandis*, 2006].

1.2.3 Sinks

Aerosols are removed from the atmosphere by wet and dry deposition. Removal by dry deposition occurs via two pathways: sedimentation due to gravitational settling and turbulent transport. The process of dry deposition can be characterised by a 'dry deposition velocity', which is an effective velocity describing how fast an aerosol parti-

cle comes into contact with the Earth's surface. The dry deposition velocity depends on the aerosol size and is largest for Aitken and coarse mode particles. Small particles (Aitken mode) have larger dry deposition velocities as a result of their Brownian motion. Particles of sizes greater than 1μm (coarse mode) have increased deposition velocities as gravity becomes more important. Overall dry deposition accounts for 10 - 20% of aerosol removal by mass and is the dominant removal mechanism for coarse mode particles [*Textor et al.*, 2007]. In recent years, global climate models have been incorporating improved dry deposition models, which depend on particle size and characteristics of the Earth's surface [e.g. *Petroff and Zhang*, 2010].

Wet deposition removes aerosol through interactions with clouds and precipitation and can be divided into below-cloud scavenging and in-cloud scavenging. Below-cloud scavenging removes aerosol particles below clouds by collisions with precipitation. As a water droplet or ice crystal falls through the atmosphere, it may collide and coalesce with particles in its path. The number of particles removed depends on the collision and coagulation efficiency of the falling hydrometeor. Like dry deposition, below-cloud scavenging is least efficient for accumulation mode particles. Smaller particles increase the probability of collision due to their Brownian motion, and larger particles have greater inertia and therefore a greater chance of colliding with falling droplets. In-cloud scavenging removes aerosols that exist within a cloud by impaction scavenging through collision with cloud droplets (similar to below-cloud scavenging) or by nucleation scavenging, where the particle activates into a cloud droplet that grows in size and precipitates to the ground. Accumulation mode particles are removed primarily by this mechanism. Wet deposition accounts for 80 - 90% of aerosol removal by mass and is the dominant removal mechanism for Aitken and accumulation mode particles [*Textor et al.*, 2007].

Prediction of wet scavenging remains highly uncertain and is controlled by uncertainties in the prediction of precipitation properties as well as the size and composition of aerosols. For insoluble primary particles like black carbon and dust, nucleation

scavenging also depends strongly on their degree of mixing with soluble compounds [*Boucher et al.*, 2013].

1.3 Aerosol variability

The spatial distribution of aerosols and their microphysical properties exhibit a high degree of variability across the globe, largely due to their relatively short lifetimes (on the order of 4–7 days [*Textor et al.*, 2006]). The highly variable nature of aerosols is one of the major causes of the uncertainty associated with quantifying their effect on climate [*Boucher et al.*, 2013]. A better understanding of aerosol variability and the scales on which it occurs is essential for reducing this uncertainty and improving model predictions of their effect.

Figure 1.3 from [*Myhre et al.*, 2013b] shows how the composition of aerosol varies in different regions of the world. The pie charts demonstrate the relative contribution of each aerosol type to aerosol optical depth, as predicted from a global climate model. One can see over industrialised areas like North America, Europe, and East Asia where there are relatively few natural sources, sulphates and carbonaceous aerosols from fossil fuel burning make a large contribution to overall aerosol amount. Nitrate is also a large component of aerosol optical depth over Europe where NO_x emissions from agriculture and industry are high. Areas such as East Africa and India are dominated by dust aerosols from surrounding desert regions. Remote areas over the ocean are far from anthropogenic sources and are therefore dominated by sea-salt aerosol as well as sulphate from nucleation of oceanic dimethyl sulphide emissions.

In addition to variability in aerosol composition, there exist large gradients in aerosol concentrations across the globe. In a synthesis of ground level particulate matter measurements [*Hidy*, 2009], the regional mass concentrations ranged, on average, from 1 to 80 $\mu g/m^3$ with the highest concentrations found in areas of high population density and industrialisation, especially China and India, but also North America and Europe. The spatial distributions of mass concentrations were shown

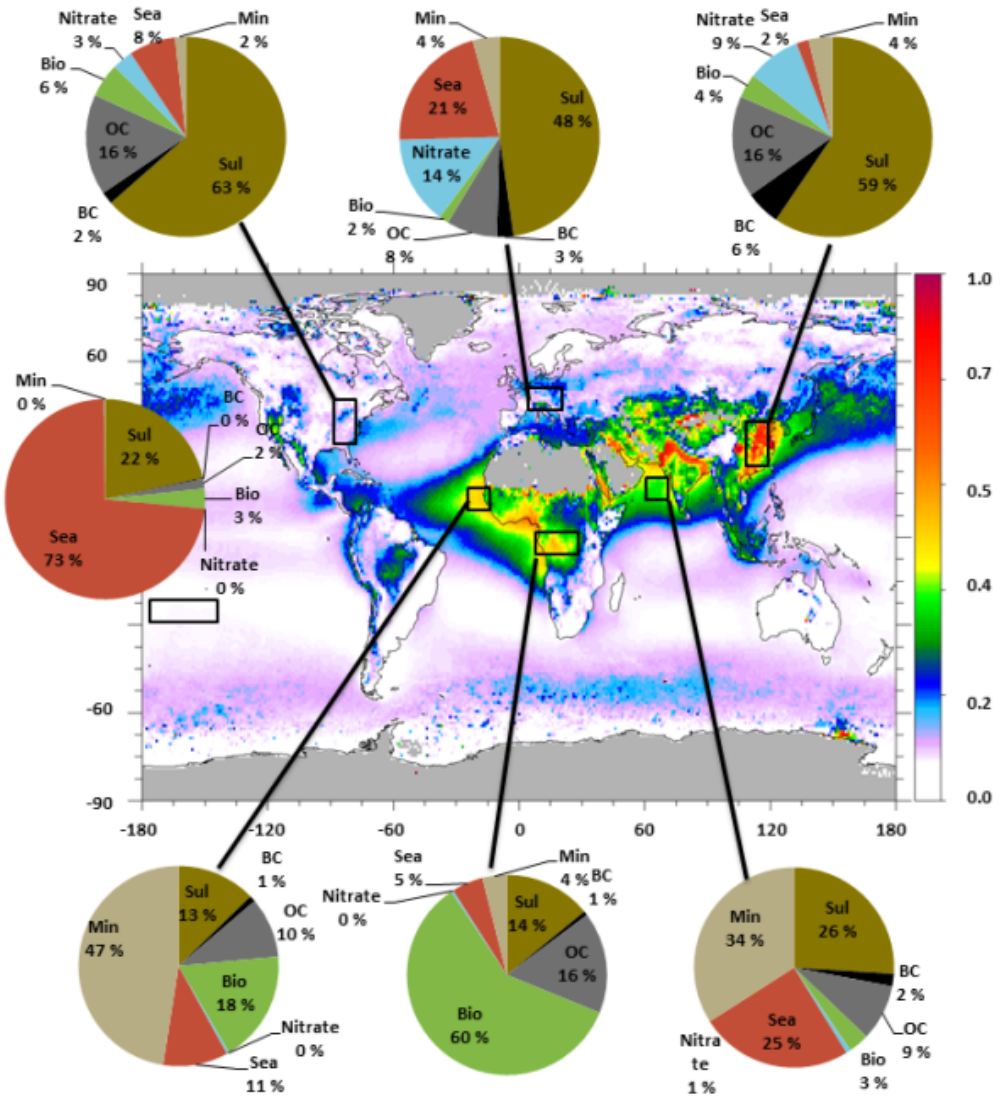

Figure 1.3: From *Myhre et al.* [2013a]. The map shows MODIS aerosol optical depth at 550 nm averaged over the 10-year period 2001–2010. The pie charts represent the contribution of various aerosol types to total AOD for different regions, as estimated by a global aerosol model. Aerosol types are Sul (sulphate), BC and OC from fossil fuel usage, Bio (OC and BC from biomass burning), Nitrate, Sea (sea salt), and Min (mineral dust). Grey areas indicate lack of MODIS data. Note that the contribution from OC is likely underestimated as in most of global models [*Zhang et al.*, 2007]

to depend on the proximity to sources, most of which were continental in origin with contributions from sea salt emissions in the marine environment. Natural sources of blowing dust, sea salt, and wildfires were also shown to contribute to large, intermittent synoptic-scale particle concentrations. Long-range transport of pollution caused persistent regional- and continental-scale gradients of mass concentration, especially

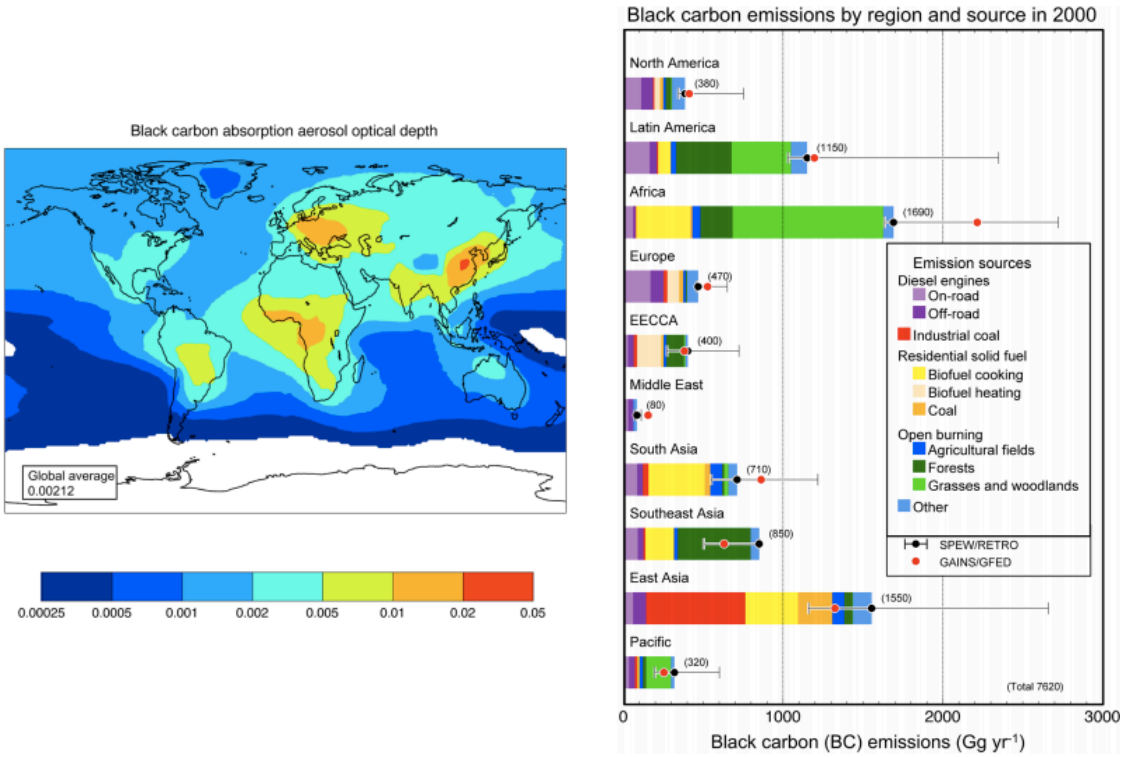

Figure 1.4: From *Bond et al.* [2013]. The left panel shows the aerosol absorption optical depth at 550 nm attributable to black carbon. The fields are from the AeroCom median model fields [*Schulz et al.*, 2006] of all-source black carbon. The right panel (also from *Bond et al.* [2013]) shows emission rates of BC in the year 2000 by region. The orange and black dots represent emission amounts used in two emission databases.

in the Northern Hemisphere. Data were sparse in the Southern Hemisphere but were generally much lower in mass concentrations compared to the Northern Hemisphere [*Hidy*, 2009].

Focusing specifically on the distribution of black carbon, as it is the focus of study in Chapters 2 and 3, one sees that black carbon concentrations are highly variable and are largest around source regions. The left panel of Figure 1.4 shows the distribution of aerosol absorption optical depth attributable to black carbon, with high concentrations over source regions. High sources of black carbon can be grouped into categories, broadly described as diesel engines, industry, residential solid fuel, and open burning. Asia and Africa are dominated by residential coal and biomass fuels (60–80%), while on-road and non-road diesel engines are important emitters (about 70%) in Europe, North America, and Latin America. Residential coal contributes significantly in China,

Russia, and a few Eastern European countries [*Bond et al.*, 2013]. These trends are summarised in the right panel of Figure 1.4.

While concentrations are highest over source regions, black carbon experiences regional and intercontinental transport during its lifetime. Removal from the atmosphere usually occurs within a few days to weeks via precipitation and deposition. As a result, black carbon is found in remote regions of the atmosphere at concentrations much lower than in source regions. Transport from East Asia to the Arctic and the remote Pacific can occur in the spring, when synoptic systems loft pollutants to higher altitudes, where they can be transported long distances. The vertical profiles of black carbon are also quite variable. In polluted regions they generally show a declining mass mixing ratio from the surface to approximately 4 km altitude, and relatively constant values up to above the tropopause. However, in remote regions, which are influenced by the transport of pollution from source regions, black carbon loadings tend to peak in the free troposphere or above [*Bond et al.*, 2013].

1.3.1 Sources of variability

Aerosol variability arises from a number of different mechanisms including emissions that vary in space and time and meteorological influences. Variability in aerosol composition and distribution can largely be explained in terms of major aerosol sources, such as biomass burning, megacities and dust storms; and major sinks, such as precipitation [*Anderson et al.*, 2003]. For example, *Garrett et al.* [2010] showed that the seasonal variability in Arctic haze is dominated by wet scavenging, which is most efficient in the summer months when the air is warm and moist. *Ram et al.* [2010] measured carbonaceous aerosols over India and attributed the variability in black carbon and organic carbon concentrations to source variability and emission strength of biomass burning during the winter. In European industrial and urban areas, satellite observations of regional variations in AOD were related to anthropogenic emissions of aerosol precursors such as SO_2 and NO_x and their subsequent transformation into the

aerosol phase [*Robles González et al.*, 2003].

Aerosol variability can also be explained by the fact that after aerosols are emitted into the atmosphere, their lifetimes in the troposphere are much shorter than the time scales of horizontal mixing processes that eliminate mesoscale variations. Theoretical and observational studies show that global variability of aerosol concentrations is inversely related to residence time in the atmosphere and the spatio-temporal distribution of sources and sinks [*Junge*, 1974; *Jobson et al.*, 1999].

Meteorological factors also contribute significantly to aerosol variability. Analysis of ground-based measurements in Europe demonstrated that the most prominent explanatory meteorological variables for variability in particulate mass concentrations were convective boundary layer depth, wind speed, wind direction, and temperature. Vertical mixing in the boundary layer causes horizontal inhomogeneity by mixing clean tropospheric air from higher altitudes into the polluted boundary layer. High wind speeds enhance atmospheric dispersion, and consequently lower concentrations of sulphate, nitrate, and ammonium aerosols [*Squizzato et al.*, 2012]. Conversely, *Kiliyanpilakkil and Meskhidze* [2011] showed that surface wind speeds greater than 4 m/s are linearly correlated with marine aerosol optical depth as higher wind speeds increase sea-salt emissions.

The aerosol distribution over the UK is influenced by the UK's unique meteorological conditions that favour frequent renewal of air masses due to its relatively flat terrain, predominant mean westerly winds, and frequent passages of cold fronts and depressions resulting in rain [*Rodriguez et al.*, 2007]. Aerosol number concentrations from a sampling station in Harwell, UK showed large fluctuations as the area experienced periods of easterly winds when it encountered polluted air from London and continental Europe, followed by periods of cleaner westerly air from the North Atlantic [*Asmi et al.*, 2011].

Temperature has an indirect effect on the variability of aerosol distributions through its impact on primary and secondary emissions. In a recent study analyzing PM data

from European sampling stations [*Barmpadimos et al.*, 2012], temperature was shown to have a negative relationship with $PM_{2.5}$ in winter and a positive relationship in summer. The winter relationship of $PM_{2.5}$ with temperature can be explained by the fact that nitrate formation is enhanced at colder temperatures. The positive relationship between $PM_{2.5}$ and temperature in summer is likely due to fast production of secondary aerosols that occurs with high solar radiation. The PM_{10} measurements had a positive relationship with temperature, which can be attributed to the fact that higher temperatures are often associated with drier soil conditions, which can lead to enhanced dust emission. *Cusack et al.* [2013] also measured a high degree of variability in nucleation and accumulation mode particles in the Mediterranean. Elevated concentrations coincided with high temperatures, which increased photochemical reactions and subsequent growth from condensation of organic vapours produced from volatile organic compounds.

In periods of stagnant meteorological conditions, aerosol microphysical processes can also have an important effect on aerosol variability. Several studies show enhanced condensation of volatile organic compounds during periods of high atmospheric stability [*Daher et al.*, 2013; *Sardar et al.*, 2005; *Matsui et al.*, 2009] as well as increased variability in particle size due to coagulation [*Nicolas et al.*, 2009; *Costabile et al.*, 2009].

As one can see, the factors controlling aerosol variability are vast, ranging from sources, sinks, meteorological factors such as boundary layer stability, wind speed, and temperature, and aerosol microphysics. Observed variability in aerosol distribution and composition is rarely the result of one process; it is a complex interaction between meteorological and aerosol processes that contribute to aerosol variability on different scales. It is essential to determine the relative contribution of different processes to aerosol variability in order to quantify the important scales on which this variability occurs.

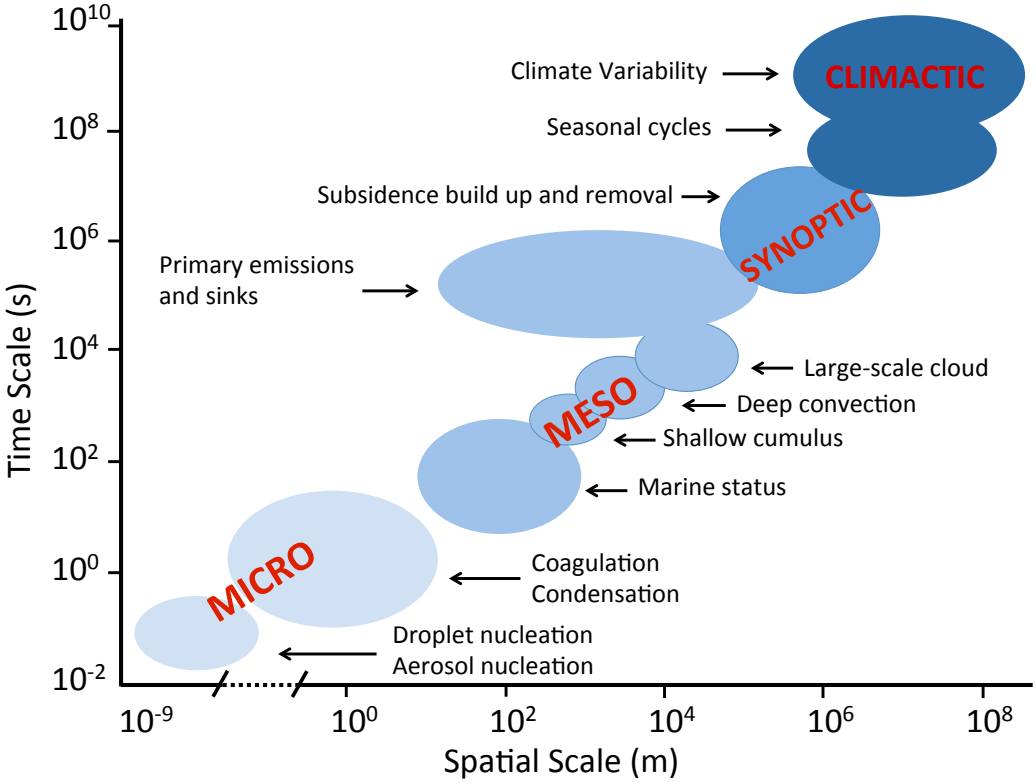

Figure 1.5: Schematic depicting the spatial and temporal scales of aerosol interactions in the atmosphere over the course of their lifetime. The interactions can be categorised into micro-scale, meso-scale, synoptic scale, and climate scale.

1.3.2 Scales of spatial variability

The preceding section provided an overview of the multitude of interactions that contribute to aerosol variability. Typical spatial scales of some of these interactions (shown in Figure 1.5) range from 1 nm to 1000 μm for aerosol and droplet nucleation, less than 100 m for coagulation and condensation processes, 100–1000m for marine stratus formation, 1–2 km for shallow cumulus formation, 2–10 km for deep convection, 50–100 km for large-scale cloud systems, 20–200 km for diurnal cycles of land/sea breezes and for some major aerosol sources and sinks such as dust storms, biomass fires, megacity plumes, and precipitation and $<$ 1000 km for synoptic scale build up (e.g. smog) and removal [*Wang et al.*, 2011; *Jacobson and Seinfeld*, 2004; *Anderson et al.*, 2003].

Traditionally, modelling of aerosols operated under the assumption that aerosol concentration and composition vary horizontally at the same scale as the airmass scale.

This was supported by older studies that showed that aerosol transport distances in the lower troposphere were related to synoptic-scale meteorology [*Schwartz*, 1989; *Benkovitz et al.*, 1994]. However, recent studies reveal that aerosol variability occurs on many different scales, which are frequently smaller than the airmass scale.

These more recent studies seeking to quantify aerosol scales of variability have focused on variability of aerosol radiative properties. *Anderson et al.* [2003] used autocorrelation functions of a number of observational datasets to assess the temporal and spatial variability of aerosol light scattering at 550 nm and of AOD. A preliminary inspection of the data series revealed that while aerosol plumes do occur on scales of several hundred to a thousand kilometres, they are rarely homogeneous over temporal scales of more than 12h and spatial scales of more than 200 km. The autocorrelation functions of each dataset showed that most of the variation in the aerosol properties in fact existed on scales of 40-160 km (or 3-6 hours).

Targino et al. [2005] performed a similar analysis using autocorrelation functions of aircraft data from clean and polluted regions in the free troposphere. They found the spatial scales of variability to be on the order of 10 km, much smaller than results from *Anderson et al.* [2003] who used aircraft data measured in the boundary layer. They attribute the difference in scales to sporadic vertical intrusions of aerosol from the boundary layer into the free troposphere, creating smaller patches of polluted air compared to the larger scale plumes found in the boundary layer. *Shinozuka and Redemann* [2011] compared the horizontal variability of aerosol optical depth during two contrasting phases of the Arctic Research of the Composition of the Troposphere from Aircraft and Satellites (ARCTAS) campaign. In the first phase, which was dominated by local emission sources, AOD demonstrated considerable variability at scales of 20 km, whereas the second phase, which was dominated by long-range transport, showed very little variability at these scales, suggesting that proximity to sources has a significant effect on aerosol variability. *Redemann et al.* [2005] analyzed the spatial variability of AOD data derived from aircraft sun photometer measurements and

demonstrated that AOD can vary by as much as 50-70%, but more typically 25-50% over horizontal distances of 50 km. Note that this range does not refer to differences in mean AOD, but rather the possible maximum variations between instantaneous AOD measurements. *Kumar et al.* [2013] correlated MODIS satellite data at 40 km resolution at select locations with all other grid points to show that AOD over South India is relatively homogenous over radial distances of 100-150 km but variability in AOD increases significantly at larger scales.

Studies quantifying the scales of variability of specific aerosol types are scarce. There are a few studies that have looked at correlations between black carbon measurements from nearby sites in populated cities and found black carbon concentrations to be weakly correlated between sites, suggesting a high degree of spatial variability at neighbourhood scales [*Venkatachari et al.*, 2006; *Thornhill et al.*, 2008; *Snyder et al.*, 2010].

All of these studies demonstrate that significant aerosol variability exists on scales smaller than 100 – 200 km, and that these scales can vary depending on location, meteorological conditions, and nearby sources. Most of these studies use high resolution aircraft data whose flight tracks cover only small regions of a few hundred to a couple thousand kilometres. Many of these aircraft campaigns were designed to fly through regions where significant aerosol plumes were anticipated and therefore may not be representative of typical aerosol variability. Other studies use globally expansive satellite data, but these are limited to assessing variability of column-integrated variables without distinguishing between different aerosol types.

Previous research has shed light on the importance of quantifying the scales of aerosol variability; however, there is still a lack of understanding regarding its significance. Further research is required to quantify how this variability impacts aerosols' effect on climate and to determine what scales of aerosol variability are most important to the overall radiation budget.

1.4 Scale problem in aerosol modelling

Global model simulations of aerosols are necessary in order to predict the aerosol effect on climate; however, models can show large discrepancies in aerosol concentrations when compared to observations. In a large inter-comparison study of 16 GCM simulations of aerosol optical properties, *Kinne et al.* [2006] found that although the mean global annual AOD simulated by the various models agrees well with ground-based and satellite-retrieved AOD, more detailed comparisons revealed that there exists large differences in regional aerosol distribution and compositional mixture. *Wang et al.* [2011] showed that even when using a multi-scale aerosol-climate model, simulations of black carbon at the surface were underestimated by a factor of 2-4, and accumulation mode number concentrations in the mid to upper troposphere were overestimated by a factor of two. Other aerosol and gas fields showed less extreme differences, matching observations within a factor of 2 in most cases [*Wang et al.*, 2011].

A fundamental limitation of GCMs is their inability to capture spatial variations smaller than the size of their grid boxes, which typically range from 100 – 400 km for aerosol climate simulations. This means that spatial variations of meteorological and aerosol parameters are averaged over the grid cell area so that the variability within the grid cell may not be properly represented. The previous section demonstrated that significant aerosol variability exists on scales smaller than global climate model grid-boxes, and discrepancies between aerosol modelling schemes and observations have been attributed to these sub-grid spatial variations [e.g. *Gustafson et al.*, 2011; *Wang et al.*, 2011; *Benkovitz and Schwartz*, 1997]. It is therefore necessary to determine the extent to which different sub-grid scale processes contribute to the discrepancies in aerosol modelling in order to focus model development on parameterisations of these important aerosol processes.

1.4.1 Impact of neglecting sub-grid variability

In global climate models, and even in higher resolution regional-scale models, sub-grid variability exists for both meteorological and aerosol parameters. Neglecting sub-grid variability in these models could significantly affect simulated aerosol outcomes through a multitude of non-linear processes.

When simulating emission of aerosol into the atmosphere, the heterogeneous emissions from all aerosol sources within a model grid-box are averaged over the entire grid-box, which instantaneously dilutes elevated point sources and mixes individual aerosol plumes. This can have a significant impact on the ageing of aerosols and their subsequent interactions within the simulated climate. *Qian et al.* [2010] explored the the effect of neglecting sub-grid scale emission heterogeneity on simulated aerosol and trace gas concentrations using a regional-scale model. Their experiments involved running the model over an urban area at a constant resolution while varying the resolution of input emissions. They found that emissions can account for up to 50% of the total sub-grid variability in regions near urban sources; however, the impact of emissions is much less significant over rural and remote areas and decays with increasing altitude. Further modeling studies [e.g. *Karamchandani et al.*, 2002] have demonstrated how the inability of traditional grid models to resolve sub-grid scale emissions can lead to errors in determining the contribution of elevated point sources to ambient concentrations.

Wind-driven emissions are also affected by sub-grid variability of wind fields. *Marcella and Eltahir* [2010] incorporated a dust emission scheme into a regional-scale model to account for sub-variability of wind fields over southwest Asia. Increased variability of wind fields was found to increase AOD by nearly 35%, producing more realistic results when compared to observational datasets.

Chemical reaction rates often have non-linear dependencies on aerosol and gaseous concentrations. The instantaneous mixing of gaseous and aerosol concentrations can therefore produce errors in reaction rates for processes such as nucleation, condensation, and secondary organic aerosol formation. Coarse grid resolution was found to be

partly responsible for the negative bias in SOA model predictions due to inaccurate representation of primary organic aerosol emissions, VOC emissions, and SOA production rates [*Stroud et al.*, 2011; *Wainwright et al.*, 2012]. In a study exploring the impact of grid-scale versus plume-scale treatment of aircraft emissions, they found that emitting gaseous emissions in individual plumes rather than diluting over the grid decreased ozone production by 77%, methane destruction by 68% and carbon monoxide destruction by 74% [*Cameron et al.*, 2013], highlighting the highly nonlinear nature of these reactions.

Neglecting the sub-grid variability of the underlying topography can also have significant effect on aerosol simulations. At lower resolutions, the sharp features in terrain are smoothed out, which can impact flow patterns and precipitation development. Evidence shows that aerosol concentrations are significantly altered by model grid resolution with the strongest effect occurring in regions of complex terrain and flow patterns [*Gustafson et al.*, 2011; *Girard and Bekcic*, 2005]. To account for sub-grid variability in orographic precipitation, *Leung and Ghan* [1995] developed a parameterisation designed to predict precipitation, temperature, and soil moisture for a selected number of surface elevation classes within each model grid cell. They concluded that a simulation performed at 90-km grid resolution with the sub-grid parameterisation performs better compared to observations than simulations performed at 90-km or 30-km grid resolutions without the parameterisation due to better representation of terrain variability. *Qian et al.* [2010] also found that terrain variability, through its impact on meteorological fields such as wind and planetary boundary height, affects the transport and mixing of aerosols.

The spatial variability of relative humidity can impact modelling of aerosol optical properties due to non-linearities in aerosol hygroscopic growth, particularly in regions of high humidity (90–100%). This non-linear relationship can cause large errors in calculations of aerosol optical depth at GCM resolutions due to their inability to capture the variation in relative humidity at sub-grid scales [*Haywood et al.*, 1997].

Bian et al. [2009] showed that increasing the resolution of relative humidity from 2°x2.5° to 1°x1.25° increases aerosol radiative forcing by 8–9%. This difference is likely even more dramatic at higher resolutions since a 1°x1.25° grid is still quite coarse compared to the processes that induce variations in humidity. *Myhre et al.* [2002] suggest that global studies may underestimate the magnitude of the radiative forcing due to hygroscopic aerosols by up to 30–40% due to coarse spatial resolution, at least over regions of high humidity.

The treatment of sub-grid variability of clouds has been studied extensively over the past decades, and it is well established that parameterisations of cloud processes in global climate models are necessary to accurately capture their variability. While the variability of cloud properties is beyond the scope of this thesis, it is worth highlighting the effect of the sub-grid variability of convection on aerosol distributions. Model resolution can affect the intensity of convective transport by its ability to resolve turbulence. A study by *Klich and Fuelberg* [2014] using a regional-scale model at varying resolutions showed that convective transport occurs much more rapidly at high resolution. Therefore, the scale at which convective transport is resolved can have an effect on the vertical distribution of gaseous and aerosol tracers.

While the above studies highlight the important impact of sub-grid variations in models on simulations of aerosol fields, it is unclear which processes have the most effect. In the paper by *Gustafson et al.* [2011] exploring aerosol sub-grid variability, they conclude that improvement in modelling aerosol variability depends on the underlying processes that are most affected by sub-grid variability. If meteorological effects such as transport and advection are the most important, then the problem may only be solved by increasing model resolution. However, if the main issues involve specific aerosol processes such as emissions, non-linear reactions, or vertical mixing, then there may be other ways to parameterise this sub-grid variability.

It is clear that disentangling meteorology from aerosol processes is key to improving our understanding and, ultimately, the representation of aerosol sub-grid variability.

Most of the previous studies in this area explore the effect of sub-grid variability by varying model resolution and evaluating the subsequent effect on aerosol fields. In these studies, aerosol fields are affected by changes in resolution of a multitude of different model components, making it difficult to isolate and understand the impact of a particular aerosol process. Modelling aerosol microphysics is computationally expensive, which further emphasises the importance of determining which processes would benefit most from increased variability so that modellers can focus on improving parameterisations for these specific processes.

1.4.2 Accounting for sub-grid variability

One of the major challenges to future modelling is determining how to account for the sub-grid variability of aerosol processes. Several methods have been attempted in the literature including adaptive grid techniques, plume-in-grid techniques, emissions parameterisations and other sub-grid parameterisations.

Using an adaptive grid is a relatively new concept where the resolution of a model is not constant over the model domain but rather changes continuously and automatically to allow for more detailed simulations in regions where sub-grid variability is significant. This technique has been applied to the regional scale model CMAQ, the first to include simulations of particulate matter with an adaptive grid. They evaluated the model over a small region in the U.S. with the adaptive grid version of CMAQ showing improvement compared to its static grid counter-part [*Garcia-Menendez et al.*, 2010]. Most of the existing models of this nature are in preliminary development stages, focusing on testing the accuracy of the dynamics and physics parameterisations compared to current models [e.g. *Skamarock et al.*, 2012]. While these models offer promising potential for the future of climate modelling, inclusion of aerosol processes on a global scale will require substantial further development.

A more commonly employed technique is the plume-in-grid methodology where a reactive puff model is embedded within the host grid model in order to track near-

source transport and chemistry of sub-grid scale plumes [*Karamchandani et al.*, 2002]. This method has been employed in many regional-scale modelling studies and must be customised to each specific source. The method has been shown to capture particulate plume events more often and generally better than the standard grid-based approach [e.g. *Karamchandani et al.*, 2006]. *Vinken et al.* [2011] employed a plume-in-grid technique for gaseous ship plume emissions in a global model, which improved simulations of NO_x chemistry in regions with high ship emissions.

Many previous studies have focused on developing parameterisations to attempt to account for sub-grid scale heterogeneity of aerosol and gaseous emissions. These parameterisations do not explicitly model the processes that lead to the dilution and ageing of species to the size of a model grid-box; they instead reproduce the effect of heterogeneous emissions on large-scale variables like aerosol concentrations. *Galmarini et al.* [2008] developed a parameterisation that translated sub-grid scale emission heterogeneity into a measure of concentration fluctuations using the variance of the concentrations. They found that accounting for variance as a prognostic variable allows one to quantify uncertainty due to sub-grid variability and recover information regarding particulate concentrations on sub-grid scales. This method has interesting implications but has not been tested in a global scale model. *Cassiani et al.* [2010] built upon this concept using a stochastic fields method where the sub-grid emission variability is assimilated in the model as a probability density function (PDF) of the emissions. The PDF technique has also been used on wind fields to improve parameterisations of wind-driven dust emissions *Cakmur et al.* [2004]; *Ridley et al.* [2013].

Pierce et al. [2009] use an approach that determines the probability that a given particle emitted within a model grid-box will survive and transfer to a neighbouring grid-box. This approach is based on the fact that artificial dilution of emitted particles does not account for reduction in particle number by coagulation as they spread through the grid cell, meaning that particles that should not survive long enough to leave the source grid cell may be artificially advected to neighbouring grid-boxes. *Stuart*

et al. [2013] took a similar approach for sub-grid scale coagulation of sea-salt particles in order to quantify the effect of coagulation on marine cloud brightening. Both studies showed that the parameterisations decreased overall number concentrations, producing more realistic results.

These methods offer a number of different approaches to tackling the sub-grid problem, each with their own advantages and disadvantages. Increasing our understanding of the underlying mechanisms most affected by sub-grid variability will help guide future development of these methods.

1.5 Aims of this thesis

The overarching goal of this project is to determine the important scales of variability of aerosol microphysical properties in order to improve predictions of future climate. The effect of aerosols on climate has been identified as one of the largest uncertainties in climate research. A major cause of this uncertainty is the high degree of spatial and temporal variability of tropospheric aerosol properties and the processes that affect their lifetime. Changes in aerosol distribution in time and space make it difficult to quantify the impact of anthropogenic aerosol on the climate system and complicate our ability to predict aerosol climatic effects. It is therefore necessary to obtain a detailed understanding of aerosol processes and feedbacks, and to quantify them on relevant scales, which can span orders of magnitude in time and space.

This thesis seeks to answer the following research questions:

1. What are the important scales of variability of aerosols?
2. How does a GCM's inability to resolve sub-grid scale aerosol variability affect model predictions of aerosols?
3. What processes contribute the most to aerosol variability?
4. How can we improve model simulations of aerosol variability?

These questions are addressed through a number of different approaches in the subsequent chapters of this thesis. Chapter 2 seeks to quantify the scales of important aerosol features in the atmosphere and relate these scales to overall aerosol variability. This is accomplished by using aircraft measurements of black carbon to quantify the spatial scales of black carbon plumes. The measurements were taken during the HIAPER Pole-to-Pole Observations (HIPPO) aircraft campaign, whose flight track spans thousands of kilometres over the Pacific Ocean with nearly continuous vertical profiling in order to provide substantial latitudinal and vertical coverage of black carbon in the troposphere. This unique dataset allows for the characterisation of the spatial scales of typical black carbon plumes in a large region of the globe.

Chapter 3 seeks to quantify how a GCM's inability to resolve sub-grid scale variability affects model simulations of important aerosol features, such as plumes. The aim of this chapter is to explore the impact of model resolution on aerosol plume scales by comparing the scales of observed plumes from Chapter 2 to those simulated by global climate models. In order to produce meaningful comparisons between the HIPPO aircraft data and global climate model data, a flight track simulator is implemented during the model runs, which allows the model data to be sampled at the same time and spatial locations as the aircraft measurements Two global models are used in this analysis: ECHAM-HAM at three different resolutions and HadGEM-UKCA in two configurations differing only in their description of convective scavenging. Running ECHAM-HAM at three different resolutions enables the investigation of the impact of model resolution on simulated plume scales. The two simulations using HadGEM-UKCA enables the analysis of the impact of improving aerosol processes (as opposed to increasing resolution) on plume scales. In addition to comparing observed and simulated plumes scales, this chapter takes advantage of global climate models' ability to simulate three-dimensional aerosol fields at all points in time and space by exploring the horizontal and vertical extent of the identified plumes and by exploring the difference in black carbon variability in near-source and remote regions.

Chapter 4 addresses Questions 2 and 3 by investigating the impact of aerosol variability on important aerosol processes. A novel technique is developed to disentangle the effect of aerosol variability from other sources of variability within the model by simulating the aerosol processes at varying resolutions while maintaining a constant resolution in all other model fields. This technique is implemented in the regional-scale model WRF-Chem to quantify the effect of neglecting sub-grid aerosol variability on aerosol optical depth and cloud condensation nuclei. This analysis enables the identification of aerosol processes that are most affected by neglecting aerosol sub-grid scale variability and the resulting impact this has on the prediction of aerosol interactions with clouds and radiation.

The work from all three chapters will help answer the final research question by increasing our understanding of aerosol variability and the underlying mechanisms most affected by sub-grid variability. The findings will help guide future development of aerosol models in order to improve model predictions of the aerosol effect on climate.

Chapter 2

Scales of variability of black carbon plumes from HIPPO campaign

The work presented in this chapter is an updated version of the publication in Geophysical Research Letters [Weigum et al., 2012]. The publication is a co-authored work; I designed the study, analysed the data, and wrote the results with guidance from my supervisor P. Stier. Authors J. P. Schwarz, D. Fahey, and R. Spackman kindly provided the data for the analysis and feedback on the written paper.

In this chapter the scales of black carbon (BC) aerosol plumes are quantified using single-particle measurements of BC mass from recent aircraft campaign, HIAPER Pole-to-Pole Observations (HIPPO) [*Schwarz et al.*, 2010a].

Black carbon is the major anthropogenic aerosol absorber of solar radiation. Model simulations have shown that, on average, BC absorption reduces anthropogenic aerosol top-of-atmosphere negative radiative forcing by 60% [*Schulz et al.*, 2006]. BC can also affect the Earth's radiation balance through a number of complex interactions with clouds and the Earth's surface, making its total effect highly uncertain [*Ramanathan and Carmichael*, 2008].

Aircraft-based observations are particularly useful for assessing aerosol variability

as they can provide high-resolution information on the spatial distribution of BC in both remote and polluted areas. However, quantitative measurements of BC can be difficult to achieve. Even though BC is responsible for most of the aerosol absorption in the visible wavelength, it is only a small contributor to the total aerosol mass [*Brook et al.*, 1997]. BC's non-solubility and refractory nature (i.e. vaporising only at very high temperatures) make traditional methods designed to measure aerosols largely ineffective for measuring BC [*Schwarz et al.*, 2010b]. In addition, BC particles are non-spherical and have complex morphology, providing further limitations to measurement methods. The Single Particle Soot Photometer has become increasingly popular in the past decade as a useful instrument for quantifying BC as these problems are generally avoided [*Cross et al.*, 2010].

The HIPPO aircraft campaign employed the Single Particle Soot Photometer to make measurements of BC over the Pacific Ocean. The HIPPO flight track spans thousands of kilometres with nearly continuous vertical profiling in order to provide substantial latitudinal and vertical coverage of BC in the troposphere. This unique dataset enables the characterisation of spatial scales of typical BC plumes in a large region of the globe. It is noted, however, that as the residence times for most aerosols (dust, sulphates, particulate organic matter) are similar to that of BC (on the order of 4 – 7 days), BC scales of variability are likely indicative of general aerosol variability [*Textor et al.*, 2006].

2.1 Methods

2.1.1 Aircraft Measurements

The measurements included in the analysis were taken on board the NSF/NCAR GV [hippo.ucar.edu] aircraft during all five missions of the HIPPO campaign (subsequently referred to as HIPPO1, HIPPO2, etc.). The flights provide extensive vertical coverage, consisting of over 700 vertical profiles, with altitudes ranging from 0.2 to 14 km, and

Table 2.1: Summary of HIPPO mission dates and flight information

Campaign	Date	Number of flights
HIPPO1	9 - 30 Jan 2009	10
HIPPO2	31 Oct - 22 Nov 2009	11
HIPPO3	24 Mar - 16 Apr 2010	11
HIPPO4	14 Jun - 11 Jul 2011	10
HIPPO5	9 Aug - 9 Sept 2011	13

with a nearly global span of latitudes, ranging from 87°N to 67°S. The five missions took place during different seasons with the first (HIPPO1) occurring during the period of 9 - 30 January 2009, HIPPO2 from 31 October to 22 November 2009, HIPPO3 from 24 March to 16 April 2010, HIPPO4 from 14 June to 11 July 2011, and HIPPO5 from 9 August to 9 September 2011. The details of the missions dates and number of flights included in the analysis is summarised in Table 2.1.

BC measurements were made with a Single Particle Soot Photometer (SP2) [*Schwarz et al.*, 2010b]. The SP2 instrument operates based on the principle that the peak intensity of emitted radiation of a particle at its vaporisation temperature is linearly proportional to its mass, over a defined mass range [*Schwarz et al.*, 2006]. To measure the BC mass content, the detected particles are heated up by an intense laser beam. BC particles have a high enough boiling point that they emit thermal radiation, or "incandesce", as they vaporise, usually at a temperature around 4,000K [*Moteki and Kondo*, 2010]. Any non-refractory particles or coatings are vaporised at a much lower temperatures and do not absorb enough energy to heat significantly; however, they elastically scatter laser light without evaporation, which can also be detected by the SP2.

The SP2 provides highly sensitive measurements of BC mass and mixing state of individual BC-containing particles. Recent inter-comparisons of instruments measuring BC content of soot aerosol have shown that SP2 measurements of BC mass in individual aerosol particles are independent of particle mixing state and of a wide range of morphologies (although BC shape does introduce uncertainties, explained in

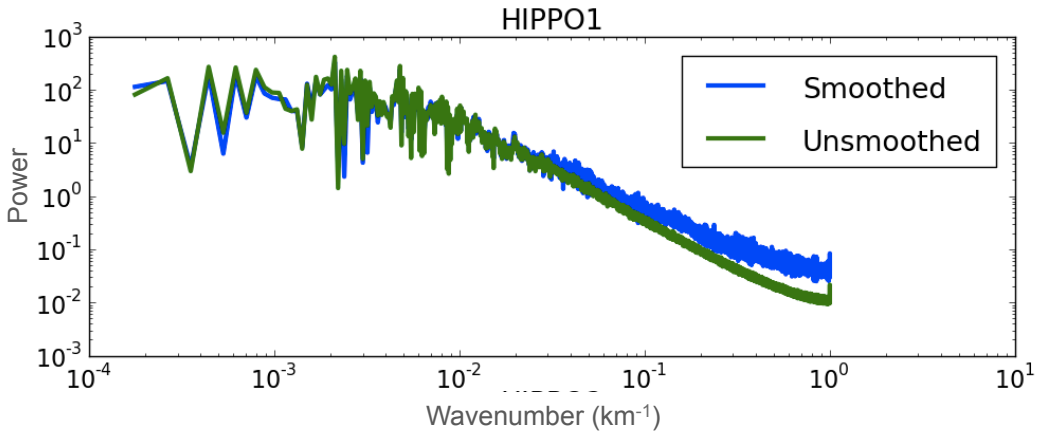

Figure 2.1: Power spectral density function of smoothed and unsmoothed BC MMR data for the first HIPPO mission (HIPPO1) as a function of wavenumber (km^{-1}).

the following paragraph) [*Cross et al.*, 2010; *Slowik et al.*, 2007]. The SP2 data is collected on a per-particle basis so that the BC contribution of a particle's mass is recorded each time a particle is detected. A conservative lower mass detection limit of the SP2 based on a moderate laser intensity was determined to be 0.7 fg (or 90 nm volume equivalent diameter); the upper diameter limit at which the SP2 can adequately sample particles is approximately 2μm [*Schwarz et al.*, 2010b].

For the current analysis, BC mass measurements are averaged over one-second time intervals and converted to a mass mixing ratio (MMR) in nanograms of BC per kilogram of dry air with a net uncertainty estimated at 30% in BC mass. The uncertainty partly arises from potential differences in the shape and morphology of ambient BC and the calibration material, which leads to differences in the particle emissivity and incandescence signals [*Shiraiwa et al.*, 2008; *Moteki and Kondo*, 2010]. Because the interest of this chapter lies in the spatial scales of BC plumes, the one-second time data is converted to spatial units using the aircraft's true airspeed at each time step so that the BC MMR is described as a function of 'distance along the flight track' with 1-second resolution.

2.1.2 Plume Identification

To facilitate the identification of major plume structures, the data from each HIPPO flight was smoothed by the regularisation method. This method is advantageous as it can handle unevenly spaced data, allows for continuous control over smoothness with one smoothing parameter, and makes no assumptions about the underlying causes of the variations in the mathematical structure of the series [*Eilers*, 2003]. The concept behind smoothing by regularisation is to balance a 'goodness-of-fit' term with the 'roughness' of the approximation using a smoothing parameter. The smoothing parameter is optimised by the generalised cross-validation [c.f. *Stickel*, 2010]. Comparison of the power spectral density functions of the smoothed and unsmoothed data (Figure 2.1) shows they diverge at scales less than 10 km. The smoothing therefore precludes plumes at scales smaller than 10 km from being reliably detected.

In the context of this analysis, a plume is defined as an occurrence of elevated mass mixing ratio above the background level. Based on this premise, a simple algorithm for plume identification is developed. In the first step, local maxima and minima present in the data are identified. A threshold MMR level for a plume is defined. All maxima above this level are considered plume peaks, and the scale of the plume is quantified by the distance between the two local minima on either side of the peak. Any overlapping plumes are merged into one larger plume. A threshold MMR is used so that only peaks above the ambient background level are identified as plumes.

As a rough measure of the background level, the threshold MMR level for each mission is set to the standard deviation of BC MMR from that mission, corresponding to values of 11, 11, 36, 7, and 21 ng/kg-air for each of the five HIPPO missions. The sensitivity of the plume identification algorithm to the value of the threshold was tested by varying the value from 5 to 50 ng/kg-air for each HIPPO mission. The median spatial scale of the identified plumes was found to vary between 84 and 117 for the five HIPPO missions, with HIPPO4 having the highest variation and HIPPO3 having the lowest.

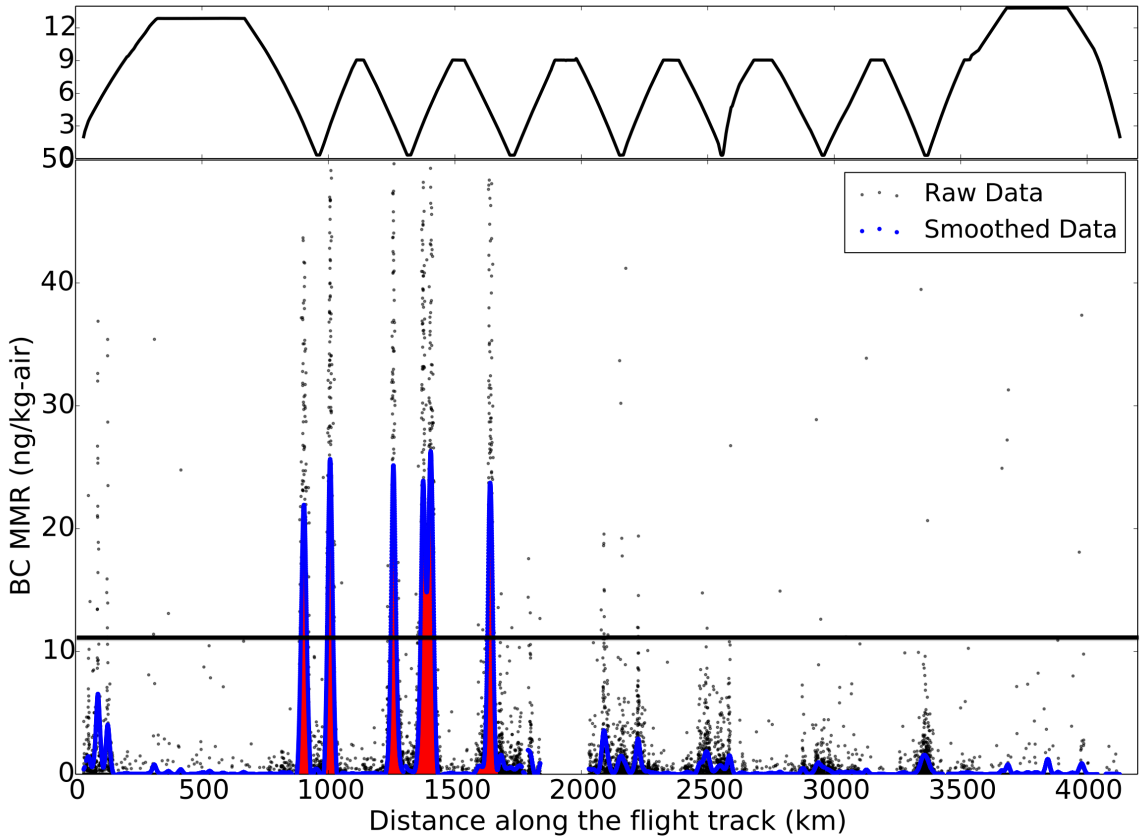

Figure 2.2: An example of how the plume detection algorithm works. This figure shows the five plumes identified on the January 16, 2009 flight during HIPPO1 in the bottom panel, and the altitude of the flight track in the top panel. The grey points represent the unsmoothed HIPPO data, and the blue line is the HIPPO data smoothed by regularisation. The black horizontal line shows the threshold MMR level, and the red-shaded areas represent the plumes identified during the flight.

Because the HIPPO campaign consists of a series of slant vertical profiles, the plume scales cannot be fully separated into their horizontal and vertical components. As such, the plume scale in this analysis is a 'scale along the (slanted) flight track' rather than a horizontal or vertical scale. Figure 2.2 shows an example of the smoothed versus unsmoothed HIPPO data as well as the plumes identified on January 16, 2009 during HIPPO1. The measured scales of the five plumes identified on this day, from left to right, are 56, 51, 99, 113, and 45 km.

Table 2.2: Results from statistical analysis of plumes detected during the five missions of the HIPPO campaign. Total BC refers to the total amount of black carbon measured during that mission of the HIPPO campaign. Total BC Mass in FT is the total mass of BC in the free troposphere, i.e. excluding mass measured at altitudes lower than 2 km. 'Mass in Plumes' is the total mass detected in plumes (in ng) and as a percentage of total BC mass in the free troposphere (in parentheses.)

Campaign Mission	# of Plumes	Median Scale (km)	Total BC Mass (ng)	Total BC Mass in FT (ng)	Mass in Plumes (ng, %)
All	208	98	20.3	13.5	9.6 (71)
HIPPO1	24	112	2.7	1.4	1.1 (76)
HIPPO2	60	89	3.0	2.3	1.6 (70)
HIPPO3	44	100	6.9	5.8	4.3 (75)
HIPPO4	44	124	1.9	1.1	0.76 (69)
HIPPO5	36	81	5.8	2.9	1.8 (62)

2.2 Results and Discussion

2.2.1 HIPPO Plume Statistics

A total of 259 BC plumes were identified during the campaign. Fifty-one of these plumes were located at altitudes less than 2 km and were likely the result of sampling polluted boundary layer air. These plumes are not demonstrative of BC plume scales and are not included in the analysis, leaving a total of 208 plumes. Table 2.2 provides a summary of the plume statistics from each mission. The plumes encompass a large spread of scales, ranging from 34 km to 607 km, with a median of 98 km.

HIPPO1 contains the smallest number of plumes, while HIPPO2 contains the most with 2.5 times more plumes than HIPPO1. HIPPO5 has the smallest median plume scale and HIPPO4 has the largest. The largest amount of BC mass was encountered during HIPPO3. These various trends could be due to rainfall, source, and transport differences between missions, which will be further explored in the following sections. Also note that 71% of the total BC mass measured above 2 km (or 48% of total BC mass measured) from the campaign is found within the identified plumes, highlighting the important contribution of plumes to total BC present in the atmosphere.

Figure 2.3 shows the histogram of all detected plume scales during the HIPPO

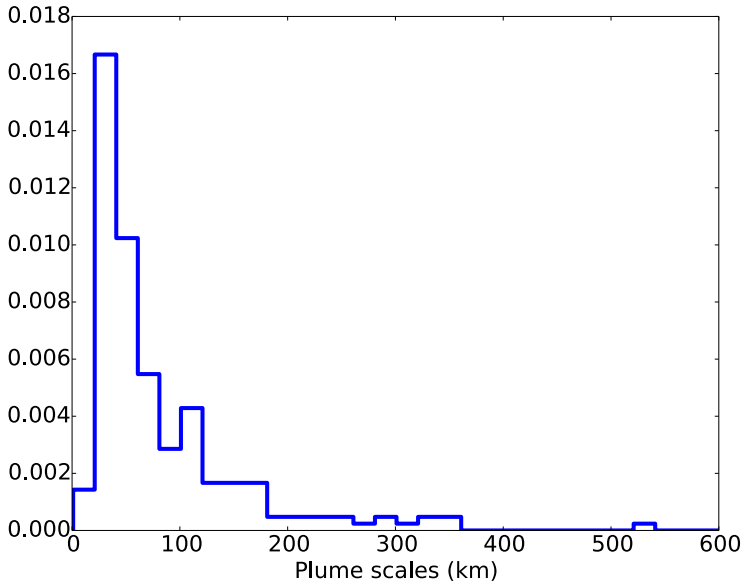

Figure 2.3: Shows the histogram of slant plume scales identified during all 5 HIPPO missions.

campaign. While the median is 98 km, one can see from this figure the large number of small scale plumes having scales of 20–60 km. There exist much larger plumes (> 200 km); however, they occur at a much lower frequency.

Another issue to consider is that if BC plumes were distributed in thin vertical layers with continuous horizontal extent, then this analysis method would detect those layers as a series of plumes where the analysed spatial scale was set by the thickness of the layers and the ratio of the vertical and horizontal speeds. The impact of this artefact is likely small since the majority of plumes were identified during different flight legs and non-consecutive vertical profiles with a variety of peak concentrations and altitudes. However, it could potentially affect some of the identified plume scales and is an acknowledged limitation of the analysis.

2.2.2 Spatial Distribution of Plumes

Figure 2.4 shows the locations of the identified plumes. The majority of plumes are located in the Northern Hemisphere in areas over the Pacific Ocean (blue region), North Pole (purple), and North America, with relatively few plumes in the Southern

Hemisphere (green). This is likely primarily due to the relative lack of BC sources contributing to loadings in the South Pacific Ocean.

Extensive research in pollution transport to the Arctic region has shown that Arctic air masses can be influenced by long-range transport from biomass-burning and anthropogenic source regions at lower latitudes, especially in winter and early spring [e.g. *Stohl*, 2006]. Arctic plumes may also arise from direct injection of BC into the troposphere near its source by local biomass burning events, as was the case for plumes detected during the ARCPAC campaign [*Warneke et al.*, 2009; *Koch et al.*, 2009], which sampled BC plumes in the Alaskan Arctic region in April 2008. The plumes detected in this campaign were attributed to agricultural fires in Kazakhstan and southern Russia, and forest fires in Siberia. These types of sources could have similarly contributed to the presence of the HIPPO Arctic plumes. The large number of HIPPO plumes identified in the North Pacific region are also likely due to similar transport mechanisms. *Holzer et al.* [2005] showed that significant amounts of East Asian air are transported across the Pacific Ocean, particularly from March to August. *Schwarz et al.* [2010a] attributed northern Asia as a likely source region for the BC detected in HIPPO1.

The side panels of Figure 2.4 show that most regions contain plumes with a wide range of scales spanning altitudes from 2 to 13 km. While no distinct pattern is present, the majority of plumes were detected in the mid-troposphere. The different sources and transport mechanisms of BC in these regions likely contribute to the wide range of observed plume scales. Midlatitude synoptic low pressure systems can carry biomass burning plumes from Asia and Eastern Europe over the Pacific Ocean, and these plumes can be sheared horizontally into fine-scale filaments and layers as they exit the cyclonic systems. These layers have been observed in the free troposphere in both Arctic and Pacific regions in previous observational campaigns [*Brock et al.*, 2011; *Liu et al.*, 2003]. This mechanism may contribute to the large number of small-scale HIPPO plumes observed at mid-tropospheric altitudes.

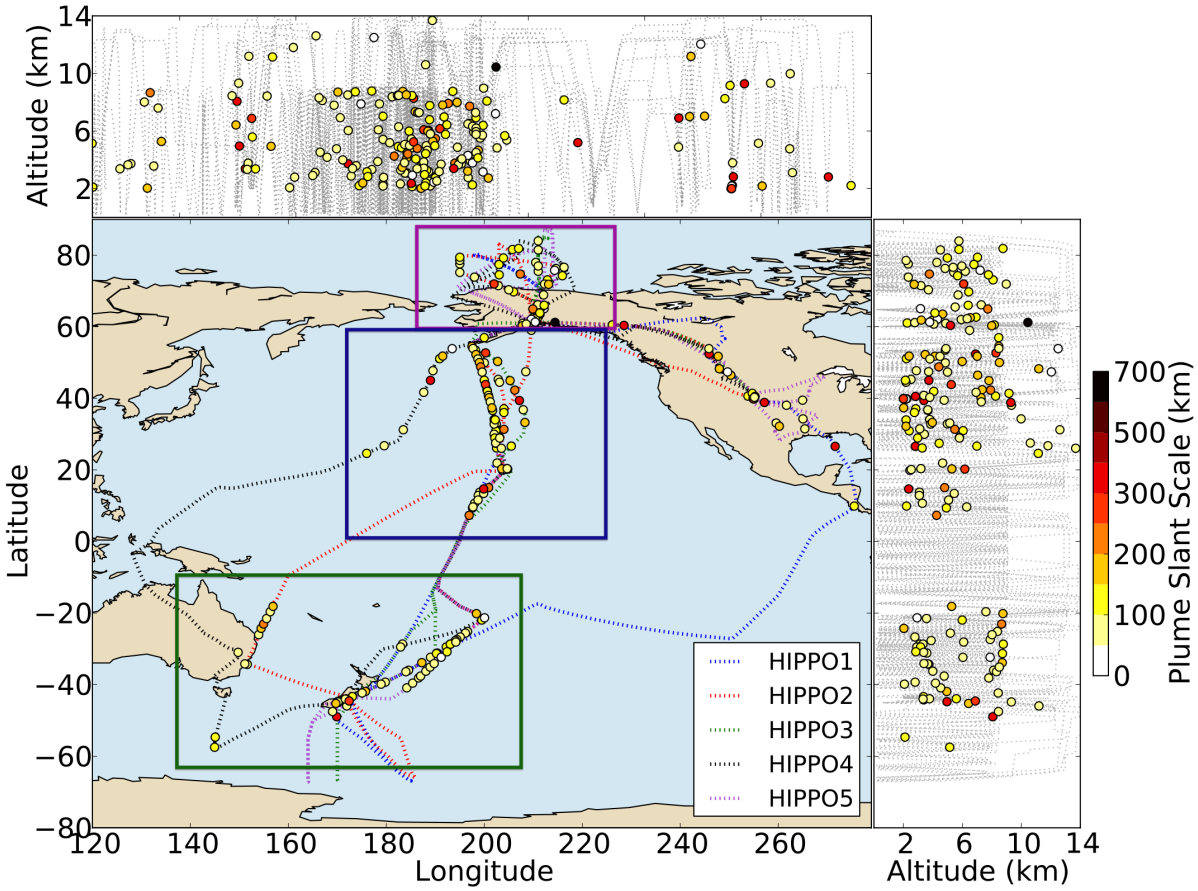

Figure 2.4: The centre panel shows the location of each plume peak along the flight track of the five HIPPO missions. The right and top panels show the altitudes of the corresponding plume peaks as a function of latitude and longitude, respectively. The grey dotted lines in each side panel represent the flight track of the entire campaign. The colour bar is the plume slant scale in kilometres. The coloured boxes represent different regions with the Arctic in purple, the North Pacific in blue, and Australia/South Pacific in green.

2.2.3 Plume Composite

To gain a better understanding of the general characteristics and overall shape of BC plumes, a composite of all plumes is produced. This is done by taking each plume and re-gridding the distance along the flight track to distance from plume peak at 0.5 km equal spacing. The composite is then created by determining the median MMR at each 0.5 km interval away from the plume peak. The blue line in Figure 2.5 depicts the composite of all 208 identified plumes, and the top panel indicates the number of plumes averaged in each 0.5 km bin. Only bins with 25 or more plumes

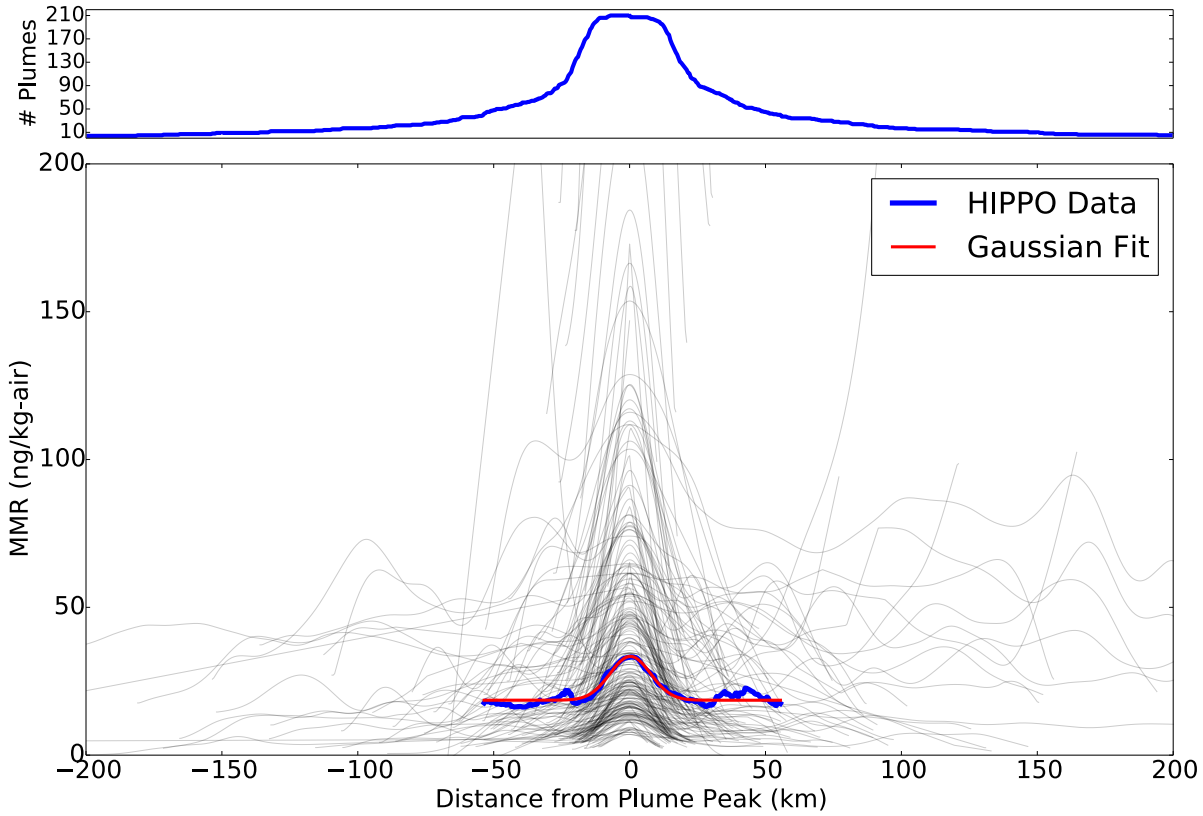

Figure 2.5: A composite of all plumes is represented by the blue line. The top panel shows the number of plumes included in each composite bin; only bins with at least 25 plumes are depicted in the composite. The red line is a Gaussian fit to the composite. The gray lines represent the individual identified plumes.

are included in the composite. The plume composite has a clear Gaussian shape, so to quantify its scale, a Gaussian function is fit to the composite peak according to Levenberg-Marquardt least-squares minimization. The scale of the composite plume is approximated to six times the standard deviation of the Gaussian, which encompasses 99.7% of the area under the curve. This approximation is chosen so that the definition of the composite plume scale is comparable to the definition of the scale of the HIPPO plumes, which is defined by the distance between two minima on either side of the plume peak. The Gaussian has a standard deviation of 11 km, and so the scale of the composite plume is approximately 66 km. The composite structure was insensitive to the disparate peak values of the various plumes; normalization of the plumes before compositing did not affect this result.

The scale of the composite plume is considerably less than the value of the median

plume scale (98 km); however, this is due to the fact that the composite is more representative of smaller scale plumes. This is visible in Figure 2.5, which includes the re-gridded HIPPO plumes, centred at their peak. One can see, as the distance from the peak increases, most of the plumes drop off at distances less than 100 km from the peak until only the broader, less Gaussian plumes remain. Because the composite only includes bins with 25 or more plumes, the shape and scale of the composite reflect the high number of small-scale plumes, as confirmed by the histogram presented earlier (Figure 2.3).

2.2.4 Seasonal Differences

A useful feature of the HIPPO campaign is that the five missions took place at different times of the year, enabling one to gain insight into the seasonal differences in BC plumes over the Pacific region. The seasonal differences are explored in Figure 2.6, which shows the spatial distribution of the detected plumes colour-coded by HIPPO mission, and Figure 2.7, which shows the relative peak concentration of BC plumes in each mission using the compositing technique from Section 2.2.3.

These figures show several interesting features. Firstly, one can see that the large number of plumes in the North Pacific were primarily detected during HIPPO3 and HIPPO4, which took place in March/April and June, respectively. As discussed in Section 2.2.2, these plumes are likely the result of long-range transport from East Asia, which is most efficient at this time of year. *Holzer et al.* [2005] quantified the transport of air from the industrialized regions of East Asia and found that during March-April-May, East Asian air is particularly well exported and travels almost exclusively east toward North America. The climatology as well as event composites show that East Asian air is lofted slantwise into the mid troposphere in March-April-May, consistent with warm-conveyor-belt transport and quasi-isentropic mixing. During June-July-August, there is also transport across the Pacific; however, nearly half of the East Asian air moves westward to the Middle East [*Holzer et al.*, 2005]. The individual

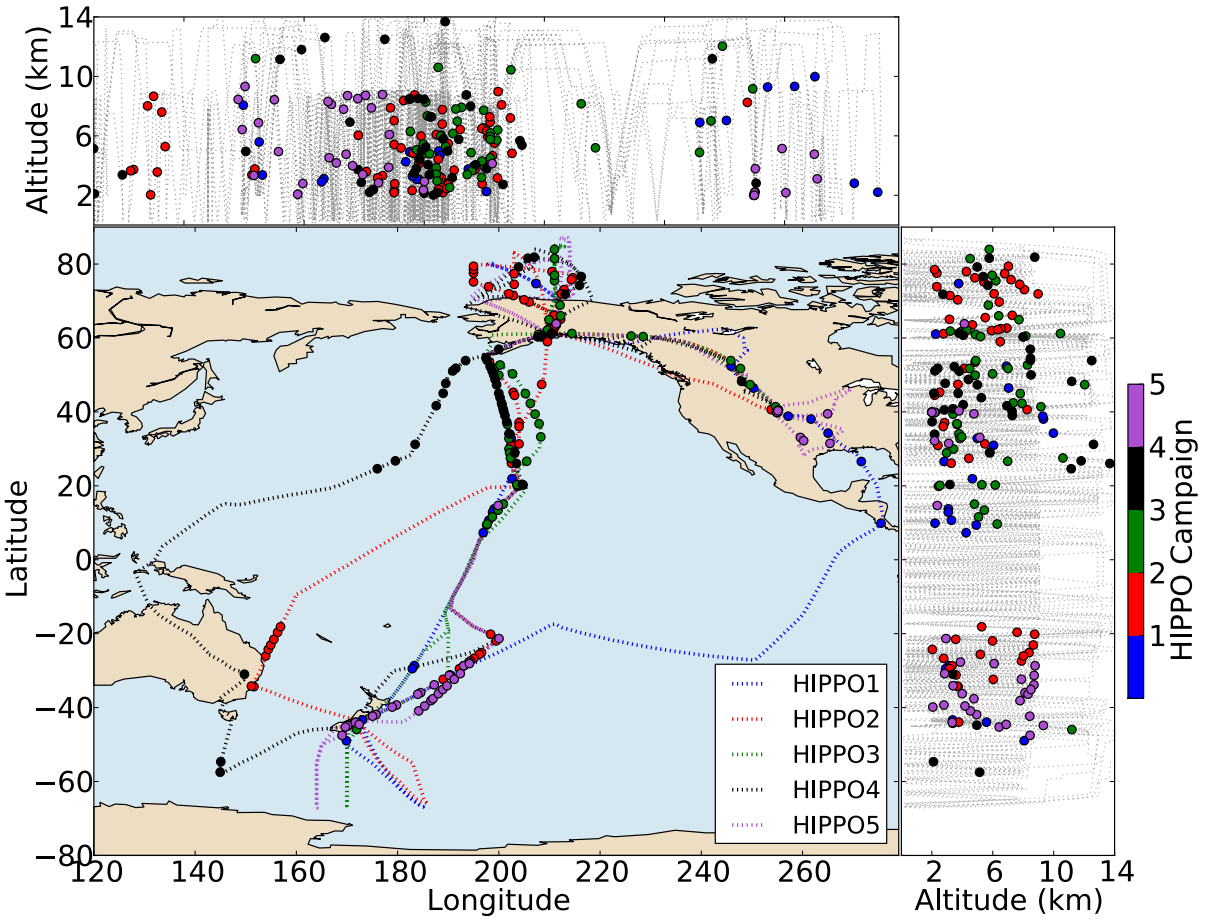

Figure 2.6: The large centre panel shows the location of each plume peak along the flight track of the five HIPPO missions. The right and top panels show the altitudes of the corresponding plume peaks as a function of latitude and longitude, respectively. The gray dotted lines in each side panel represent the flight track of the entire campaign. The points are colour-coded to the mission during which the plume was measured to provide insight on the seasonality of the detected plumes.

plume composites from Figure 2.7 show that the median mass mixing ratios are much higher for HIPPO3 than HIPPO4, consistent with greater transport of air during HIPPO3.

One can also see a smaller collection of plumes off the coast of Australia and New Zealand, primarily from HIPPO2 and HIPPO5, which took place in November and August/September, respectively. These plumes are likely due to biomass burning events in Australia and New Zealand. Fire counts in this region from global satellite data show that peak emissions occur from late August to early November [*Generoso et al.*, 2003]. HIPPO5 shows a higher median mass mixing ratio than HIPPO2 (Figure

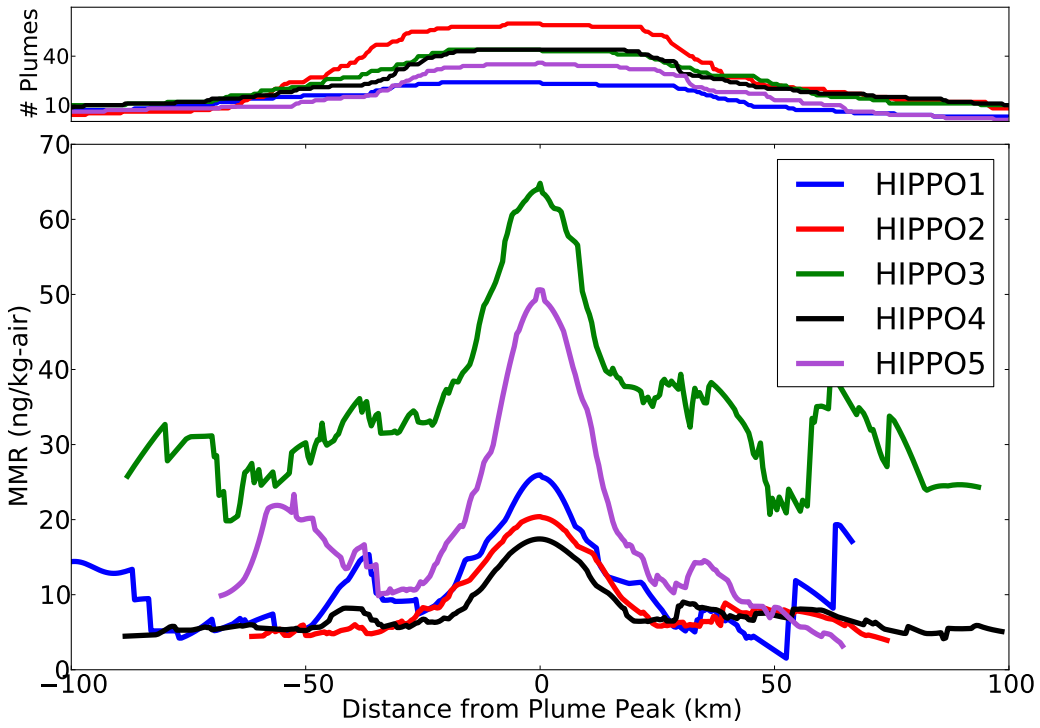

Figure 2.7: Composites of the plumes identified in each mission are pictured in the main panel. The different colours represent the different HIPPO missions. The top panel shows the number of plumes included in each composite bin; only bins with at least 20% of plumes detected from each mission are depicted in the composite.

2.7), which is likely because September tends to have relatively higher emissions than November in this region.

HIPPO2 also detected a large number of small scale plumes in Arctic in October-November. The relatively small scale of these plumes compared to other HIPPO missions could be indicative of local sources of BC since long-range transport to the Arctic tends to occur in early Spring [*Stohl*, 2006].

2.2.5 Comparison to Effective Model Resolution

Because the identified plume scales have both horizontal and vertical components, comparing these scales to a GCM's horizontal resolution is an inaccurate way of quantifying a model's ability to resolve these plumes, since this disregards the GCM's

vertical resolution. In order to make an accurate comparison between the HIPPO plume scales and typical GCM resolutions, one can define an approximate 'effective model resolution', which takes into account the flight track geometry of the HIPPO campaign and the vertical resolution of the model. A typical modern GCM for use in climate modelling has a horizontal grid spacing of 1–2° (100 - 200 km at the equator) and a vertical grid spacing in the range of a few hundred metres up to a kilometre (at altitudes in the range of the identified plumes). To calculate an 'effective model resolution', the slope of each vertical profile from HIPPO and the height of a typical tropospheric vertical level in a GCM (varied from 300 m to 1 km) are used to calculate the total distance traveled through a grid box. These distances vary from 4 km for the lowest altitudes and steepest slopes to 58 km for higher altitudes and shallower climbs. If the minimum resolvable wavelength of a numerical model is approximated to be four times the model grid spacing (an optimistic estimate according to some authors [e.g. *Walters*, 2000]), then the effective model resolution is in the broad range of approximately 20 – 230 km. Eighty-eight percent of the identified plumes (65% of the plume mass) are smaller or of similar magnitude to this range.

2.2.6 Autocorrelation Analysis

To relate this work to previous attempts to quantify aerosol scales of variability, autocorrelation analysis is performed on the unsmoothed data from each HIPPO mission, similar to the analysis of satellite data by *Anderson et al.* [2003]. Because this analysis is performed on all data from each HIPPO mission rather than the detected plumes, it provides the opportunity to link the scales of BC plumes to the variability of overall measured BC.

Figure 2.8 shows the average daily spatial autocorrelation for each HIPPO campaign as a function of lag (in kilometres). The autocorrelation functions were derived from the power spectral density distributions using the Wiener-Khinchin theorem. A high autocorrelation represents a low degree of variability, and a decreasing autocor-

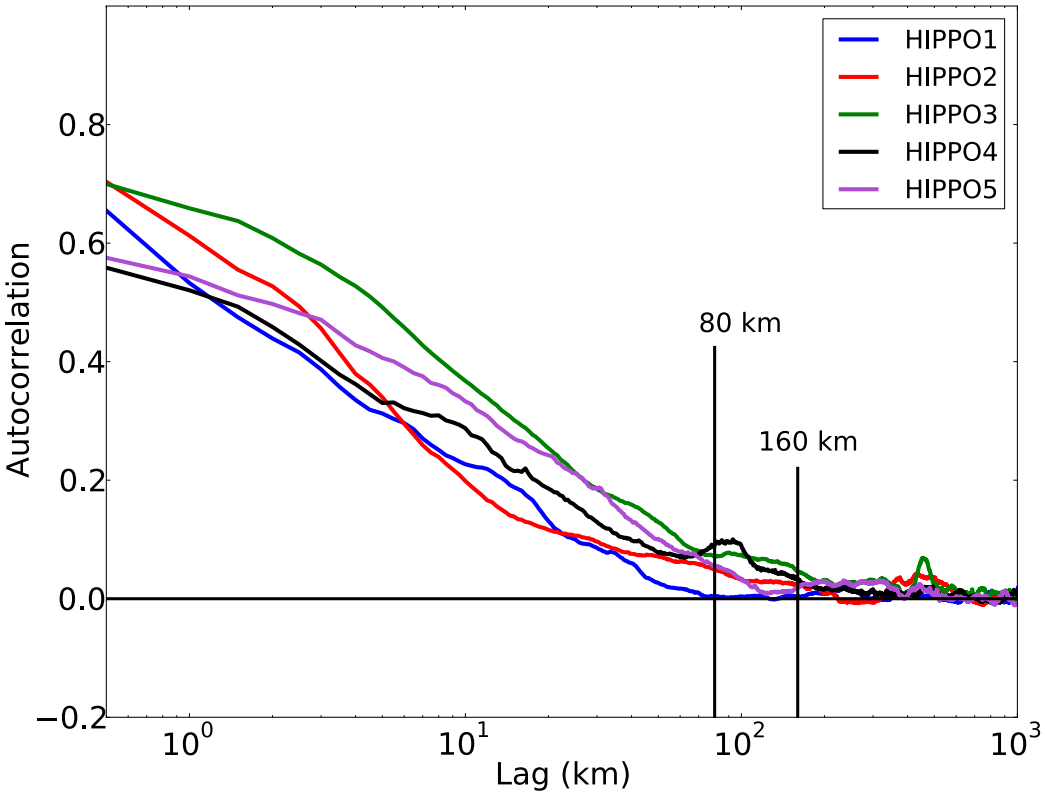

Figure 2.8: The average daily spatial autocorrelation as a function of lag (in km) for the five HIPPO missions.

relation indicates an increase in variability with increasing lag. The autocorrelation of all five missions drops off rapidly, with HIPPO1 reaching a plateau of nearly zero correlation at a lag of 80 km, and the other HIPPO missions reach a near-zero plateau at approximately 160 km, after which the five curves become rather noisy. This signifies that most of the BC variability exists at scales below ∼80 – 160 km. These scales are of similar magnitude to the along-track scales of the HIPPO plumes, suggesting that a large degree of BC variability is accounted for in these plume structures. *Anderson et al.* [2003] found a similar range of scales for the variability of aerosol optical depth (40 – 160 km). Their analysis included spaceborne lidar data and aircraft data from level segments of flight legs, ensuring that their measured scales of variability represent strictly horizontal scales. Because of the nature of the HIPPO flights, the data is unable to be separated into horizontal and vertical components; however, the agreement between HIPPO scales of variability and those determined by *Anderson et al.* [2003]

could be indicative of the HIPPO scales having a substantial horizontal component.

2.3 Summary and Implications

This chapter quantifies the scales of variability of BC plumes identified during all five missions of the HIPPO aircraft campaign, and determines how these scales relate to current GCM resolutions used in climate modelling simulations. A total of 208 plumes were identified during the campaign. These plumes represent a large portion (71%) of the total mass of BC measured in the FT during the campaign, confirming that these plumes are important features of BC in the atmosphere. The majority of plumes were detected over the North Pacific Ocean and the Arctic, with a small number of plumes detected in the Southern Hemisphere off the coast of Australia and New Zealand.

Statistical analysis of the plume characteristics show that the median plume scale is 98 km. A plume compositing technique, which favours the high number of small-scale plumes, reveals that a typical BC plume has a Gaussian shape and a scale of approximately 65 km. From these two analyses, one can infer that a typical BC plume scale is in the range of 65 – 100 km. Autocorrelation analysis reveals that most of BC's variability occurs on scales smaller than 80 – 160 km, which is similar in magnitude to previous studies of aerosol horizontal variability. This range of total BC variability overlaps considerably with the range of BC plume scales, suggesting that a large portion of the BC variability can be accounted for by these plume structures.

Comparing the along-flight-track scale to an 'effective model resolution' shows that most of the measured plumes exist on scales that are smaller or of similar magnitude to the effective model resolution, which ranges from 20 km for low altitudes and steep ascents to 230 km for high altitudes and shallower ascents. Large-scale plumes ($>$ 230 km) and plumes located at low altitudes with significant vertical structure are likely resolvable by a typical GCM; however, plumes representing horizontal features at these scales are too small to be captured by GCMs running at climate modelling resolutions. The agreement between HIPPO scales of variability and previous calculations of hori-

zontal aerosol variability, suggests that the HIPPO plumes have a significant horizontal component. Although the identified plume scales are roughly half the size of GCM resolutions, the capabilities of GCMs are rapidly increasing, and running climate model simulations at twice the resolution will likely be possible in the near future. Because BC plumes represent a large portion of total BC in the atmosphere and account for a large degree of its variability, it is crucial for aerosol models to capture these features in order to accurately describe BC's effect on radiative forcing and the climate.

Chapter 3

Simulated plume scales and their dependence on model resolution

Chapter 2 quantified the scales of black carbon plumes over the Pacific ocean as measured by the HIPPO aircraft campaign. The results showed that typical black carbon plumes had spatial scales on the order of 100 km, suggesting that plumes characterised predominantly by their horizontal variation at these scales are too small to be captured by GCMs running at resolutions currently suitable for climate simulations.

This chapter seeks to build upon the results from Chapter 2 by comparing the scales of observed plumes to those simulated by global climate models. Global climate models are unable to resolve aerosol variability that exists on scales smaller than a model grid-box, and it is important to understand how this inability to resolve sub-grid scale variability affects model simulations of important aerosol features, such as plumes. The aim of this chapter is to explore the impact of a model's ability to resolve variability on aerosol plume scales by applying the plume identification analysis from Chapter 2 to plumes simulated by global climate models at varying resolutions. The analysis is performed using two global aerosol-climate models: ECHAM6-HAM2 and HadGEM3-UKCA [1]. The analysis focuses primarily on the ECHAM6-HAM2 simulations, which

[1]It should be noted here that while I designed the study and analysed the model output, the model simulations were conducted by fellow group members Dr. Nick Schutgens and Dr. Zak Kipling.

are conducted at three different resolutions: 1) a baseline resolution representing the typical resolution current GCMs are able to run for climate simulation purposes, 2) a coarse resolution typical of older generation GCMs and 3) a high resolution currently feasible for short term climate simulations.

A further test is performed using two configurations of HadGEM3-UKCA: 1) a configuration with a similar resolution to the ECHAM baseline simulation but with an outdated description of convective scavenging, and 2) an updated baseline configuration at the same resolution, which includes an improvement to the model's convective scavenging routine. These additional tests enable the analysis of the impact of improving aerosol processes (as opposed to increasing resolution) on black carbon plume scales. They also enable the comparison of plume scales simulated by different models with similar resolutions.

In addition to comparing observed and simulated plume scales, this study takes advantage of global climate models' ability to simulate three-dimensional aerosol fields at all points in time by exploring the horizontal and vertical extent of the identified plumes — a feature that could not be investigated with the HIPPO aircraft measurements due to the slanted nature of the flight track and their limited spatial coverage.

3.1 Observational Data Set

The data used in this analysis come from the HIAPER Pole-to-Pole Observations (HIPPO) aircraft campaign. The HIPPO campaign measured black carbon (BC) over the Pacific Ocean during five missions, taking place during different seasons from January 2009 to September 2011. Further details are provided in the previous chapter in Section 2.1.1.

3.2 Models

Two global aerosol-climate models are used in the plume scale analysis: ECHAM6-HAM2 and HadGEM3-UKCA. For an evaluation of the performance of ECHAM and HadGEM compared to observed BC burdens and vertical profiles of mass mixing ratios as measured by HIPPO see *Kipling et al.* [2013].

All simulations were run from July 2008 to the end of September 2011 to cover the HIPPO campaign period. A six-month spin-up period was allowed before the start of HIPPO1, with the meteorology nudged to European Centre for Medium- Range Weather Forecasts (ECMWF) ERA-Interim reanalysis data at six hourly intervals at 1.5° resolution. In the HadGEM3-UKCA simulations, potential temperature and horizontal winds were nudged, and in ECHAM6-HAM2, temperature, vorticity, and divergence are nudged toward ERA-interim reanalysis data.

3.2.1 ECHAM6-HAM2

ECHAM6 [*Roeckner et al.*, 2003; *Stevens et al.*, 2013] is the sixth generation atmospheric GCM developed by the Max Planck Institute for Meteorology. It has a spectral dynamical core, solving prognostic equations for vorticity, divergence, surface pressure and temperature in spherical harmonics with a triangular truncation. Tracers such as water vapour, liquid and ice hydrometeors, various trace gases and aerosols are advected with a semi-Lagrangian transport scheme [*Lin and Rood*, 1996] on a Gaussian grid. A hybrid sigma/pressure vertical coordinate is used.

The aerosol module used in ECHAM is the two-moment modal HAM 2.0 module [*Stier et al.*, 2005; *Zhang et al.*, 2012] based on the M7 framework [*Vignati et al.*, 2004], which describes the seven-modal microphysics. HAM calculates the global evolution of sulphate, sea salt, black carbon, particulate organic matter, and mineral dust in seven internally-mixed log-normal modes, four of which are hydrophilic and three hydrophobic. It simulates the formation and growth of aerosol particles due to nucleation and

condensation of sulphuric acid gas, coagulation of aerosol particles, and aerosol water uptake. The module is two-moment in that it simulates both aerosol mass and number concentration.

In ECHAM6-HAM2, removal processes such as wet deposition, dry deposition, and sedimentation are included. In-cloud scavenging assumes that a prescribed fraction of the available aerosol in each mode from the cloudy part of each grid box is embedded in cloud droplets and ice crystals and are removed at the rate at which large-scale cloud water/ice is converted to rain/snow [*Stier et al.*, 2005]. Scavenging in convective clouds is parameterised similarly by removing aerosol at the rate which water and ice are removed by convective precipitation. Where a fraction of the precipitation in a column evaporates before reaching the ground, the same fraction of the aerosol removed from the column is returned to the atmosphere.

Below-cloud scavenging describes the removal of aerosols due to collection by precipitation; the removal rate depends on the precipitation rate and area, and the collection efficiency [*Seinfeld and Pandis*, 2006]. Turbulent dry deposition is based on a surface resistance model following *Ganzeveld et al.* [1998] and depends on tracer concentration, air density and deposition velocity for each surface type. Sedimentation is described by Stokes theory and is only considered for the larger particles.

Primary emissions of BC come from the AeroCom II year 2000 emissions inventory [*Lamarque et al.*, 2010], which includes emissions from fossil fuel and biofuel burning. Biomass burning emissions come from monthly-mean fields from the Global Fire Emissions Database (GFED) version 2 [*van der Werf et al.*, 2006]. Emission data at various resolutions for ECHAM6-HAM2 is available for the year 2000 only. Since this study is not evaluating individual modelled plumes but only their size statistics, these emissions are likely sufficient for these purposes. BC emissions use a modified version of the AeroCom recommended size distributions, accounting for the width of the M7 modes. Fossil-fuel and biofuel emissions are added as a surface flux to the boundary-layer vertical diffusion equations, while biomass-burning emissions use

a biome-dependent vertical profile, as specified for AeroCom Phase I [*Dentener et al.*, 2006; *van der Werf et al.*, 2006]. BC aerosol is always emitted into the insoluble Aitken mode but can transition to the soluble modes by ageing through sulphate condensation and coagulation.

The configuration used in this chapter is atmosphere-only with sea surface temperatures derived from AMIP2 climatology. Because ECHAM6-HAM2 is a spectral model, it calculates its dynamics using spherical harmonics as opposed to grid points (non-linear terms and physical parameterisations are calculated on a Gaussian grid). Spectral models designate their horizontal resolution by a "T" number, which indicates the triangular truncation at the 'T'th harmonic, and their vertical resolution with an "L" number, which indicates the number of vertical levels in the model. In this study, ECHAM6-HAM2 is run at three different resolutions: 1) low resolution T31L19 with an approximate equivalent grid spacing of 3.75° and 19 vertical levels up to ∼10hPa (HAM Low), 2) baseline resolution T63L31 with an equivalent grid spacing of 1.875° and 31 vertical levels up to ∼10hPa (HAM Base), and 3) high resolution T127L95 with an equivalent grid spacing of 0.95° and 95 vertical levels up to ∼0.01hPa (HAM High). The 95 levels in HAM High combine the lower tropospheric resolution of L31 with considerable vertical extent into the middle and upper atmosphere. The L31 version was not yet available at T127 for this study, but the L95 version results in HAM High having approximately the same vertical resolution in the troposphere as HAM Base. These details are summarised in Table 3.1.

3.2.2 HadGEM3-UKCA

HadGEM3 [*Hewitt et al.*, 2011] is the third generation of the Hadley Centre Global Environmental Model developed at the UK Met Office. This study uses the uncoupled atmospheric component of the model with prescribed sea-surface temperature and sea ice fields. HadGEM3 has a non-hydrostatic, dynamical core and is fully compressible with a semi-Lagrangian transport scheme and hybrid sigma/pressure vertical

coordinate.

The chemistry scheme used with HadGEM3 is the standard tropospheric chemistry component of the UK Chemistry and Aerosols (UKCA) model [*O'Connor et al.*, 2014]. UKCA uses components of the Unified Model for the large-scale advection, convective transport, and boundary layer mixing of its chemical and aerosol tracers. The chemistry scheme includes 8 emitted species, 102 gas-phase reactions, 27 photolysis reactions and interactive deposition schemes.

The aerosol scheme in UKCA is the two-moment modal version of the Global Model of Aerosol Processes (GLOMAP-mode) [*Mann et al.*, 2010], which also follows the M7 framework. The set-up differs from HAM in that dust is not included in this UKCA configuration of GLOMAP-mode, so there are only five modes (four soluble, one insoluble) instead of seven. GLOMAP-mode simulates a number of processes over the aerosol life-cycle including size-resolved primary emissions, new particle formation, condensation, coagulation, and cloud-processing. Cloud processing is defined here to be the growth of aerosol particles by chemical reaction and uptake of gases while the particles exist as water droplets in non-precipitating clouds [*Mann et al.*, 2010].

A number of removal processes exist within GLOMAP-mode including aerosol dry deposition, sedimentation, nucleation scavenging and impaction scavenging. Removal by nucleation scavenging is calculated for both large-scale and convective-scale precipitation. In-cloud scavenging by large-scale precipitation assumes that 100% of the aerosol in the soluble accumulation and coarse modes is taken up by cloud water in the cloudy fraction of each grid-box and is then removed at the same rate at which the large-scale cloud water is converted to rain. Convective rainfall is treated similarly but assumes a cloud fraction of 30% and a conversion rate of 99% over 6 hours in all grid-boxes where convective rain is produced. Dry deposition and sedimentation are calculated following *Slinn* [1982] and *Zhang et al.* [2001].

Primary emissions of BC come from the AeroCom hindcast inventory [*Diehl et al.*, 2012], which includes emissions from fossil fuel, biofuel, and biomass burning through

to the end of 2006. These emissions are used for fossil fuel and biofuel burning sources; however, biomass burning emissions come from GFED2, as in ECHAM-HAM. Fossil-fuel and biofuel emissions are added to the lowest model level, while biomass burning emissions are distributed uniformly in height over levels 2 to 12 (approximately 50 m to 3 km) [*Kipling et al.*, 2013]. Like in ECHAM-HAM, BC is emitted into the insoluble Aitken mode but can transition to soluble modes through condensation and coagulation of sulphuric acid vapour and secondary organic material.

In this study, two versions of HadGEM3-UKCA are used, which differ only by their description of convective scavenging. The older version of HadGEM3-UKCA (UKCA OldScav) uses an operator-split approach to convective scavenging where aerosol is removed from the grid-box mean field after the convection scheme has run. In an updated approach (UKCA NewScav), the aerosol is removed directly from the tracer flux in the convective updraft, along with the removal of water by convective precipitation. The latter approach is the same as in the ECHAM6-HAM2 simulations. This updated approach was implemented by *Kipling et al.* [2013] and has been found to improve agreement in column BC burden when compared to HIPPO observations. As the two versions of HadGEM3-UKCA run at the same resolution, they are used to investigate how an improved description of an important aerosol process (i.e. convective wet-scavenging) can affect BC plume scales. It will also allow for the comparison of aerosol plume scales from two different GCM climate models operating at similar resolutions.

Both HadGEM configurations employed in this study have 38 vertical levels extending to a height of approximately 39 km. They have horizontal resolutions of 1.25° by 1.875°, which is nearly equivalent to the resolution of the ECHAM Base simulation. These details are also included in Table 3.1.

Table 3.1: Specifications of different model runs. The three ECHAM-HAM simulations are specified by the prefix HAM, and the HadGEM-UKCA simulations are specified by the prefix UKCA.

Run abbreviaton	Horizontal resolution	Vertical levels	Convective scavenging approach
HAM Low	3.75° x 3.75°	19 up to 10 hPa	In-cloud
HAM Base	1.875° x 1.875°	31 up to 10 hPa	In-cloud
HAM High	0.95° x 0.95°	95 up to 0.01 hPa	In-cloud
UKCA OldScav	1.25°x1.875°	38 up to 39 km (4 hPa)	Operator-split
UKCA NewScav	1.25°x1.875°	38 up to 39 km (4 hPa)	In-cloud

3.3 Methods

3.3.1 Flight Track Simulator

Before making comparisons between models and observations, it is important to be aware that models represent averages over horizontal and vertical dimensions, whereas in situ observations represent individual points in time and space. It is therefore inevitable that model calculations will result in deviations from measurements with substantial sub-grid variability. Many studies have shown that a significant portion of the departure between modelled and observed aerosol fields can be attributed to sub-grid spatial variation and non-representative sampling of model grid cells at the observation location [*Benkovitz and Schwartz*, 1997; *McComiskey and Feingold*, 2012].

Anderson et al. [2003], in their study of mesoscale variations of tropospheric aerosols, concluded that in situ measurements used for validation of models should be appropriately matched to the temporal and spatial scales of the models, but large-scale or long-term averages of in situ data should be used with caution because such averaging will tend to degrade correlations and mask important relationships.

In order to produce more meaningful comparisons between the HIPPO aircraft data and global climate model data, the model output is sampled at the same time and spatial locations as the aircraft measurements. This method was designed and implemented by *Kipling et al.* [2013], which is an adaptation of a flight track simulator

implemented by *Telford et al.* [2013] and *O'Connor et al.* [2005]. With this method, the instantaneous mass mixing ratio fields from the model are interpolated to points along the HIPPO flight track. The spatial interpolation is linear in log-pressure and both horizontal directions. Temporally, each observation is matched to the nearest following model time-step. ECHAM-HAM used time steps of 2400s, 720s, and 240s for HAM Low, HAM Base, and HAM High, respectively. Both HadGEM-UKCA runs had a time step of 1800s. Coupled with nudging to reproduce the observed synoptic conditions, this approach allows for close comparison of model data with the HIPPO observations while taking into account the meteorological conditions during the flight campaigns [*Brunner et al.*, 2003]. These point-by-point comparisons are particularly important in regions with filamentary structures or high fluctuations in tracer concentrations [*O'Connor et al.*, 2005].

3.3.2 Plume Identification

Initially, the same algorithm for plume identification as described for the HIPPO observations in Section 2.1.2 was carried out on the interpolated model output. However, this analysis revealed a limitation in the algorithm when applied to model data. The original algorithm relied on the detection of local minima in BC mass mixing ratio to define the plume's spatial scale as the distance between the two local minima on either side of the plume peak. The problem arises from the fact that the model data is much smoother than the observational data, and the simulated BC MMR tends to decrease monotonically from the lowest altitude to the highest altitude of a vertical profile. Therefore, the majority of local minima were detected at the peak altitude of the vertical profile. This resulted in model plume scales having values close to the distance traveled by the aircraft during vertical ascents and descents, rather than the actual horizontal or vertical scale of the aerosol layer.

Figure 3.1a provides a visual demonstration of this effect. The data presented in this figure are the flight-track interpolated model data from the HAM Low simulation

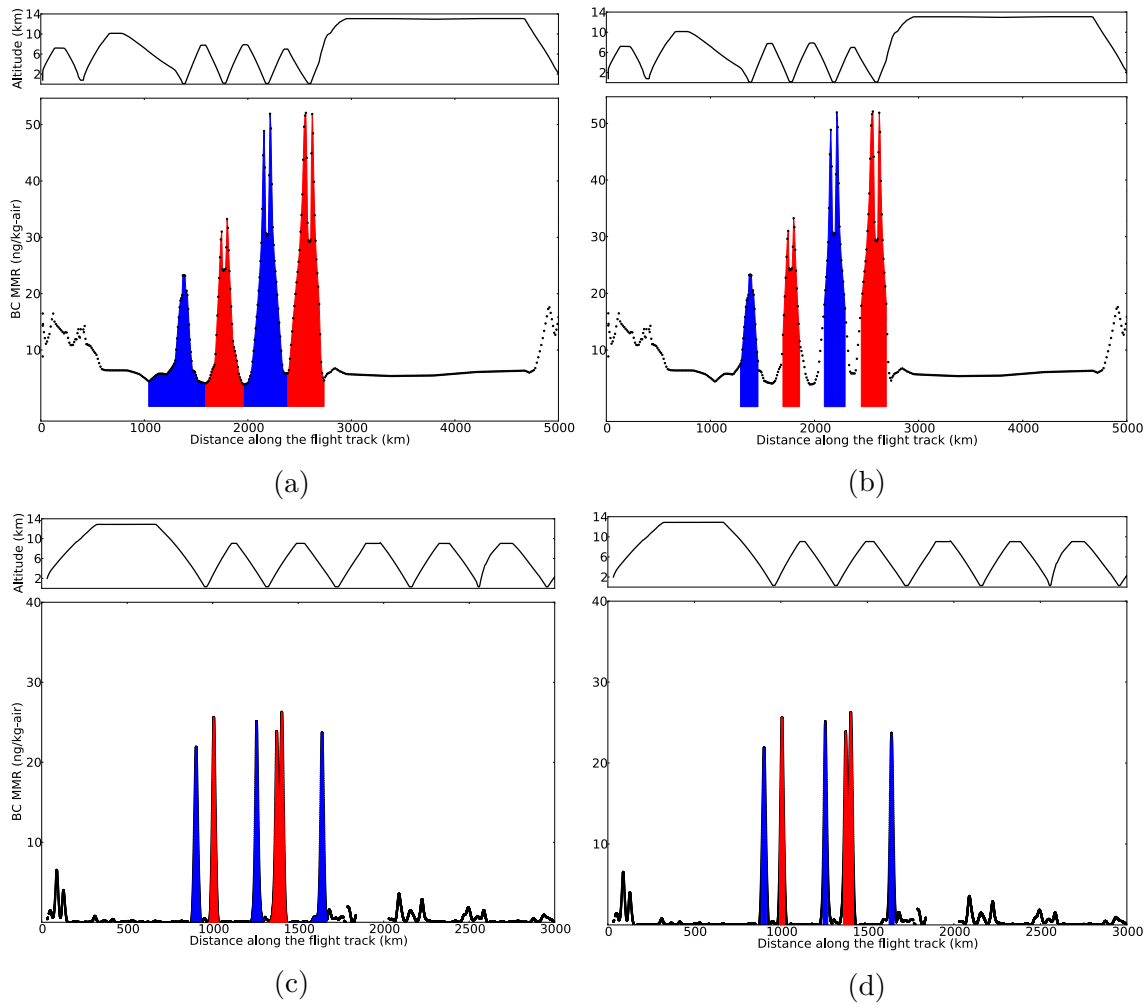

Figure 3.1: Demonstrates the difference in plume scales between the original plume algorithm in Chapter 2 (left) and the updated plume algorithm in this chapter (right). Figures (a) and (b) show the flight-track-interpolated BC mass mixing ratio from the ECHAM Low simulation on November 21, 2009 (HIPPO2). The red and blue patches represent the plumes identified during that flight. The top panels in each plot show the altitude of the aircraft as a function of distance along the flight track. Figures (c) and (d) show the measured BC mass mixing ratio from the HIPPO campaign on January 14, 2009.

on November 21, 2009 (HIPPO2). The red and blue patches represent plumes identified using the original plume identification method from *Weigum et al.* [2012]. One can see that the resultant widths of the plumes are artificially large, with their start and end points occurring at the peak altitudes in the flight track. To remedy this effect, the plume identification algorithm was altered so that the plume widths were redefined as the width of the plume at one third the plume's peak mass mixing ratio value. While the fraction 'one-third' was arbitrarily chosen to be representative of the actual plume

width, the fraction was varied from one-half to one-quarter of the peak value for each model run, and the median plume widths changed by 26 – 31%. More importantly, the relative differences in median plume peaks between the HIPPO observations and the different model simulations varied by less than 5%. Figure 3.1b shows the same plumes as Figure 3.1a but with the updated plume widths. The updated plume algorithm was also applied to the HIPPO observational data so that the definition of the measured plume scales are consistent with the simulated plume scales. Figures 3.1c and 3.1d show an example of the original plume widths (c) and the updated plume widths (d) for HIPPO observational data on January 14, 2009 (HIPPO1). Using the new method, the median plume scale from HIPPO observations decreased from 98 km to 56 km.

3.3.3 Analysis of 4D model fields

An advantage of using global climate models is that they are able to provide four-dimensional temporal and spatial coverage of the entire globe. While it is important that model data be appropriately matched to the temporal and spatial sampling of observational data when making comparisons between the two, analysis of the four-dimensional model output can provide further insight into these comparisons.

In this study, to complement the point-by-point model-observations comparisons provided by the flight track simulator, the variability in model fields is analysed using two additional techniques: 2D autocorrelation analysis and 3D plume detection. These techniques are applied to the ECHAM-HAM simulations, where the effect of resolution on BC variability can be explored.

Two-dimensional autocorrelation analysis

Two-dimensional autocorrelation analysis is used to quantify the scales of BC variability simulated in ECHAM-HAM, similar to the one-dimensional autocorrelation analysis employed in Chapter 2, which quantified the scales of BC variability in terms of distance along the flight track. Two dimensional autocorrelation analysis enables

the quantification of BC scales of variability in two dimensions, which is useful for evaluating simulated BC variability in terms of its latitudinal, longitudinal, or altitudinal scales. To compute the two-dimensional autocorrelation, the 4D model data is reduced to two dimensions by selecting a 2D area at a particular point in time (e.g. a latitudinal by longitudinal area at a particular vertical level, or a latitudinal by altitudinal area at a particular longitude). The 2D autocorrelation is calculated using the Wiener-Khinchin Theorem, by taking the real portion of the inverse two-dimensional Fourier transform of the two-dimensional power spectrum over the selected BC mass mixing ratios. In this study, 2D autocorrelation analysis is applied to a latitudinal by longitudinal area over the North Pacific Ocean and over East Asia to compare the difference in BC scales of variability in remote and near-source regions. The analysis is also applied to a latitudinal by altitudinal area over the North Pacific Ocean to compare the difference in horizontal and vertical BC scales of variability.

Three-dimensional plume detection

Three-dimensional plume detection works in a way similar to the plume analysis from Chapter 2, except instead of detecting plumes along the HIPPO flight track, it is able to detect 3D plumes and quantify their scales in both horizontal and vertical directions. In the 3D plume analysis, the definition of a plume remains the same as in the previous along-flight-track plume detection, which defines a plume as an occurrence of elevated mass mixing ratio above a background threshold value. All points within the three-dimensional area are classified as either plume or not plume based on whether the mass mixing ratio at that point exceeds the background level. The points classified as plumes that are next to other points classified as plumes are then grouped together as large-scale plumes using a technique called 'connected-component labelling' [*Stockman and Shapiro*, 2001]. This done by passing over the data twice as follows:

First pass: Iterate through each point in the analysis region. If the point is classified as a plume then test whether there are neighbouring points. If not, uniquely label the

point and continue. If so, find the neighbour with the smallest label and assign it to the current point.

Second pass: Iterate once again through each point in the analysis region. If the point is classified as a plume, then relabel the point with the lowest equivalent label.

This means that all plume points directly next to another plume point in at least one dimension are classified as one, large-scale plume.

This study is interested in using the 3D plume analysis to provide insight into the three-dimensional scales of the 1D plumes detected using the flight track simulator. To do this, each HIPPO flight is matched in time to the nearest 6-hourly 3D model output. At each of these time intervals, the 3D plume analysis is conducted over the globe using the same threshold level that was used during that particular flight for the 1D along-flight-track plume detection. Then, each flight-track-simulated plume (called FTS plumes from this point forward) that was detected during this time interval is co-located in space to the 3D plume in which it is found. One can quantify the average latitudinal, longitudinal, and vertical scale of the 3D plumes that match with each of the FTS plumes from the along-flight-track plume analysis.

The 3D plume detection was tested for sensitivity to the threshold value. It was found to be relatively insensitive to increases in the threshold value — increasing the threshold by 50% resulted in average spatial scales within 10–15% of the original values. Decreasing the threshold value tended to classify large portions of the globe as single plumes, which was not useful for this analysis. Using the same values as the FTS analysis allowed for easy co-location of FTS and 3D plumes and provided realistic plume scale values.

Table 3.2: Plume Statistics from simulated and observed plumes. Total BC mass is the sum total of all measured/simulated BC along the flight track. BC mass in FT is the sum total of all measured/simulated BC along the flight track in the free troposphere, i.e. excluding altitudes below 2 km. 'Mass in plumes' refers to the sum total of BC mass detected in plumes in ng and as a percentage of total BC mass in FT in parentheses.

	# of Plumes	Median Scale (km)	Total BC Mass (ng)	BC Mass in FT (ng)	Mass in Plumes (ng, %)
HIPPO	208	56	20	14	8.7 (64)
HAM Low	158	130	69	40	17 (43)
HAM Base	176	101	69	40	23 (58)
HAM High	187	92	69	41	24 (60)
UKCA OldScav	222	217	40	29	14 (47)
UKCA NewScav	96	95	23	13	4.4 (34)

3.4 Results

3.4.1 Along-flight-track plume analysis

The flight track simulator was implemented in all five model simulations (HAM Base, HAM Low, HAM High, UKCA OldScav, UKCA NewScav) to allow for comparison of simulated black carbon plume scales with the observed HIPPO plume scales. Table 3.2 provides a summary of the plumes statistics for both the observed and simulated plumes. With the updated plume algorithm, the median plume scale from the HIPPO observations is 56 km. Because the defined plume scales are smaller in the updated algorithm, the amount of black carbon measured within the plumes is less than with the original plume algorithm at 64% of the total measured BC mass in the free troposphere (compared to 71% in Chapter 2).

With respect to the ECHAM-HAM plumes, the lowest resolution simulation has the largest median plume scale at 130 km, which is approximately 2.3 times the observed median plume scale from HIPPO. As one would expect, the median plume scale decreases as the resolution of ECHAM-HAM is increased, with the median plume scales of HAM Base and HAM High having values of 101 km and 92 km, respectively. How-

ever, this decrease in plume scale is not as large as one might expect given that the horizontal resolution doubles between HAM Low and HAM Base and between HAM Base and HAM High; the plume scales show decreases of only 23% and 9%, respectively. Furthermore, the decrease between the baseline and high resolution run is much smaller than between the base-line and low resolution run. This could suggest that the scales of the FTS plumes are dictated by their vertical extent, since the vertical resolution in the troposphere does not change much between HAM Base and HAM High. It could also mean there are factors other than the model's inability to resolve sub-grid scale variability that cause the discrepancy between observed and simulated plume scales. For a view of the range of plume scales detected in simulation, Figure 3.2 shows the frequency distributions of plume scales for the three ECHAM-HAM and the two HadGEM-UKCA runs. Although HAM High and HAM Base have similar median scales, HAM High has a higher frequency of small scale plumes than both HAM Base and HAM Low. It also shows that HAM Low has higher frequencies at much larger scales (>250 km). Looking at the two HadGEM-UKCA runs, one can see that the version with the updated convective scavenging routine has a much higher frequency of small scale plumes and a much lower frequency of large scale plumes compared to the old convective scavenging simulation, confirming that the new convective scavenging routine leads to smaller scale plumes. However, all model runs underestimate the number of small scales plumes compared to the HIPPO observations (Figure 2.3).

Looking at the HadGEM3-UKCA results, the median plume scale from UKCA OldScav (217 km) is much larger than all other models and is nearly four times the observed HIPPO scale. The likely reason for this large discrepancy is the unrealistic description of convective scavenging in the baseline configuration. The median plume scale decreases to 95 km when the improved convective scavenging routine is employed in UKCA NewScav. This new plume scale is similar in size to the high resolution ECHAM-HAM run. The change in plume scale between the two HadGEM simulations is much larger than the change in the ECHAM simulations, suggesting that perhaps

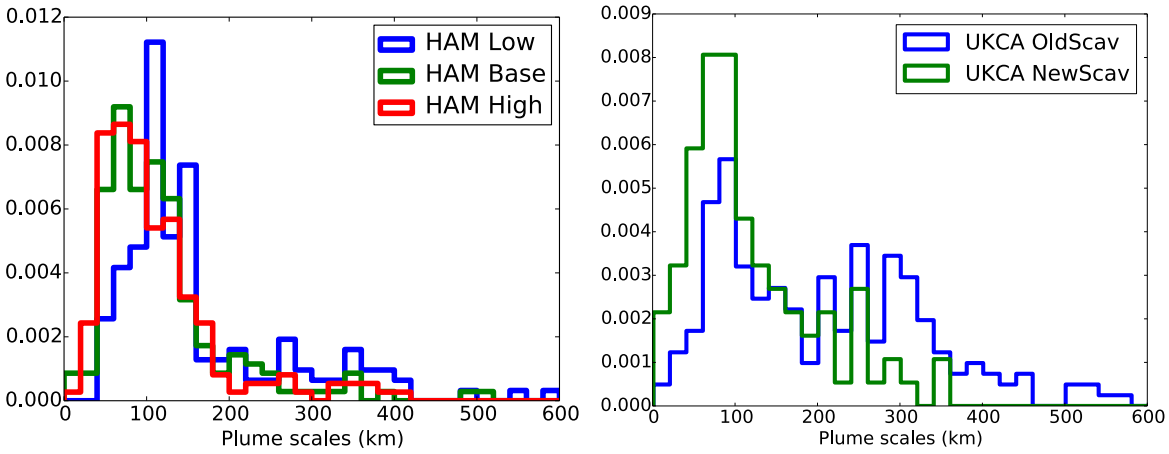

Figure 3.2: Histogram of ECHAM-HAM (left) and HadGEM-UKCA (right) plume scales (in km).

key aerosol processes such as wet scavenging have a larger impact on plume scales than model resolution. This suggestion requires further investigation and is discussed in the Future Works section of the concluding chapter.

Another notable difference between the observations and simulations is the total measured mass and the amount of mass in plumes. All models significantly overestimate the total amount of black carbon along the HIPPO flight track, except for UKCA NewScav, whose total BC mass is only marginally larger than that measured by HIPPO. In the case of ECHAM-HAM, this could be due to differences in emissions between observations and simulations, or differences in transport across the Pacific Ocean. Differences in emissions likely play an important role, as *Kipling et al.* [2013] found improvement between ECHAM5 simulations and HIPPO observations with increased temporal resolution of biomass burning emissions. Although the ECHAM-HAM simulations overestimate the amount of mass in plumes, the proportion of BC mass in plumes is similar to that of the HIPPO campaign for HAM Base and HAM High. HAM Low underestimates the proportion of mass in plumes; this could be due to the dispersive nature of the low resolution run causing BC plumes to spread out and mix with the background.

In the case of the HadGEM simulations, the overestimation of total BC mass in the UKCA OldScav simulation is likely due to the operator-split convective scaveng-

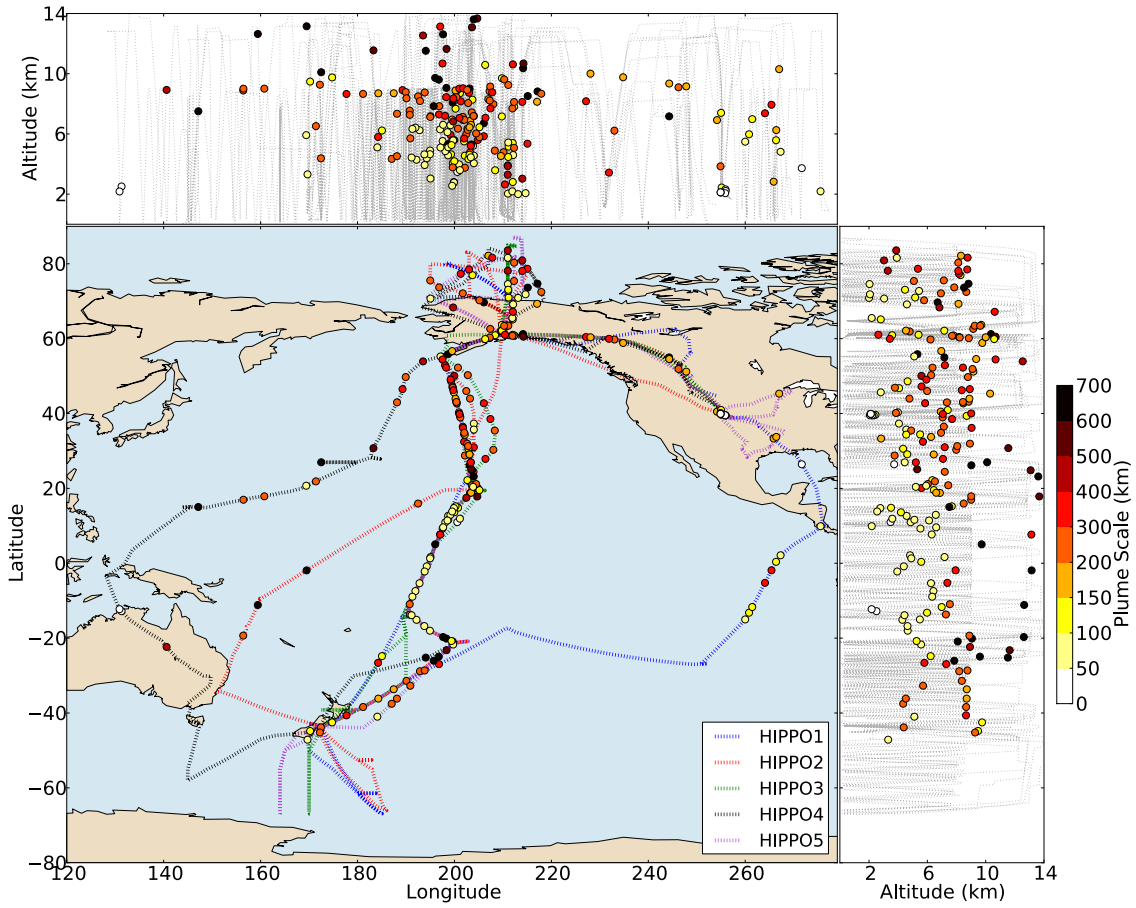

Figure 3.3: The large centre panel shows the location of each plume peak detected in the UKCA OldScav simulation where the model data has been interpolated to the HIPPO flight tracks. The right and top panels show the altitudes of the corresponding simulated plume peaks as a function of latitude and longitude, respectively. The grey dotted lines in each side panel represent the flight track of the entire campaign. The colour bar is the plume scale in kilometres.

ing routine not removing enough aerosol. The UKCA NewScav total mass matches the HIPPO total mass quite well; however, it underestimates the total mass of BC in plumes (and number of plumes). Therefore, the improved convective scavenging process appears to improve total simulated BC mass, but does not accurately distribute the mass into plumes. The difference between UKCA OldScav and UKCA NewScav plumes can readily be seen in Figures 3.3 and 3.4, which show the spatial distribution of the simulated plumes from each simulation. In UKCA OldScav (Figure 3.3) there are a high number of large-scale plumes found above 8 km, in the upper troposphere/lower stratosphere (UTLS) compared to the HIPPO plumes (Figure 2.4

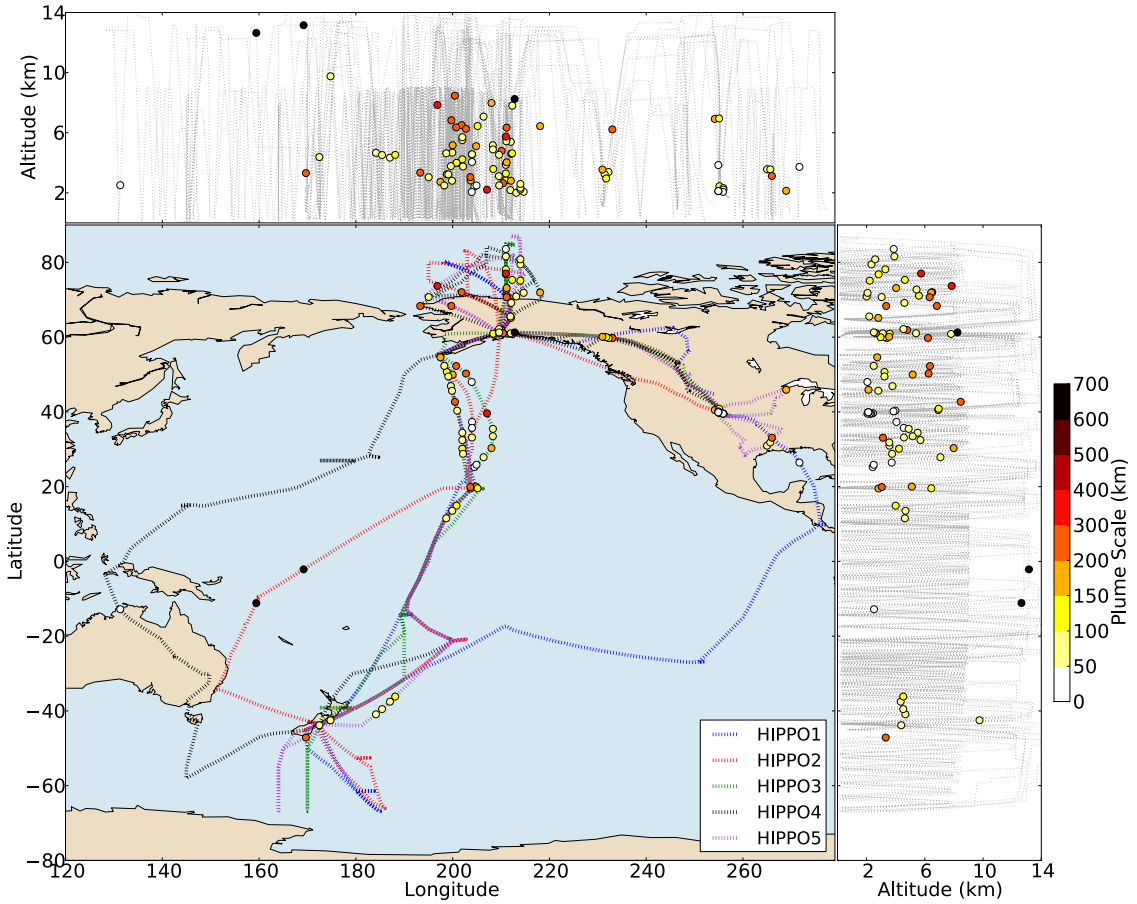

Figure 3.4: As Figure 3.3, except for UKCA NewScav.

from Chapter 2), which detected only a few small-scale plumes at these altitudes. Figure 3.4 shows that with the improved description of wet scavenging these spurious high-altitude plumes disappear, although it also clearly demonstrates the underestimation in total number of plumes in the UKCA NewScav run. This confirms that the operator-split convective scavenging routine in UKCA OldScav is incorrectly lofting large amount of BC into the UTLS where it is not being removed. This is in agreement with results from *Kipling et al.* [2013], who showed that the upper-tropospheric excess in UKCA OldScav is largely removed when the new convective scavenging routine is employed.

Figures 3.5, 3.6 and 3.7 show the spatial distribution of plumes simulated in the HAM Low, HAM Base, and HAM High simulations, respectively. One can see that the plumes are similarly distributed in the three ECHAM-HAM runs, with HAM Low and

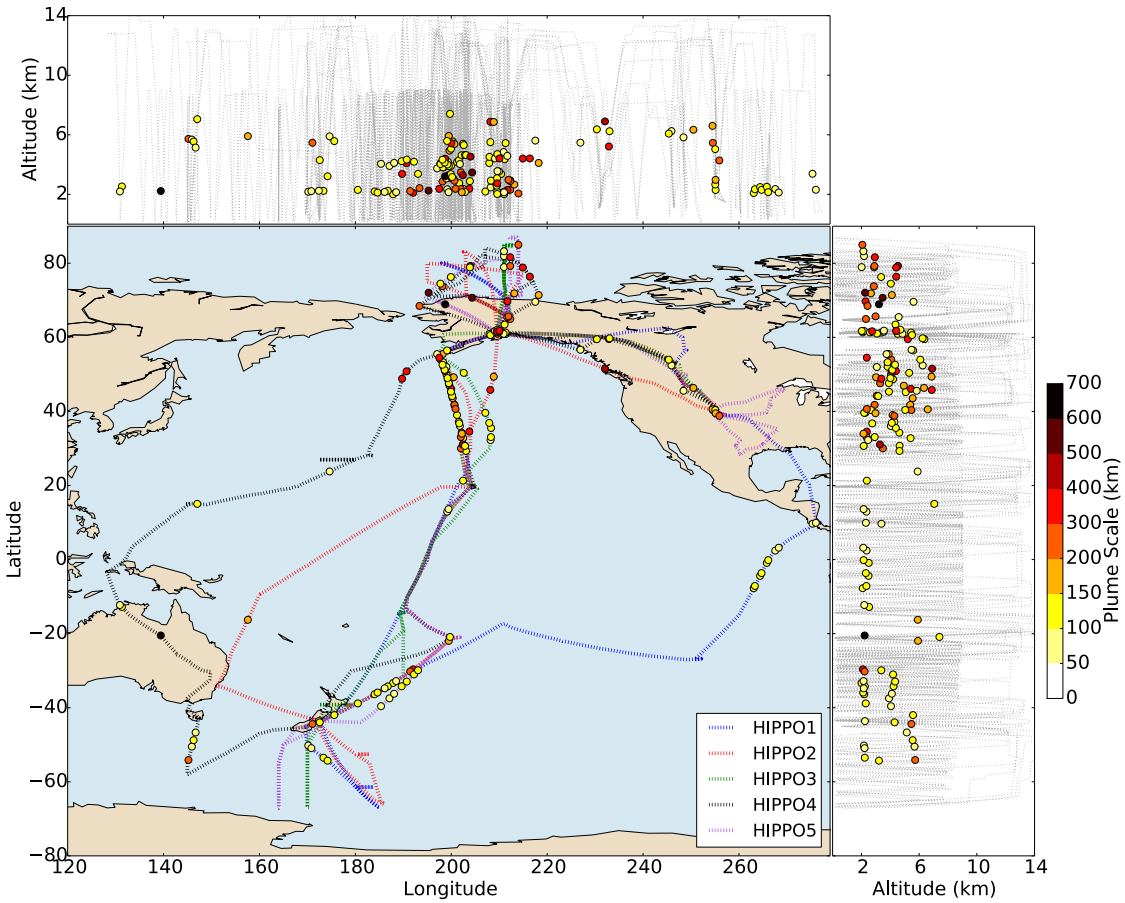

Figure 3.5: As Figure 3.3, except for HAM Low.

HAM High having slightly more plumes in the Southern Hemisphere. The ECHAM-HAM plumes are mostly concentrated in the mid-troposphere, over the North Pacific ocean, similar to the observed HIPPO plumes. However, they miss the large number of Arctic plumes detected during the HIPPO campaign as well as some of the higher altitude plumes. One can see that the model plumes are rarely detected at altitudes greater than 6–7 km. Several previous studies have also found that ECHAM-HAM underestimates poleward transport of aerosols to the Arctic [e.g. *Textor et al.*, 2006; *Bourgeois and Bey*, 2011; *von Hardenberg et al.*, 2012].

Plume composites provide a useful visual representation of the differences in plume scales between the observed and simulated plumes, as demonstrated in Figure 3.8. The composites for each model are created by the same method described in Section 2.2.3 in Chapter 2, except the composite peaks have been normalised to facilitate compar-

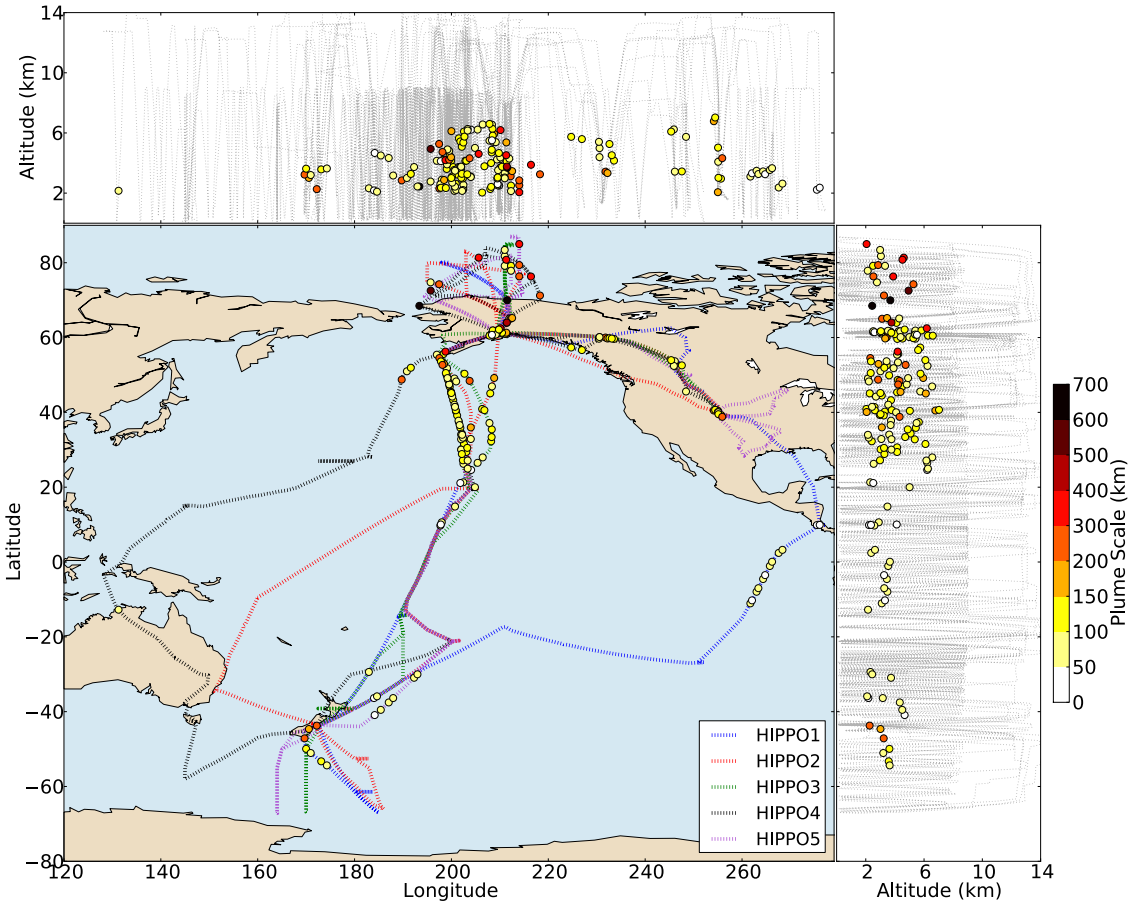

Figure 3.6: As Figure 3.3, except for HAM Base.

ison between the different simulated plume scales. The composite plot highlights the overestimation in plume scale by all of the models, particularly UKCA OldScav, which shows the widest composite of all models. There is also a small decrease in composite plume scale between HAM Low and HAM Base; however, the composites of the rest of the models (HAM Base, HAM High and UKCA NewScav) significantly overlap indicating very little difference in plume scale between these models, in accordance with the plume statistics presented above.

The above analysis has shown that GCMs running at climate modelling simulations are unable to capture the scales of plume structures detected during the HIPPO campaign. The analysis can be taken a step further to compare the overall scales of variability of the simulated flight track data to the along-flight-track measurements using one-dimensional autocorrelation analysis as was done in Chapter 2, Section 2.2.6.

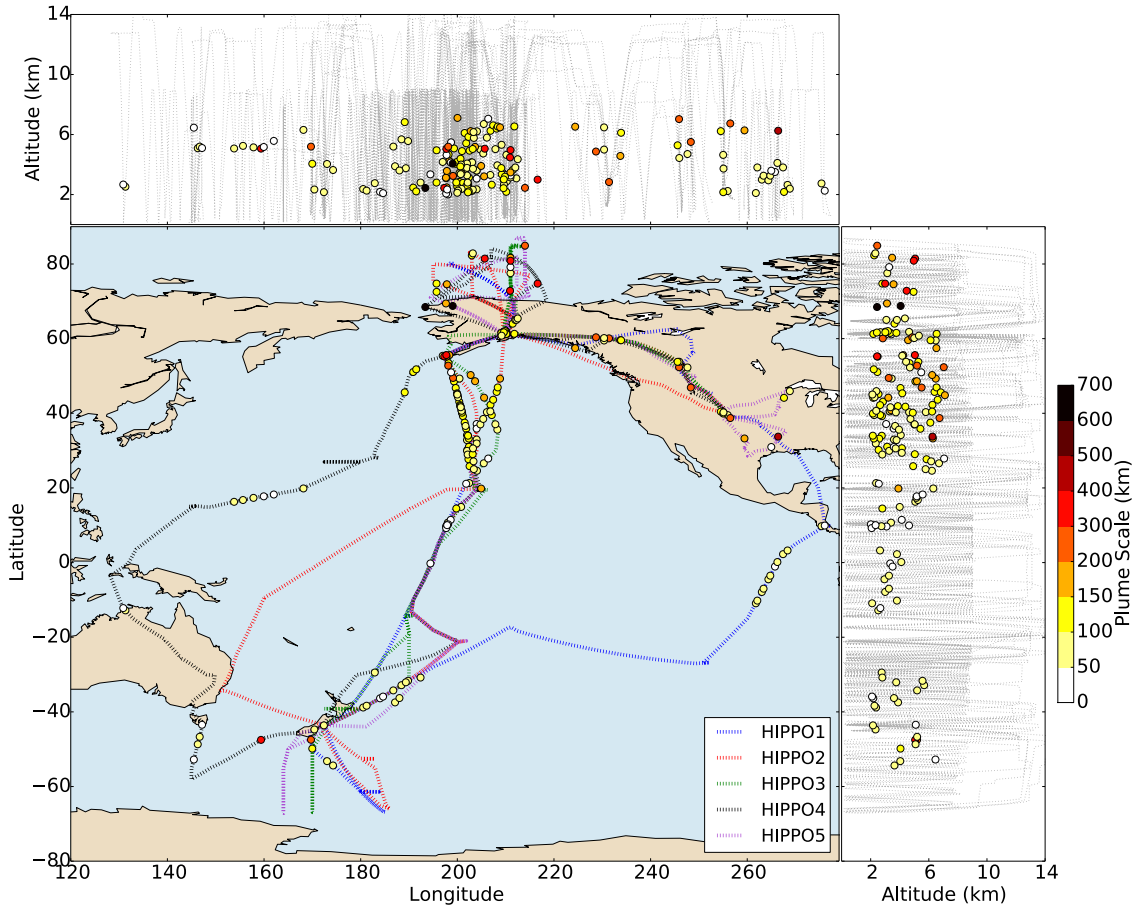

Figure 3.7: As Figure 3.3, except for HAM High.

Figure 3.9 shows the average daily autocorrelation of all five HIPPO flight tracks for observations (in blue) and the five model simulations. The HIPPO data reach a near-zero autocorrelation at lags close to 100 km, meaning that most of the variability in the HIPPO observations occurs on scales of less than 100 km (as discussed in the previous chapter). All of the model flight track data, however, reach a near-zero autocorrelation between lags of 200 - 300 km, meaning the variability in simulated flight-track data occurs on scales two to three times the value of observations. The autocorrelation function of the model data also remains relatively constant at scales less than 10 km compared to that of HIPPO, indicating much lower variability in models at these small scales. At all scales below 200 km the autocorrelation functions of the model simulations remain higher than the HIPPO observations, confirming that there is greater variability in the observations at these scales. There is relatively little difference be-

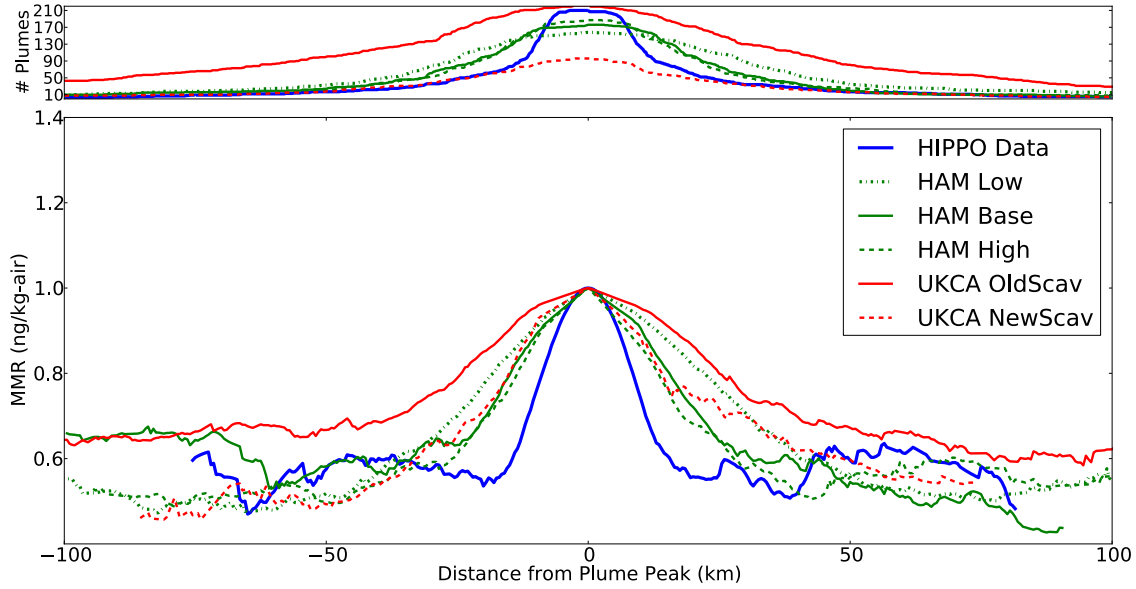

Figure 3.8: Normalised plume composites of all BC plumes detected during the HIPPO campaign (blue) and all GCM simulations. The top panel shows the number of plumes included in each composite bin; only bins with at least 25 plumes are depicted in the composite.

tween the different models, except for UKCA NewScav, whose autocorrelation drops off more rapidly than the other models after at approximately 10 km. Again, this is consistent with the plume scale analysis presented earlier.

A peculiar feature of the models' autocorrelation is the peak at approximately 450 km. The peak is persistent in all five flight missions and all five simulations and indicates the presence of synoptic-scale periodicity. *Anderson et al.* [2003] found a similar peak in their autocorrelation analysis of aerosol variability using satellite data and attributed it to the fact that the satellite passed over three distinct, synoptic-scale aerosol plumes with relatively clean air in between. The peak in the above autocorrelation could be a result of the flight track sampling smaller segments of larger-scale plumes. This possibility will be explored by analysing four-dimensional model output from ECHAM-HAM in the following sections.

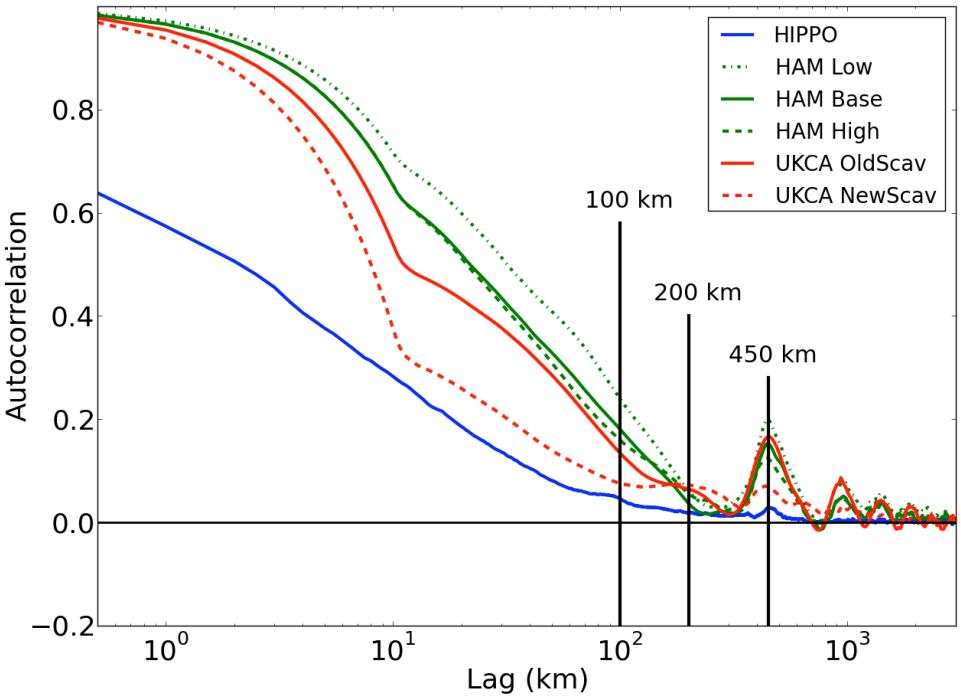

Figure 3.9: Daily spatial autocorrelation averaged over all five flight campaigns for the HIPPO observations (blue), the ECHAM-HAM simulations (green), and HadGEM-UKCA simulations (red). The autocorrelation is a function of lag in kilometres.

3.4.2 2D Autocorrelation analysis

Autocorrelation analysis has been shown to provide useful insight into the scales of variability of aerosols in the atmosphere. In the above analysis of HIPPO observational data and the along flight-track model output, the autocorrelation as a function of lag distance-along-the-flight-track shows that the variability in observed BC fields exists on scales smaller than the simulated BC fields. Additionally, there is very little difference in the scales of variability between the simulated BC data at different resolutions, which is counter-intuitive given that one would expect BC variability to increase as the model resolution increases. One possible explanation for the unchanging autocorrelation between model runs is that the HIPPO flight track is limited in spatial coverage and is perhaps unable to sample large enough segments of the model data in order to capture the model's larger-scale variability. This possibility is explored using two-dimensional autocorrelation analysis over two regions of model data: remote Pacific

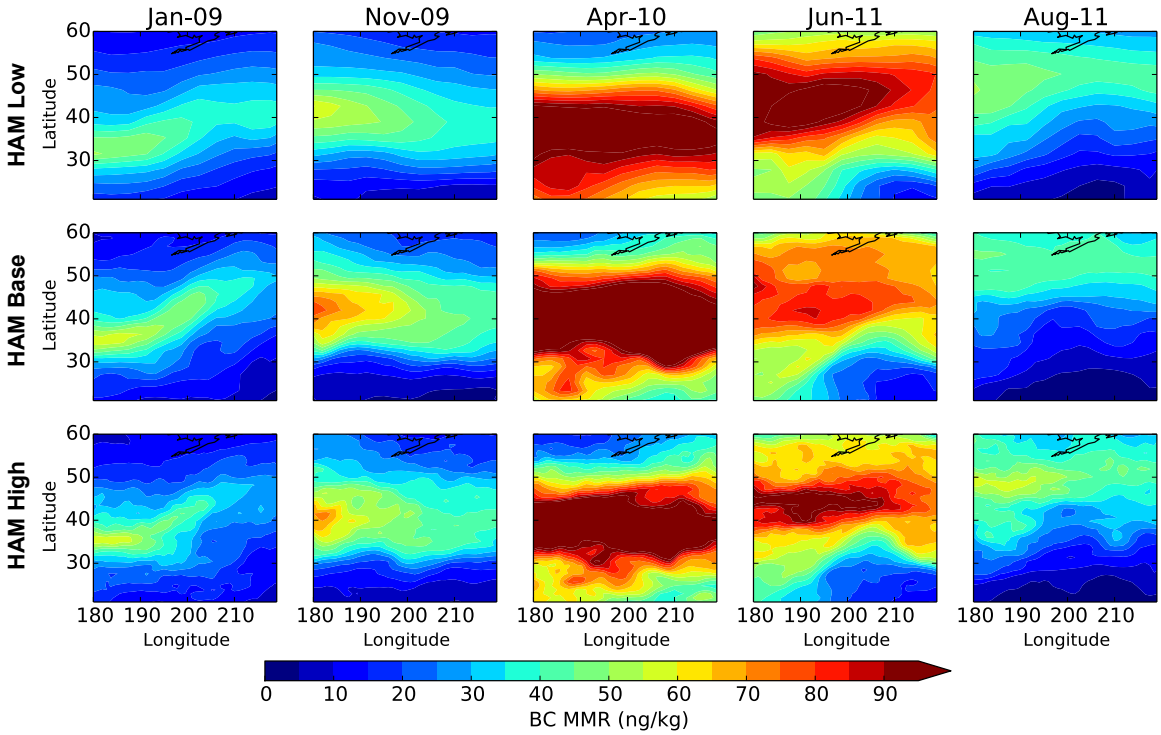

Figure 3.10: Simulated monthly mean mid-tropospheric black carbon mass mixing ratio (ng/kg-air) over the North Pacific Ocean at an altitude of 5.3 km for the five HIPPO months: January 2009, November 2009, April 2010, June 2011 and August 2011. Top row shows BC fields from HAM Low, middle row from HAM Base and bottom row from HAM High.

and near-source.

For consistency with the HIPPO observations, the first analysis region consists of a 40° longitudinal by 40° latitudinal box over the north Pacific Ocean from (20°N, 180°E) to (60°N, 220°E). The two-dimensional autocorrelation analysis was calculated for 6 hourly BC fields and averaged over a month at a given model level, which corresponds to an altitude of approximately 5.3 km in all three ECHAM-HAM simulations. This altitude was chosen as a large number of FTS plumes were detected in the mid-troposphere. Five monthly mean autocorrelation fields are presented to match with the five HIPPO missions: January 2009, November 2009, April 2010, June 2011, and August 2011. Figure 3.10 shows the black carbon monthly mean mass mixing ratio for this region during each of the HIPPO months. The BC fields reveal large inter-seasonal variability with high concentrations of BC during April and June when significant amounts of East Asian air are transported across the Pacific Ocean. One can also see

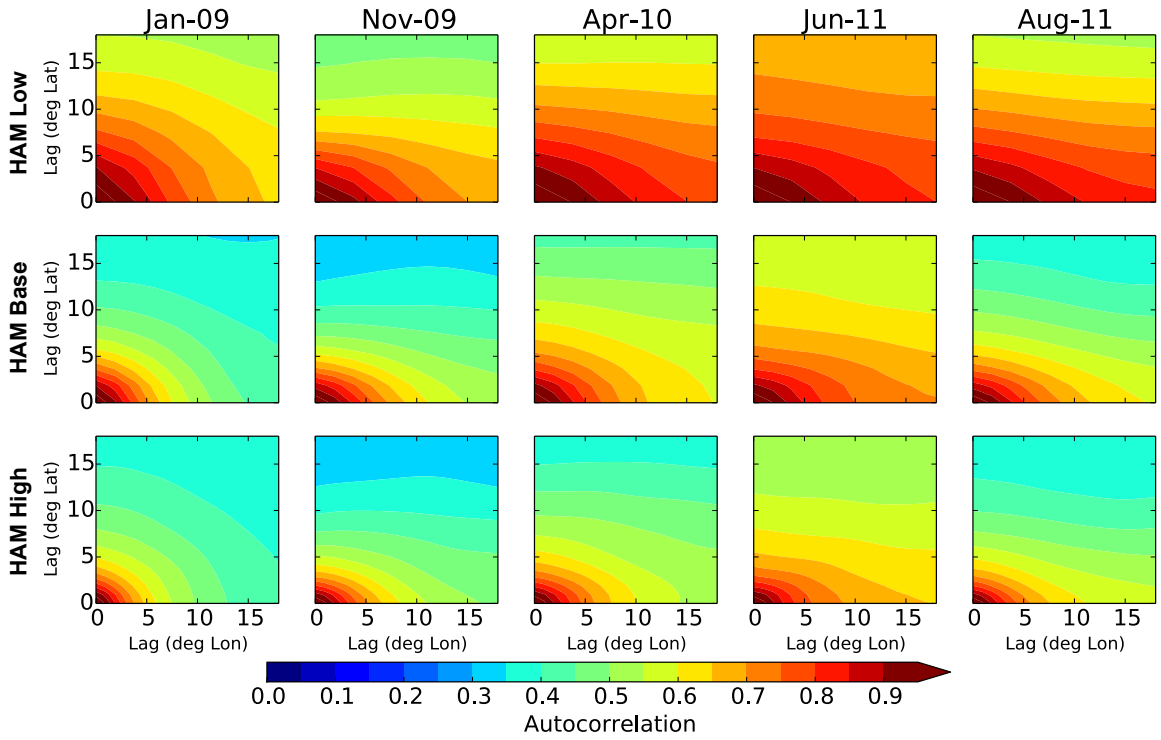

Figure 3.11: Two-dimensional autocorrelation of BC mass mixing ratio over the North Pacific Ocean at an altitude of 5.3 km for the five HIPPO months. X-axis shows the autocorrelation as a function of longitude (in degrees); y-axis shows the same for latitude. The autocorrelation was calculated at 6 hourly intervals and then averaged over each month.

more structure within the BC fields as the model resolution increases; however, a large degree of this structure has been smoothed out by taking the monthly mean. Keep in mind that the 2D autocorrelation analysis was performed on 6 hourly model data and subsequently averaged over the month, so the BC fields were not as smooth as depicted by the monthly mean fields.

Figure 3.11 shows the two-dimensional monthly averaged autocorrelation as a function of degree longitude (in the x-direction) and degree latitude (in the y-direction). There are a number of interesting observations to note from this figure. Firstly, the two-dimensional autocorrelation decays more rapidly as the model resolution is increased. Using a lag of 3.75° as a reference point, in the latitudinal direction the autocorrelation drops by an average of 0.14 and 0.08 when the resolution increases to HAM Base and then to HAM High, respectively. The values are slightly smaller in the longitudinal direction with average drops in autocorrelation of 0.09 and 0.07.

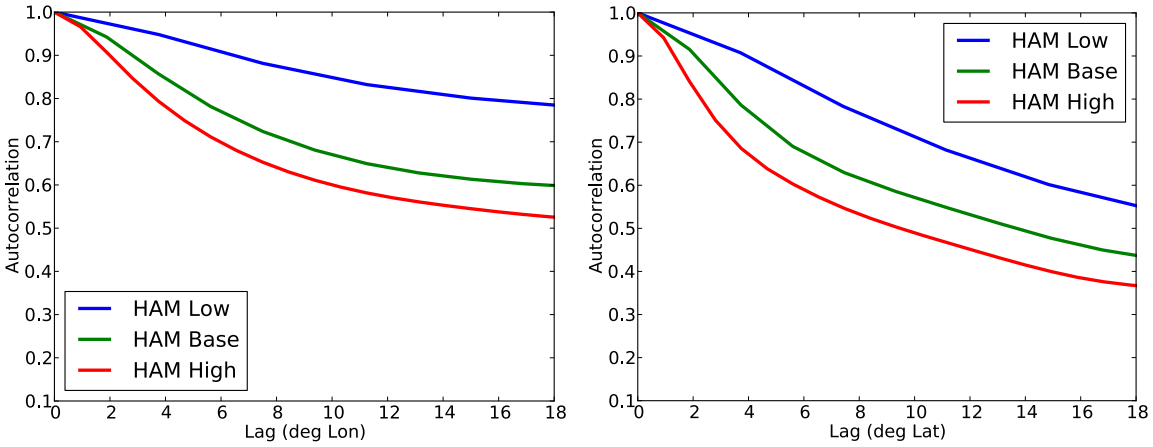

(a) (b)

Figure 3.12: Separates the 2D autocorrelation of April 2011 from Figure 3.11 into each dimension for visualisation purposes. (a) is a cross section of the autocorrelation as a function of lag in degree longitude when the lag in latitude is 0 degrees, and (b) is a cross section of the autocorrelation as a function of lag in degree latitude when longitudinal lag is 0 degrees.

This indicates that BC variability increases with increasing resolution, contrary to the results from the 1D autocorrelation of the along-flight-track model data, which showed similar autocorrelation values at different resolutions. This also shows that the autocorrelation remains higher in the longitudinal direction than in the latitudinal direction, meaning that BC exhibits less variability longitudinally. To demonstrate these observations more clearly, Figure 3.12 gives an example of the 2D autocorrelation from April 2011, separated into its 1D autocorrelation in each dimension when the other dimension is held fixed at zero degree lag. This clearly shows that: 1) as resolution increases, so does the rate of decay of the autocorrelation function, 2) and the longitudinal autocorrelation decays slower than the latitudinal autocorrelation. The latitudinal autocorrelation also shows a more uniform increase in variability with increasing resolution, whereas the longitudinal autocorrelation shows greater gains in variability when increasing the resolution form HAM Low to HAM Base.

These trends can also be visualised in the BC fields from the previous figure (Figure 3.10), where large-scale BC structures spread across the North Pacific region in the longitudinal direction as BC is being transported away from its East-Asian source

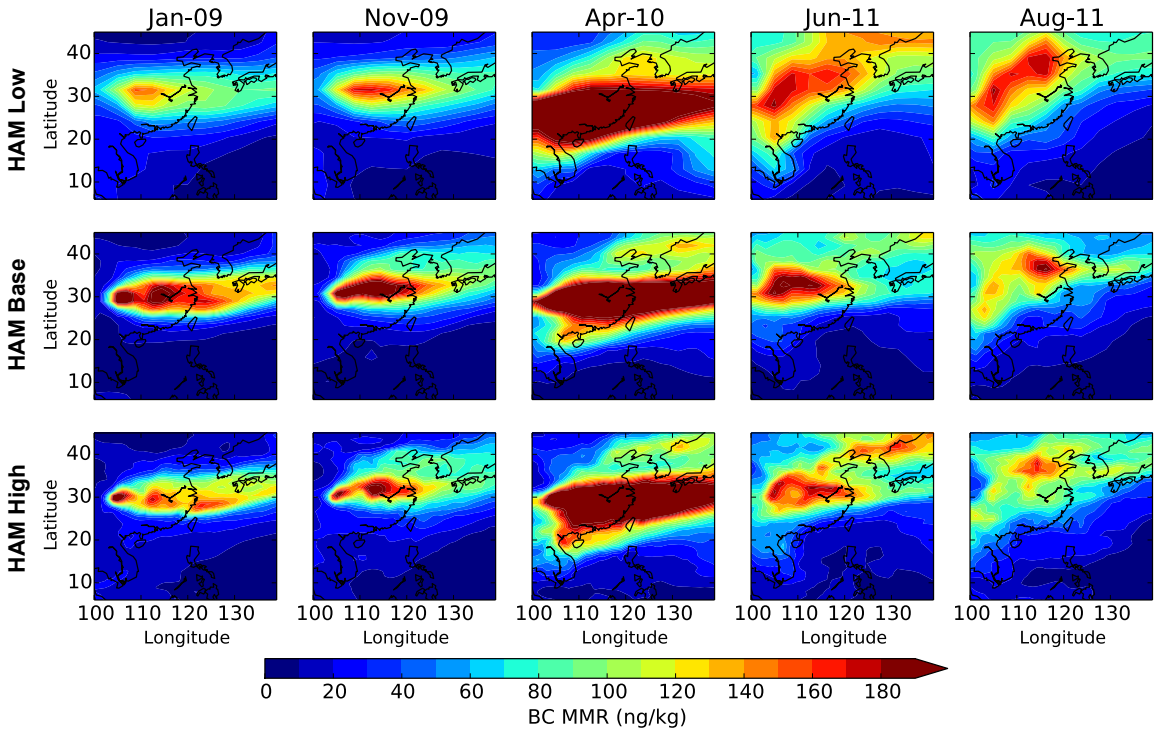

Figure 3.13: Monthly mean mid-tropospheric black carbon mass mixing ratio (ng/kg-air) over BC source region in East Asia for the five HIPPO months: January 2009, November 2009, April 2010, June 2011 and August 2011. Top row shows BC fields from HAM Low, middle row from HAM Base and bottom row from HAM High.

region. Furthermore, the variability in BC is much lower in the summer and springtime months (as indicated by the higher autocorrelation values) when large amounts of BC are being transported across the Pacific Ocean in large-scale plumes.

This analysis is extended by comparing BC variability in the remote regions of the HIPPO campaign to BC variability near sources. To investigate near-source BC variability, the two-dimensional autocorrelation analysis was performed on another 40° longitudinal by 40° latitudinal region, this time over East Asia from (5°N, 100°E) to (45°N, 140°E). The same five months of BC data were analysed; the monthly mean BC mass mixing ratios at the same model levels (5.3 km) are shown in Figure 3.13. Qualitatively, one can see that BC plumes have greater structure in the near source region compared to the north Pacific Ocean where the plumes have had time to disperse more evenly throughout the mid-troposphere. Concentrations are also highest in April 2010 when emissions of BC are at a maximum [*Bond et al.*, 2013].

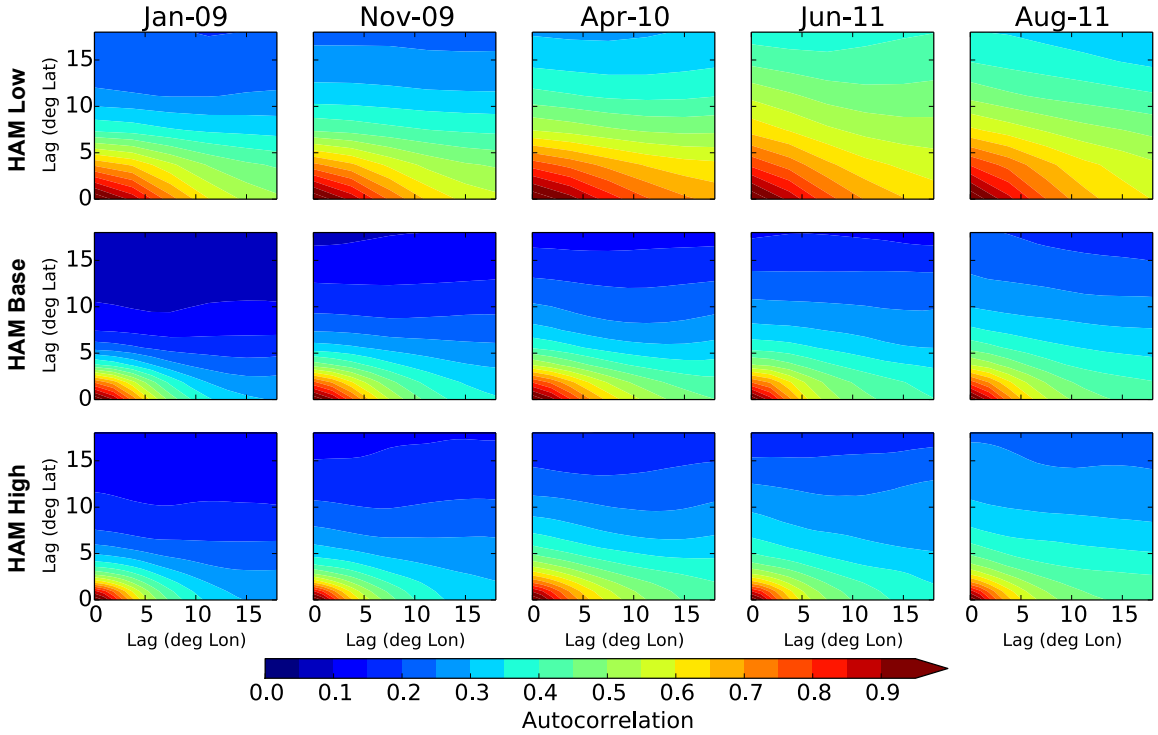

Figure 3.14: Two-dimensional autocorrelation of BC mass mixing ratio at an altitude of 5.3 km over the East-Asian source region for the five HIPPO months. X-axis shows the autocorrelation as a function of longitude (in degrees); y-axis shows the same for latitude. The autocorrelation was performed at 6 hourly intervals and then averaged over each month.

The two-dimensional autocorrelation functions are presented in Figure 3.14. Overall, this figure shows that the autocorrelation decays faster in the near source region compared to the remote Pacific, indicating a higher degree of BC variability near sources. At a lag of 3.75°, the autocorrelation of HAM Base near source is 0.18 to 0.34 less in the latitudinal direction and 0.05 to 0.17 less in the longitudinal direction compared to the remote Pacific. The differences become even larger at higher lag values. Although the variability is greater in both directions near source, the variability still tends to be greater in the latitudinal direction than in the longitude, as seen in the remote Pacific region.

Again in all cases, the autocorrelation decreases with increasing resolution, and the decrease is larger between HAM Low and HAM Base than between HAM Base and HAM High, particularly in the longitudinal direction. These differences are difficult to

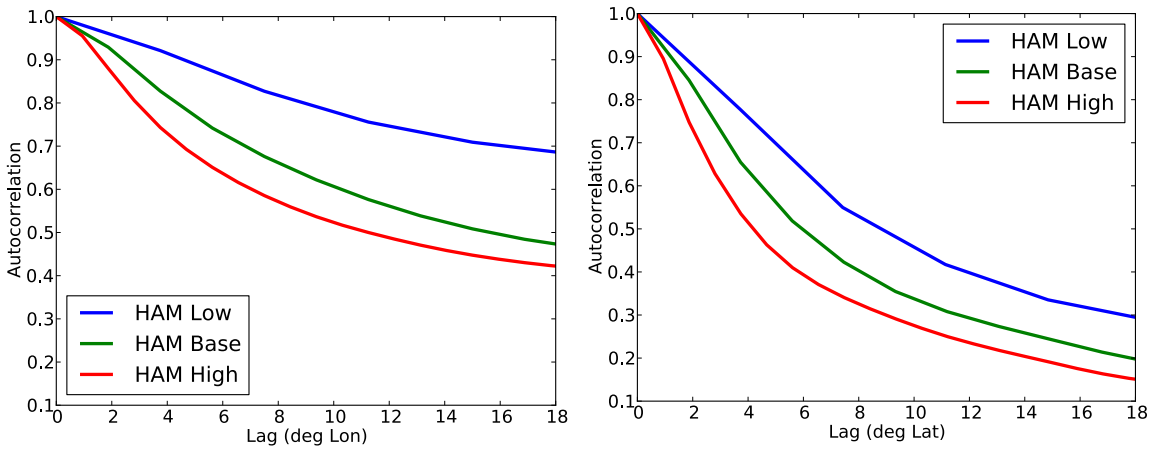

(a) (b)

Figure 3.15: Separates the 2D autocorrelation of April 2011 from Figure 3.14 into each dimension for visualisation purposes. (a) is a cross section of the autocorrelation as a function of lag in degree longitude when the lag in latitude is 0 degrees, and (b) is a cross section of the autocorrelation as a function of lag in degree latitude when longitudinal lag is 0 degrees.

see in the two-dimensional plots because the autocorrelation decays so rapidly near-source. Figure 3.15 provides an easier visualisation of the decreases in autocorrelation with increasing resolution as well as the difference in latitudinal and longitudinal variability.

Two-dimensional autocorrelation analysis can also be applied to the model's vertical dimension. To investigate the degree of BC variability in the vertical dimension, the two-dimensional autocorrelation function is applied to the north Pacific region on an area spanning 40° latitude from (20°N, 200°E) to (60°N, 200°E) and approximately 17 km in the vertical. This is essentially a slice down the middle of the first analysis region. The mass mixing ratios for this region are included in Figure 3.16, which shows seasonal differences in the vertical profile of BC with maximum concentrations in the lower to mid-troposphere, particularly in the springtime and early summer months.

In the vertical dimension, the differences in the autocorrelation between the different model resolutions are not as stark as they were in the latitudinal and longitudinal directions. At a lag of 4 km, the autocorrelation of HAM Low is 0.06 – 0.12 lower than HAM Base, and there is very little difference between HAM Base and HAM

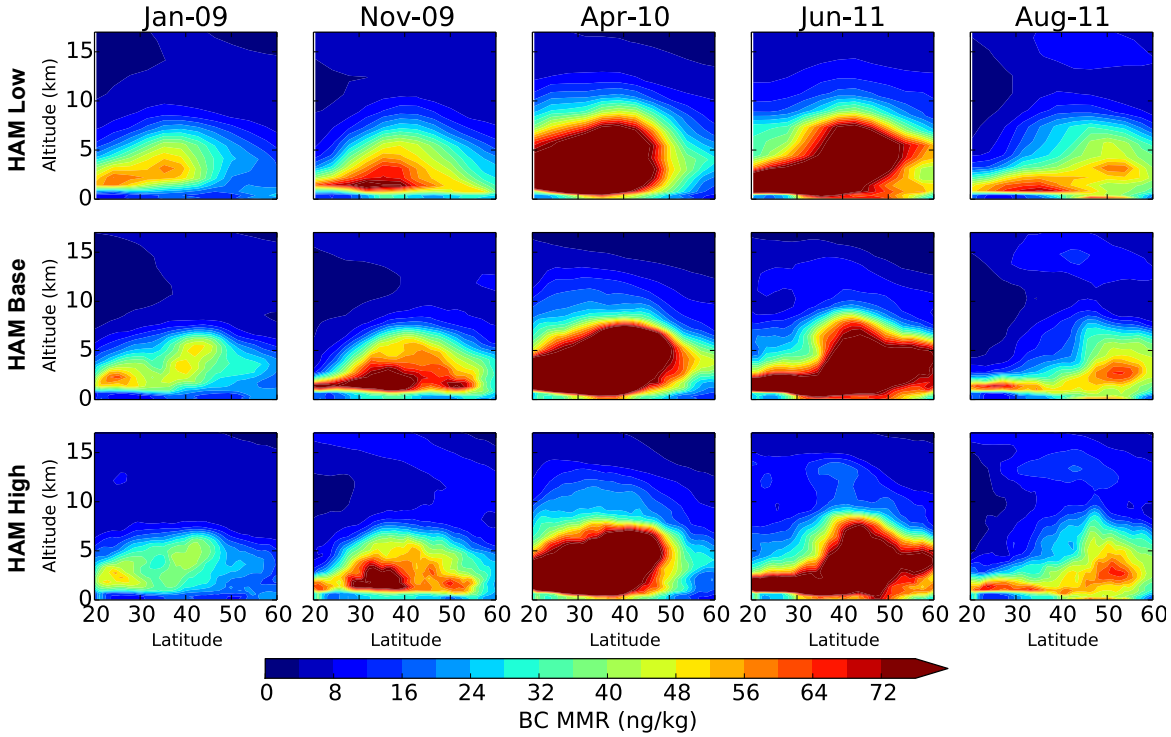

Figure 3.16: Vertical profile (in km) of monthly mean black carbon mass mixing ratio (ng/kg-air) as a function of latitude over the North Pacific Ocean for the five HIPPO months. Top row shows BC fields from HAM Low, middle row from HAM Base, and bottom row from HAM High.

High. HAM Low has roughly half the number of vertical layers compared to HAM Base and HAM High, which both have approximately the same number of layers in the troposphere. Therefore, it is not surprising that there is not a significant change in the autocorrelation functions between HAM Base and HAM High as the tropospheric vertical resolution is nearly identical for these two simulations. There is also very little seasonal dependence in vertical BC variability; the autocorrelation at a lag of 4 km ranges from 0.37 in January 2009 to 0.50 in August 2011.

3.4.3 Three dimensional plume identification

Section 3.4.1 provided an analysis of simulated black carbon plume scales along the flight track of the HIPPO aircraft campaign. While the point-by-point model output enables the direct comparison between observed and simulated plume scales, it does

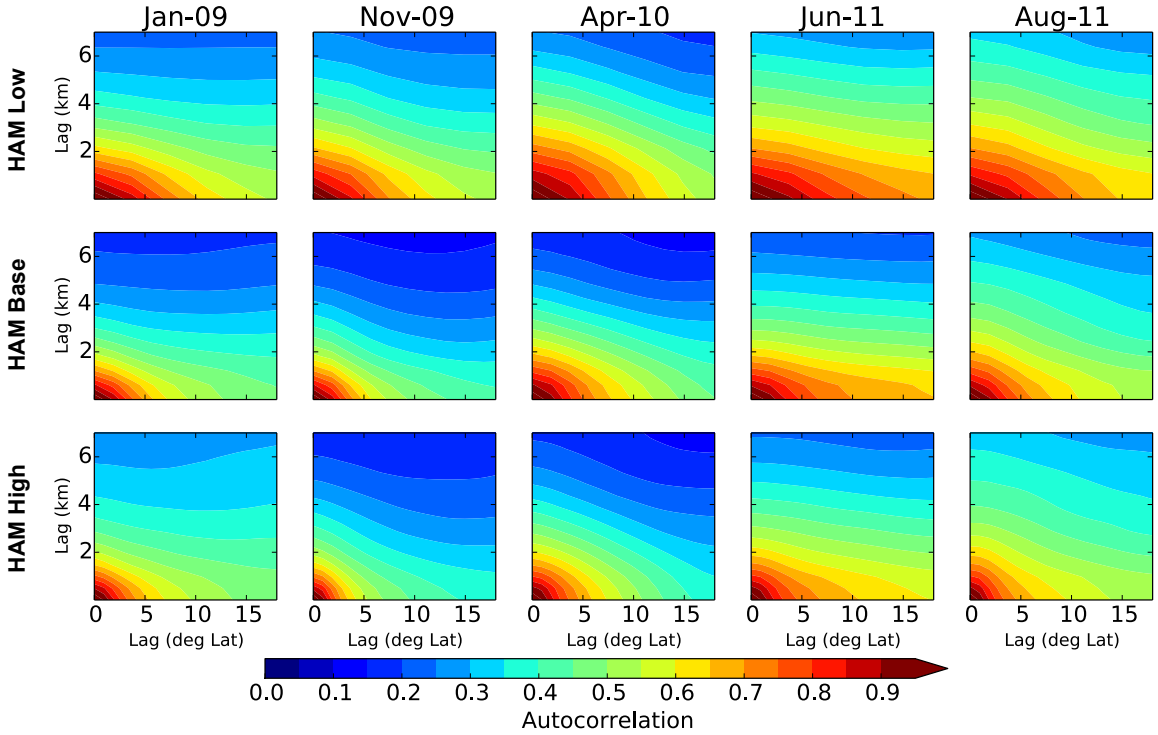

Figure 3.17: Two-dimensional autocorrelation of BC mid-tropospheric mass mixing ratio over the North Pacific Ocean for the five HIPPO months. X-axis shows the autocorrelation as a function of latitude (in degrees); y-axis shows the autocorrelation as a function of altitude (in km). The autocorrelation was performed at 6 hourly intervals and then averaged over each month.

not take into account the potential multidimensional nature of these black carbon plumes. To investigate the multidimensional plume scales simulated by GCMs, a three-dimensional plume detector was developed, which identifies three-dimensional plume structures in space at a particular point in time and quantifies their average latitudinal, longitudinal, and vertical expanses. Section 3.3.3 describes how the 3D plume detection algorithm works.

The 3D plume analysis was conducted over the entire globe but only at time steps that coincided with FTS plumes. Model levels below 2 km were excluded from the 3D plume analysis to remain consistent with the detection of FTS plumes. Each FTS plume was co-located in time and space to the 3D plume in which it is contained. Only 3D plumes that were co-located to an FTS plume are included in the analysis. A limitation of this analysis, is that only three-dimensional plumes are considered, rather

Table 3.3: Plume statistics from 3D plume detection. '# matched plumes' refers to the number of FTS plumes that were successfully co-located with detected 3D plumes. '# of 3D plumes' refers to the number of distinct 3D plumes that contain FTS plumes. The mean scales represent the average spatial scales in each dimension of these 3D plumes.

	HAM Low	HAM Base	HAM High
# matched plumes	146	153	165
# 3D plumes	39	39	46
Mean lat scale (km)	1580	750	500
Mean lon scale (km)	1920	970	680
Mean vertical scale (km)	3.7	2.2	2.0

than 4D plumes whose structures overlap in time. This means that if one plume persisted over several days and was sampled by two different flights, the algorithm would count it as two separate plumes. This likely has a small effect on the results since a 6-hourly model time period spans thousands of kilometres of HIPPO flight track, so it's unlikely to be sampling the same plume in two subsequent flights.

Table 3.3 summarises the results from this analysis. The number of matched plumes refers to the number of FTS plumes in each ECHAM-HAM simulation that were successfully co-located with detected 3D plumes. For HAM Low, 146 of the 158 FTS plumes were matched with 3D plumes; for HAM Base, 153 of 176 FTS plumes were matched; and for HAM High, 165 of the 187 FTS plumes were matched with 3D plumes. The small number of unmatched FTS plumes arises from the fact that the 3D plume analysis was conducted on BC fields at 6-hourly time intervals, and this time resolution could miss some of the shorter-lived plumes that were detected using the flight track simulator, whose output was interpolated to the nearest model time step (on the order of minutes rather than hours).

In the HAM Low simulation, the 146 matched FTS plumes were co-located with 39 distinct 3D plumes. Similarly, the FTS plumes in HAM Base were co-located with 39 distinct 3D plumes, and in HAM High they were matched with 46 distinct 3D plumes. These results indicate that the simulated flight tracks sampled the same large-scale plumes multiple times.

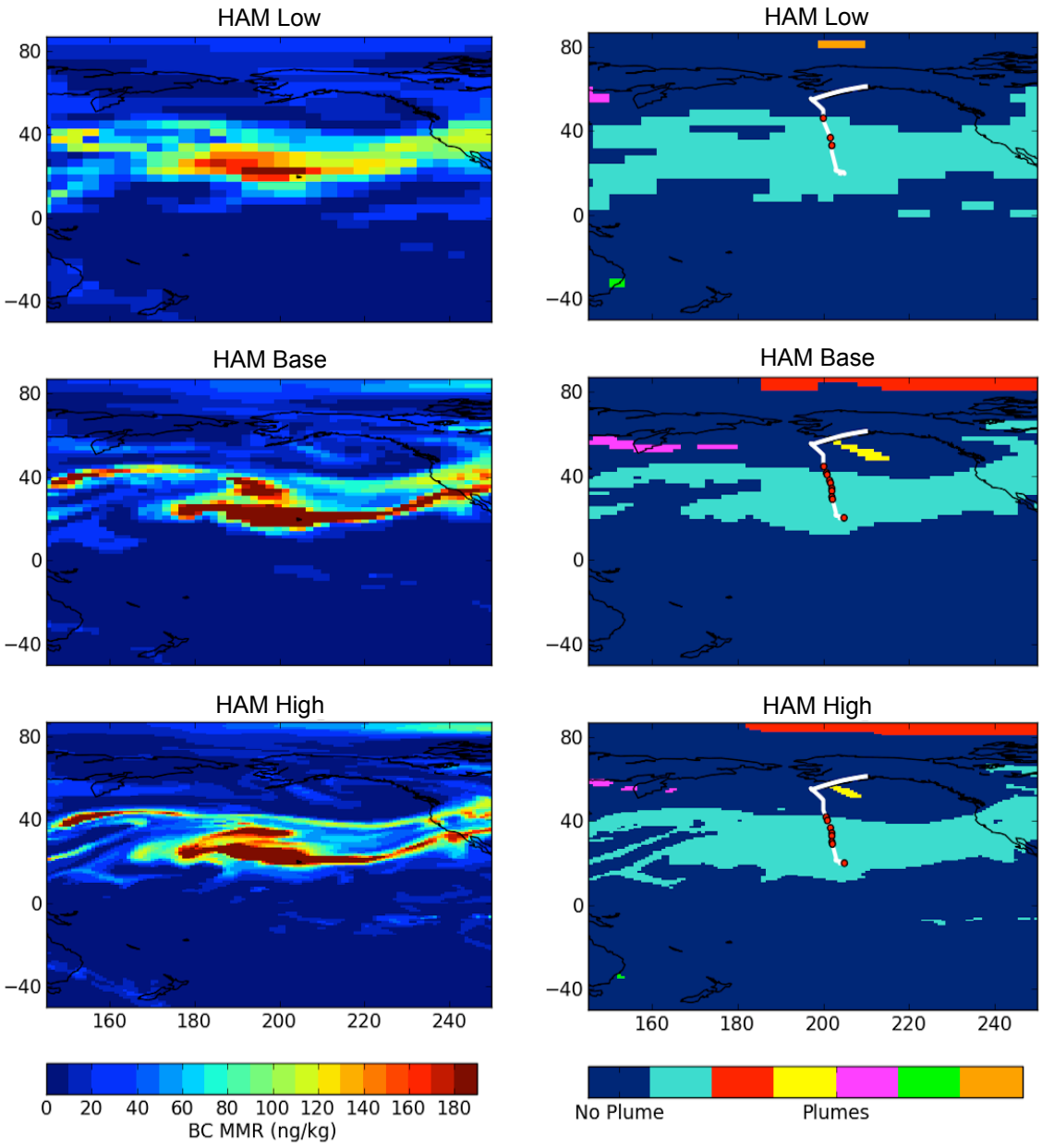

Figure 3.18: Shows an example of the difference in plume scales between the ECHAM-HAM simulations at different resolutions. Panel (a) shows the black carbon mass mixing ratio (ng/kg-air) at an altitude of 4.2 km where several 3D plumes were detected. The fields were simulated at 18:00 on 29 March, 2010, which matches with plumes detected during the third flight of HIPPO3. Panel (b) shows the identified plumes; the light blue represents the matched plumes, the other colours represent other detected plumes, and the dark blue represents where no plume was detected. The white line shows the flight track from HIPPO3, and the red dots represent the FTS plumes detected in each ECHAM-HAM run.

Figure 3.18 shows an example of a three-dimensional plume matched with multiple FTS plumes from a single flight. Note that the plots have been zoomed in over the Pacific ocean; therefore, the longitudinal and latitudinal plume scales extend further than shown in this figure. The displayed fields were simulated on 29 March, 2010 at an altitude of approximately 4.2 km and match with FTS plumes detected during the third flight of HIPPO3. Panel (a) shows the BC mass mixing ratio at each model resolution, and Panel (b) shows the corresponding 3D plumes where dark blue represents no plume and the other colours represent different 3D plumes. The HIPPO3 flight track is displayed in white with the identified FTS plumes overlaid as red points. This shows that the FTS plumes are located within the light blue large-scale 3D plume and that the individual FTS plumes are sampling this large-scale plume multiple times.

With the identification of 3D plumes, their scale in each dimension can be quantified to investigate how these scales change with increasing model resolution. The average scale of each dimension is determined separately. Thus, the longitudinal scale of a single plume is determined by taking the average of the longitudinal plume lengths at every altitude and latitude point. If there are gaps in the plume structures, the length of each segment on either side of the gap is determined separately so that the average length takes into account the smaller-scale filamentary structures within a large-scale plume, similar to those seen in the light-blue plume of the HAM High simulation near 20°N, 160°E. Figure 3.19 describes this process conceptually. The pictured plane is a latitude-longitude plane at a particular altitude. The longitudinal lengths along latitudes (a) and (b) are 4 and 3, respectively. Latitudes (c) and (d) contain gaps, therefore latitude (c) has two lengths of 2 and 1, and latitude (d) has two lengths of 1 and 1. So, in this plane, the average longitudinal length scale is (4+3+2+1+1+1)/6 = 2.

Referring back to Table 3.3, the horizontal scales in both latitudinal and longitudinal directions of the 3D plumes are much larger than those detected along the flight track, with longitudinal scales of 1920 km, 970 km, and 680 km and latitudinal scales

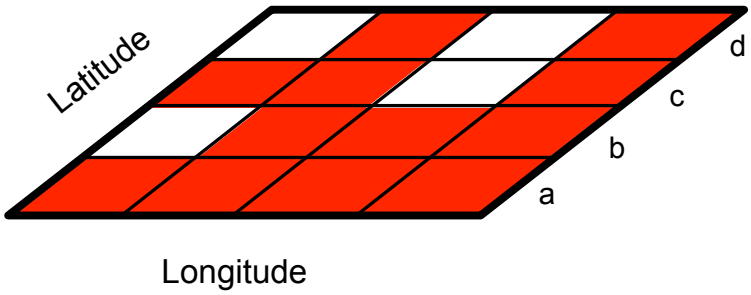

Figure 3.19: Conceptualisation of plume length calculation. The pictured plane is a latitude-longitude plane at a particular altitude. The longitudinal lengths along latitudes (a) and (b) are 4 and 3, respectively. Latitudes (c) and (d) contain gaps, therefore latitude (c) has two lengths of 2 and 1, and latitude (d) has two lengths of 1 and 1. So, in this plane, the average longitudinal length scale is (4+3+2+1+1+1)/6 = 2.

of 1580 km, 750, and 500 km for HAM Low, HAM Base, and HAM High, respectively. These mean scales reveal that the plume scale in both directions decreases significantly with increasing model resolution. The average latitudinal and longitudinal lengths decrease by approximately 50% between HAM Low and HAM Base, and by 30% between HAM Base and HAM High. The 3D plume scales therefore demonstrate the same pattern as both the along-flight-track plume scales and 2D autocorrelation analysis, which showed a smaller increase in variability when increasing resolution from HAM Base to HAM High than when increasing resolution from HAM Low to HAM Base. In this analysis, the horizontal resolutions doubles between each resolution; however, the horizontal plume scales do not show this same trend.

Analysis of the horizontal 3D plume scales also finds that longitudinal length scales are greater than latitudinal length scales by 22 – 36%. This observation again agrees with the results from the two-dimensional autocorrelation analysis, which showed that black carbon exhibited higher variability in the latitudinal direction than the longitudinal direction.

The mean vertical scale of these three-dimensional plume structures is also presented in Table 3.3. The plumes identified in HAM Low show the largest vertical scale of 3.7 km. When the resolution is increased to HAM Base, the mean vertical scale drops to 2.2 km; however, the vertical scale drops only slightly to 2.0 km when

the resolution is increased again to HAM High. This is not surprising given that it is the horizontal resolution that doubles in these simulations, not the vertical. As noted earlier, HAM Low has approximately half the number of vertical levels in the mid-troposphere than both HAM Base and HAM High, which both have a similar number of mid-tropospheric layers. These results therefore show that increasing the vertical resolution results in thinner black carbon plume layers, whereas increasing the horizontal resolution while maintaining a constant vertical resolution has little effect on a plume's vertical scale. This is similar to the results from the 2D autocorrelation analysis that showed increased BC variability in the vertical dimension in HAM Base compared to HAM Low, but not compared to HAM High.

3.5 Summary and Discussion

The aim of this chapter was to understand how a global climate model's inability to resolve sub-grid scale variability affects simulations of important aerosol features. This problem was addressed by comparing observed black carbon plume scales to those simulated by GCMs and testing how model resolution affects these scales. This chapter additionally investigated how model resolution affects black carbon variability in remote and near-source regions. These issues were examined using three different approaches: along-flight-track plume analysis, two-dimensional autocorrelation analysis, and 3D plume analysis.

In the along-flight-track analysis, black carbon plumes measured by the HIPPO aircraft campaign (see Chapter 2) were compared to GCM model output interpolated to the HIPPO flight track. Two global models were used: ECHAM-HAM at three different resolutions and HadGEM-UKCA in two configurations differing only in their description of convective scavenging. Results from the along-flight-track plume analysis showed that GCMs running at resolutions currently suitable for climate simulations are unable to capture the scales of observed along-flight-track plumes. The median observed plume scale from the HIPPO campaign was 56 km, whereas most of the

GCM median plume scales ranged from 130 km for HAM Low to 92 km for HAM High. UKCA OldScav simulated much larger plumes than the rest of the models with a median scale of 217 km.

Increasing model resolution resulted in a small improvement in the representation of flight-track plume scale; however, the change in median plume scale was greater between HAM Low and HAM Base (130 km to 101 km) than between HAM Base and HAM High (101 km to 92 km). Autocorrelation analysis of the along-flight-track data also revealed that variability in observations exists on scales less than 100 km, whereas variability in all five simulated flight track data exists on much larger scales between 200 – 300 km.

Improving the description of convective wet scavenging was shown to decrease the median plume scale by more than half (from 217 km to 95 km). This change in plume scale is much greater than the changes due to model resolution; however, the improvement does not produce better results than the highest resolution HAM simulation. Additionally, the autocorrelation function of UKCA NewScav was lower than the other model simulations (though still higher than the observations) between scales of 10 km to 100 km, indicating greater variability at these scales. This demonstrates how important aerosol processes can have a significant effect on BC plume scales and overall BC variability.

To investigate further the effect of model resolution on BC variability, two-dimensional autocorrelation analysis was performed on two 40°x40° regions — one over the remote Pacific where many of the HIPPO flights occurred and another over East Asia, a high source region of black carbon. The 2D autocorrelation functions revealed that BC variability was much higher near source regions than in the remote Pacific. This agrees with previous work that found that AOD measured by aircraft in the Arctic showed greater variability in regions dominated by local emissions compared to regions dominated by long-range transport [*Shinozuka and Redemann*, 2011]. The 2D autocorrelation analysis also showed that BC variability increased with resolution;

however, the increase was smaller between HAM Base and HAM High than between HAM Low and HAM Base, particularly in the longitudinal direction. In both regions and all resolutions, BC variability in the longitudinal direction was less than in the latitudinal direction. This implies that models may experience a greater improvement in the representation of BC variability from an increase in latitudinal resolution than in longitudinal resolution, although in practice this may be difficult to implement.

The aim of the 3D plume analysis was to quantify the multidimensional scales of 3D black carbon plumes and compare them to the scales of the flight-track-simulated plumes. The FTS plumes were co-located to 3D plumes at each resolution to investigate the scales of the 3D plumes that were sampled by the flight track. The analysis revealed that in each simulation, the hundreds of FTS plumes (between 146 for HAM Low and 165 for HAM High) were actually samples of a much smaller number (between 39 for HAM Low and 46 for HAM High) of 3D plumes. The scales of the 3D plumes were found to be much larger than the FTS plumes with longitudinal scales of 1920 km, 970 km, and 600 km, for HAM Low, HAM Base, and HAM High, respectively. The latitudinal scales were found to be 22 – 36% smaller than their respective longitudinal scales. The vertical extent of the 3D plumes were significantly smaller than their horizontal extent with scales of 3.7 km, 2.2 km and 2.0 km.

The results from these analyses reveal a number of important insights into model simulations of BC variability. Firstly, they confirm results from Chapter 2 which concluded that plume structures have a significant impact on BC scales of variability in the atmosphere. Qualitatively, the 2D autocorrelation functions were heavily influenced by plume structures present in BC fields. During the HIPPO campaign period, they showed lower variability in Spring and Summer when high BC concentrations were distributed in large-scale plumes. The 2D autocorrelation functions also showed lower variability in the longitudinal direction, particularly in regions where large-scale BC plumes were spread out across the domain by longitudinal air flows. The along-flight-track plume analysis in both observations and simulations confirmed that the

total mass in plumes represents a significant portion of the total BC mass in the free troposphere. Therefore, accurately capturing these plume scales is likely an important step in predicting BC's effect on climate.

Another key observation is that global climate models running at climate simulation resolutions have difficulty capturing the along-flight-track BC variability. This was shown by the overestimation in both the FTS plume scales and the autocorrelation functions of the flight-track-simulated data compared to the measured HIPPO data. There were small improvements in the representation of the plume scales when model resolution was increased; however, the change was greater between HAM Low and HAM Base than between HAM Base and HAM High. Between the Low and Base simulations, both the horizontal resolution and tropospheric vertical resolution were doubled, but between the Base and High simulations, the horizontal resolution doubled and the tropospheric vertical resolution remained nearly the same. The 3D plume analysis also showed that the vertical extent of the large-scale 3D plumes halved from HAM Low to HAM Base, and remained nearly the same between HAM Base and HAM High. This suggests that the simulated along-flight-track plume scales are dominated by their vertical component and that perhaps further improvement in vertical resolution would result in better agreement between simulated and observed plume scales.

While the lack of improvement in plume scales between HAM Base and HAM High is likely due in part to vertical resolution, it may not be the full story. A doubling in the vertical resolution between HAM Low and HAM Base only resulted in a 23% increase in median plume scale. If the models were simply not capturing the vertical component of the HIPPO plumes, than one might expect a greater improvement when the vertical resolution is doubled. Additionally, the 2D autocorrelation and the 3D plume analysis showed the same trend — that differences in variability and horizontal plume scales were larger between HAM Low and HAM Base than HAM Base and HAM High. In these cases, vertical resolution was not a factor. This could mean

that models are in fact converging on the horizontal scales of these plumes and the resolution is sufficiently high to capture the horizontal variability of BC. However, the fact that the along-flight-track plume scales exhibit the same trend could suggest that the models' resolution does not fully account for the discrepancy between observed and simulated plume scales. It is unclear which is the case as the measurements do not provide data on the horizontal extent of the larger scale plumes.

The 3D plume analysis demonstrated that the scales of the FTS plumes were much smaller than the horizontal scales of the 3D plumes at all resolutions, which indicates that the flight track was unable to adequately sample the horizontal extent of these large scale plumes. The FTS plumes were in fact sampling the large-scale 3D plumes multiple times; the smaller scales of these FTS plumes implies they were either sampling the vertical component of the same plume or sampling the internal variability of these large-scale features. The peak at 450 km in the 1D autocorrelation functions of the simulated flight-track data is likely a product of this sampling, given that the horizontal scales of the 3D plumes are roughly a multiple of 450 km. The fact that the peak appears in the model data and not the HIPPO data could be because these large-scale features were not present at the time of the observations or that the aircraft did not sample them.

In conclusion, these results show that GCMs overestimate the along-flight-track variability from observations; however, the scale of the flight-track plumes are not representative of the large-scale features produced in the model. Therefore, it is unclear how much of an impact this has on model predictions of BC's effect on climate. The fact that the horizontal plume scales decreased less between the baseline and high resolution simulation could mean that the key horizontal scales of these plumes are being resolved at the highest resolution. Otherwise, the model may be inadequately describing an important aerosol process, such as wet scavenging, which could impact these horizontal plume scales. A combination of measurements that are able to measure both the aerosol vertical profile and the global-scale horizontal extent of aerosol

plumes may provide insight into these issues.

Chapter 4

Investigation of unresolved scales in aerosol microphysics modelling

The preceding chapters have shown that global aerosol models running at resolutions currently suitable for climate simulations are not able to capture important scales of variability of aerosols in the atmosphere. In these models, the spatial variations of meteorological parameters, primary emission fluxes, and aerosol and trace gas fields are averaged over global model grid boxes so that the distribution and microphysical evolution of aerosols may not be properly represented. This averaging of aerosol fields can affect important spatial scale-dependent processes such as cloud formation and precipitation development, which are affected by variability in cloud condensation nuclei; nucleation events and production of secondary aerosols that depend on sub-grid particle concentrations and non-linear reaction rates; emissions and removal, which are instantaneously diluted over a model grid-box; and the interactions of individual aerosol plumes, which cannot be resolved within a model grid-box.

The aim of this chapter is to understand the impact of neglecting sub-grid scale aerosol variability on simulated aerosol fields, specifically analysing the effect it has on aerosol optical depth (AOD), an important measure for determining aerosol-radiation interactions, and cloud condensation nuclei (CCN), an important parameter for aerosol-

cloud interactions. This analysis will also identify aerosol processes that are most affected by neglecting sub-grid scale aerosol variability, so that parameterisations of specific aerosol processes can be targeted in order to improve model predictions of the aerosol effect on climate.

As highlighted in the introductory chapter, there exist previous studies that explore the effect of neglecting sub-grid aerosol variability on aerosol simulations; however, most of them do so by varying model resolution and evaluating the subsequent effect on aerosol fields. In these studies, simulated aerosols are affected by changes in resolution of a multitude of different meteorological, dynamical, and microphysical fields, making it difficult to isolate and understand the impact of a particular aerosol process. Because the focus here is on the importance of aerosol variability, it is crucial to disentangle aerosol variability from other sources of variability within the model. To address this issue, a novel technique is developed to simulate aerosol processes at varying resolutions while maintaining a constant resolution in all other model fields.

While the proposed technique has not yet been applied in the context of aerosol variability, there have been previous attempts to run different model components at varying resolutions. These studies have mostly focused on separating the dynamical core of the model from the physical parameterisations. *Held and Suarez* [1994] proposed and tested a method to evaluate the dynamical cores of atmospheric general circulation models independently from the physical parameterisations. With their method, they replaced the detailed radiation, turbulence, and moist convection physical parameterisations with simple forcing and dissipation so that they could vary the resolution of the dynamical core while effectively keeping the resolution of the physical parameterisations constant. While this technique allowed the modellers to test resolution convergence of the dynamical core, the simplified physical parameterisations did not provide realistic results for understanding the impact of dynamical variability on atmospheric parameters.

Williamson [1999] similarly studied the effect of varying the resolution of the dy-

namical core of a global climate model separately from its physical parameterisations. Their method involved modifying the dynamical state equations of their spectral model so they could be temporarily truncated to a specified lower spectral resolution. After the physical parameterisations were calculated at this lower resolution, the forcing from these parameterisations was expanded back to the untruncated dynamics grid. This method enabled the authors to explore the convergence characteristics of a particular model; however, the method introduced numerical instabilities in simulations longer than five months and required the addition of a linear stress term on the higher resolution simulations that was not present in the lower resolution runs.

A more recent study examined the resolution dependence of cloud microphysics parameterisations by holding the resolution of the dynamics grid constant and changing the grid spacing of the selected parameterisations [*Gustafson et al.*, 2013]. In this setup, their model ran at a specified fine-scale resolution, which communicated at each time step with another copy of the model physics on an alternate, coarse resolution grid. This was done by coarsening the fine-scale dynamics to the alternative grid for additional coarse-grid physics calculations that were not permitted to feed back into the fine dynamics grid. Therefore each simulation produced physics calculations at two different resolutions. However, even though the original dynamics grid was not altered by the coarse-grid physics, the coarse-grid physics could only interact with the coarsened version of the dynamics and vice versa (fine-scale physics with fine-scale dynamics).

The above methods, while useful in their intended applications, required modifications to the original model and, as a result, potentially introduced differences between coarse-grid and fine-grid components arising from factors other than resolution changes. The method presented in this chapter offers an alternative approach to varying the resolution of different model components separately from one another. In this design, the resolution of aerosols and trace gases are varied separately from the resolution of the dynamics and physics (including meteorology) of the model. Two

grids are used, one coarse and one fine; however, in this setup, both the fine-grid and coarse-grid aerosols and gases interact with the fine-grid meteorology and dynamics, so that any differences in the simulations are due solely to changes in aerosol variability. This type of experimental set-up has never been used to investigate the effect of neglecting sub-grid aerosol variability on important climate metrics, such as AOD and CCN. The implementation of this technique is described in more detail in the following section.

4.1 Methods

4.1.1 Experimental Design

In order to understand how sub-grid aerosol variability affects model predictions of aerosol fields, this experiment modifies the chemistry version of the Weather and Research Forecast model (WRF-Chem) [*Grell et al.*, 2005] so that it is capable of simulating aerosol microphysical processes at a different resolution than the dynamical and meteorological processes. The purpose of this technique is to recreate the artificial dilution and mixing of aerosol properties that occurs in global climate models, while maintaining a constant resolution in the other fields within the model. This is accomplished by running the model at a specified high resolution and, as the model is running, averaging the high resolution aerosol and trace gas fields over a pre-defined, lower resolution grid, thereby effectively dispersing the aerosol and gaseous fields over a larger grid box.

Figure 4.1 describes the process conceptually. The grid in Figure 4.1a represents the high resolution aerosol and gas fields. To simulate these fields at a lower resolution than the rest of the model, we take the mean value of all of the high resolution grid cells residing within the corresponding low resolution grid cell and re-assign each of the high resolution cells to the mean value, as depicted in Figure 4.1b. This means that even though the aerosol and trace gas species are actually running on the high resolution

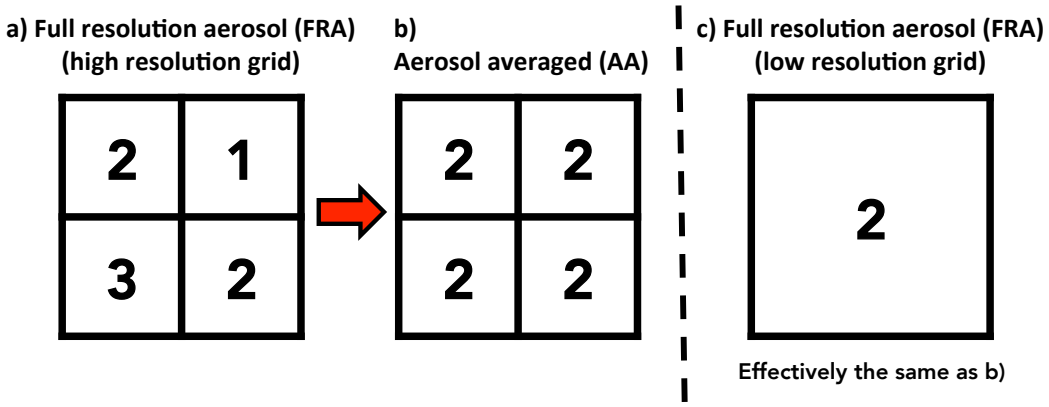

Figure 4.1: Conceptual description of experimental design. The first panel represents the high resolution aerosol and trace gas fields (a). In the second panel, the mean value of these high resolution fields is assigned to each of the high resolution grid points (b), which is effectively the same as a lower resolution grid with the same value (c).

grid, each fine grid cell within the coarse grid cell has the same value. Therefore, from the model's perspective, the fields are equivalent to a low resolution grid similar to Figure 4.1c.

This method was implemented in the regional-scale model, WRF-Chem, whose modular structure allows for easy execution of this experimental design. In WRF-Chem, the aerosol and gas-phase processes occur within the "chemistry driver", which contains separate modules for each aerosol process. In my modified set-up, the aerosol and gaseous fields are averaged over the lower resolution grid before and after each module within the chemistry driver. The averaged fields are then passed onto the rest of the model. This process is repeated at every time step. As a result, the aerosol and gaseous species are effectively simulated at a lower resolution while allowing for interaction with the high resolution meteorology.

With this design, the resolution of the aerosol and gaseous fields can be varied by simply changing the number of high resolution grid points over which the fields are averaged. In this chapter, these types of simulations are referred to as "aerosol averaged" (AA) runs. These aerosol averaged runs can then be compared to simulations in which the aerosols are simulated at the same resolution as the rest of the model.

These simulations are referred to as "full resolution aerosol" (FRA) runs.

Grid Set-up

The study is conducted over a 1,280 km by 1,280 km grid, encompassing nearly all of the United Kingdom and north-western France. To prevent unrealistic interactions between the averaged fields and the boundary conditions, the "aerosol averaging" technique is applied only to the inner 640 km x 640 km grid. Analysis is limited to this region, which covers the southern half of the United Kingdom and the English Channel. The left panel of Figure 4.2 shows the terrain height of the entire outer grid, with the inner analysis region outlined in the centre of the grid. The right panel shows the average daily ammonia emissions, providing an example of how the averaging technique is applied to the inner grid only. In this figure, the entire grid runs at a high resolution of 10 km, while the aerosol and gas fields in the inner analysis region have been averaged over an 80 km grid.

The baseline high resolution simulation is conducted at 10 km. In this run, all fields (i.e. aerosol, dynamics, meteorology) are simulated at 10 km resolution, and it will be referred to as FRA10. Ten kilometres was chosen as it is the highest recommended resolution WRF-Chem can run with a convective parameterisation. Resolutions between 2 and 10 km are considered to be in the convective grey zone, where convection is neither fully resolved by the dynamics, neither fully parametrized [*Gerard*, 2007]. At resolutions higher than 2 km, convection is explicitly resolved and a convective parameterisation is not required. Because current global climate models are unable to explicitly resolve convection at this stage, I chose to use a convective parameterisation so that the results will be comparable to global climate model simulations.

To determine how the sub-grid variability or aerosol processes impacts model predictions of important aerosol parameters, three "aerosol averaged" runs are conducted during which the aerosol resolution was set to 40 km, 80 km, and 160 km, while maintaining a resolution of 10 km in all other model fields. These runs are referred to as

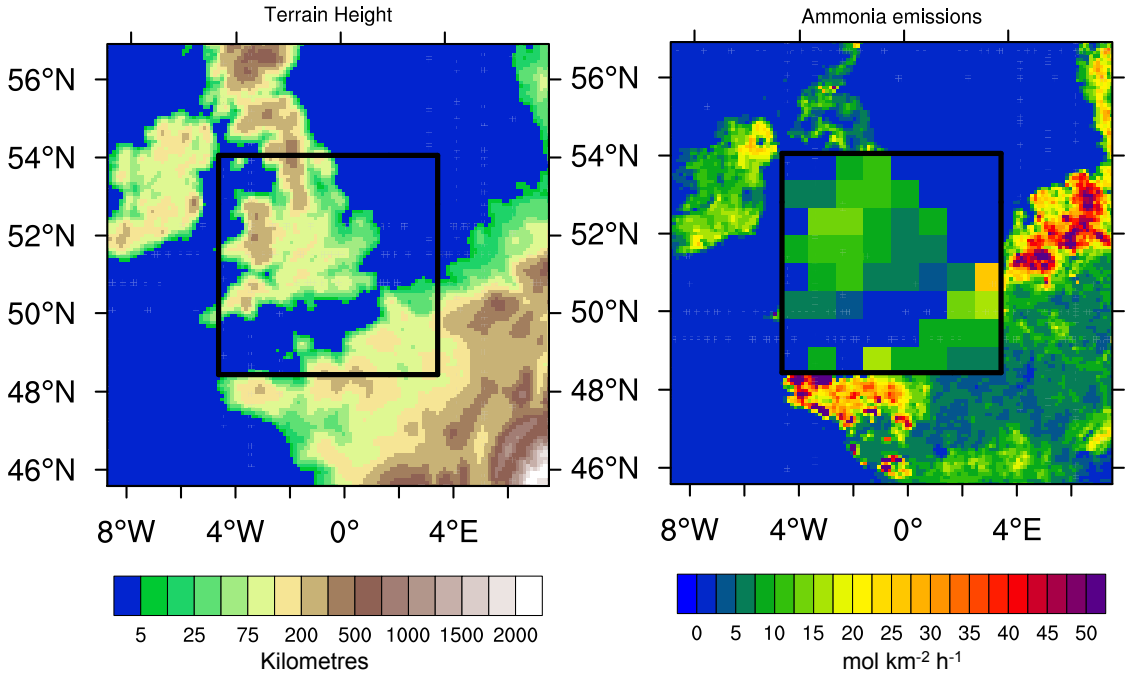

Figure 4.2: First panel shows terrain height (in metres) of the WRF-Chem domain. The outer frame represents the total high resolution 10 km domain; the inner box represents the region over which the averaging technique is applied. The second panel shows daily averaged ammonia emissions in mol/km^2/h . The inner domain has been averaged over 80 km; this provides a visual representation of how the aerosol averaged simulations work. The analysis presented in this paper is conducted over the inner region.

AA40, AA80 and AA160, respectively.

The majority of the analysis focuses on comparisons between FRA10 and AA80. AA80 represents an upper end resolution at which aerosols can be simulated in current GCMs for climate simulations purposes, and therefore demonstrates the degree of aerosol variability that these models are able to capture. The results of AA40 and AA160 are used to show the effect of increasing and decreasing the resolution of aerosol processes with respect to this current GCM resolution. In addition to these simulations, a second full resolution simulation is conducted at a resolution of 80 km (FRA80). This simulation will also be compared to FRA10 in order to demonstrate how traditional resolution comparison studies that simply vary model grid spacings to investigate aerosol variability miss important information due to their inability to

Table 4.1: Description of WRF-Chem simulations analysed in this study.

Abbreviation	Simulation description
FRA10	Entire model is run at 10 km resolution
FRA80	Entire model run at 80 km resolution
AA40	Model run at 10 km; aerosols and gases at 40 km
AA80	Model run at 10 km; aerosols and gases at 80 km
AA160	Model run at 10 km; aerosols and gases at 160 km

separate aerosol and meteorological effects. Table 4.1 summarises the different WRF-Chem simulations analysed in this paper.

The model simulations are conducted for one month from May 1 - 31, 2008. The first two days are used as a spin-up period; therefore, the analysis is carried out over the period from May 3 - 31, 2008. The UK and surrounding area experiences seasonal differences in aerosol concentrations. Observations show that the highest particulate mass concentrations occur in the first four months of the year, and lowest concentrations during later summer. This is likely due to greater emissions from heating and to reduced dispersion in the winter [*Harrison et al.*, 2012]. Seasonality has an effect on aerosol number concentrations as well, showing the opposite trend as the observed mass concentrations. The UK shows high seasonal variation in aerosol number and large variance of intra-seasonal concentrations with a prominent spring-summer maximum in all particle sizes [*Asmi et al.*, 2011]. As the simulation takes place in May, one expects aerosol concentrations between the summer and winter extremes.

4.1.2 Model Configuration

This study uses version 3.3.1 of WRF-Chem. This model is developed by the National Oceanic and Atmospheric Administration (NOAA) and is currently under active development by NOAA and other institutions. A complete description of the model can be found in *Grell et al.* [2005] and *Fast et al.* [2006].

The meteorological model WRF [*Skamarock and Klemp*, 2008] is a mesoscale nu-

Table 4.2: Physical and chemical options used in WRF-Chem configuration.

Process	WRF-Chem Option
Cloud microphysics	Lin
Long-wave radiation	RRTM
Short-wave radiation	Goddard
Surface layer	Monin-Obukhov
Land-surface model	Noah LSM
Boundary Layer scheme	YSU
Photolysis scheme	Fast-J
Cumulus parameterization	New Grell (G3)
Gas-phase mechanism	RADM2
Aerosol module	MADE/SORGAM

merical weather prediction system designed for both operational forecasting and atmospheric research purposes across scales ranging from metres to hundreds of kilometres. WRF-Chem provides a number of options for gas-phase chemistry and aerosol processes, including biogenic and anthropogenic emissions, dry and wet deposition, photolysis, vertical turbulent mixing, gas and aqueous phase chemical transformation, aerosol chemistry and microphysics as well as aerosol direct and indirect effects through interaction with atmospheric radiation and cloud microphysics.

The main options for the physical and chemical schemes employed in the simulations are summarised in Table 4.2. The two-moment Lin microphysics scheme was used with an added prognostic treatment of cloud droplet number [*Lin et al.*, 1983]. RRTM long-wave and Goddard short-wave radiation modules are used [*Mlawer et al.*, 1997; *Chou and Suarez*, 1994]; however aerosol feedbacks to the radiation schemes are turned off to ensure the meteorology is identical between runs. Other options chosen are the Monin-Obukhov surface layer scheme [*Monin and Obukhov*, 1954], the unified Noah Land Surface Model [*Chen and Dudhia*, 2001], the Yonsei University (YSU) planetary boundary layer scheme [*Hong et al.*, 2006] and New Grell 3D ensemble cumulus parameterisation [*Grell and Devenyi*, 2002]. Gas-phase atmospheric chemistry is based on the Regional Acid Deposition Model, version 2 (RADM2), which includes 21 inorganic and 42 organic chemical species with 158 reactions, of which 21

are photolytic [*Stockwell et al.*, 1990].

The aerosol module used in this analysis is the MADE/SORGAM module, consisting of the Modal Aerosol Dynamics Model for Europe (MADE), which handles the inorganic and primary organic constituents, and the Secondary Organic Aerosol Module (SORGAM), which handles the secondary organic fraction [*Ackermann et al.*, 1998; *Schell et al.*, 2001]. In MADE/SORGAM, the aerosol size distribution is described by three overlapping modes, representing the Aitken, accumulation, and coarse modes. The distribution within each mode is assumed to be log-normal as follows:

$$n(\ln d_p) = \frac{N}{\sqrt{2\pi}\ln\sigma_g}\exp\left[-\frac{1}{2}\frac{(\ln d_p - \ln d_{pg})^2}{\ln^2\sigma_g}\right]$$

where N is the number concentration, d_p the particle diameter, d_{pg} the median diameter, and σ_g the standard deviation of the distribution. The standard deviations are fixed to 1.7, 2.0 and 2.5 for the Aitken, accumulation and coarse modes, respectively [*Ackermann et al.*, 1998].

The aerosol species treated in MADE/SORGAM are ammonium (NH_4^+), nitrate (NO_3^-), sulphate (SO_4^{2-}), elemental carbon (EC), organic matter (OM – primary and secondary), aerosol water, sea salt, and mineral dust. The processes treated are homogeneous nucleation in the sulphuric acid-water system, condensation of sulphuric acid vapour, and coagulation by Brownian motion. Aerosol water uptake and formation of nitrate and ammonium is determined through the ammonia/nitric acid/sulphuric acid thermodynamic equilibrium system, which is parameterised based on the Model for an Aerosol Reacting System (MARS) [*Saxena et al.*, 1986]. Photolysis rates are simulated by the Fast-J scheme [*Wild et al.*, 2000], and the dry deposition velocities are determined by the Wesely parameterization [*Wesely*, 1989]. Wet deposition is handled in a simplified parameterisation of convective updrafts for trace gases and inorganic aerosols. There is currently available a full wet deposition module coupled with aqueous chemistry; however, these options are only available when aerosol radiative feedback is turned on. Because the aim of this experiment is to compare simulations

with identical meteorology, aerosol feedback to the radiation schemes must be switched off. Without wet deposition due to large-scale precipitation, a significant removal process is missing, which will likely result in higher aerosol concentrations than if the process were included.

All simulations used identical initial and boundary conditions generated by WRF-Chem from idealised profiles. The values are based on idealised, northern hemispheric, mid-latitude, clean environmental, vertical profiles from the NOAA Aeronomy Lab Regional Oxidant Model [*McKeen et al.*, 1991]. Meteorological boundary conditions were nudged to National Centers for Environmental Protection Final (NCEP FNL) operational global analysis data, which are available every 6 hours on a 1°by 1° grid.

Emissions

Anthropogenic emissions are taken from the Netherlands Organization for Applied Scientific Research (TNO), a detailed European gridded emission inventory developed by *van der Gon et al.* [2010] in the framework of the European MACC project (http://gmes-atmosphere.eu). The inventory is an update to the TNO 2005 emission database prepared for the GEMS project (http://gems.ecmwf.int) and is a European-wide, high resolution (1/8° lon x 1/6° lat) inventory for NO_x, SO_2, non-methane volatile organic compounds (NMVOC), CH_4, NH_3, CO, PM_{10} and $PM_{2.5}$. The dataset consists of anthropogenic emissions by country for the ten Source Nomenclature for Air Pollution (SNAP) sectors: energy transformation, small combustion sources, industrial combustion, industrial processes, extraction of fossil fuels, solvent and product use, road transport, non-road transport, waste handling, and agriculture. Scaling factors have been developed to scale the 2005 inventory to all years between 2003 and 2007. In this study, emissions from the 2007 database are used. The emissions are interpolated to the WRF domain to give hourly emissions per square kilometre.

The $PM_{2.5}$ emissions are broken into components of organic carbon, elemental carbon, sulphate, and "other mineral components" using composition profiles developed

for the TNO inventory. The derived composition profile provides mass fractions per sector per country to break down $PM_{2.5}$ mass into its components. OC, EC, particulate sulphate and "other mineral components" are split 20% into Aitken mode and 80% accumulation. PM_{10} emissions remain unspeciated as coarse mode particulate matter. Total NMVOC emissions are divided into their constituent RADM2 species to be handled by WRF-Chem.

Biogenic emissions are calculated online with a module based on the parameterisation by *Guenther et al.* [1994] using the U.S. Geological Survey 24 land use categories provided by the standard WRF configuration. The land use data is supplied at a 10 metre resolution. Sea salt and dust emissions [*Shaw et al.*, 2008] are also calculated online and are proportional to 10-metre wind speed over salt water for sea-salt and over non-urban land surfaces with sparse vegetation for dust.

4.2 Results

The results are presented in three sections. The first two sections explore the impact of aerosol sub-grid variability on AOD at 600 nm and CCN at 0.5% supersaturation, respectively, using the "aerosol averaged" technique described earlier. The primary focus is on comparisons between the full resolution run at 10 km (FRA10) and the aerosol averaged run at 80 km (AA80), with a brief exploration of the effect of increasing and decreasing aerosol resolution by presenting results from the AA40 and AA160 simulations. The third section presents results from the full resolution run at 80 km (FRA80) to demonstrate the difficulty in separating meteorological and aerosol effects in traditional model resolution studies.

In all comparisons, the FRA10 simulation is taken as the "truth". The FRA10 simulation is intended to be representative of typical aerosol conditions in the specific environment of the simulation and is meant to capture most of the aerosol variability important for accurately depicting aerosols' microphysical evolution and effect on climate.

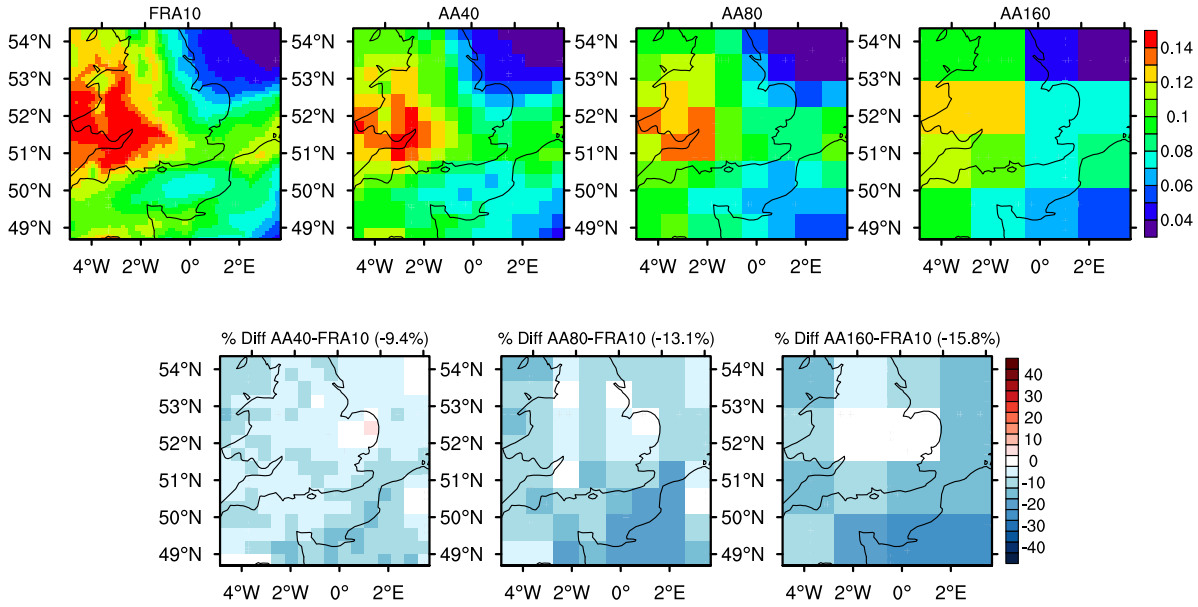

Figure 4.3: Simulated mean spatial distribution of AOD for the FRA10, AA40, AA80, and AA160 runs (top row) from May 3 - 31, 2008. The bottom row represents the percent difference between each aerosol averaged run and FRA10. The number in brackets in the bottom row represents the mean percentage difference in the two runs.

4.2.1 Effect of aerosol sub-grid variability on AOD

AOD is a measure of the column-integrated extinction and depends on aerosol number size distribution, shape, chemical composition, and the water content of aerosols. Figure 4.3 presents results of simulated AOD for the FRA10, AA40, AA80 and AA160 where the resolution of aerosol and gaseous species is varied from 10 km to 40 km, 80 km, and 160 km, respectively. The differences are calculated by first coarse-graining the results from the high resolution simulation to the grid of the low resolution run to which it is being compared. This eliminates differences due to the inevitably smoother low resolution run not being able to capture the same degree of variability as the high resolution simulation. At lower aerosol resolutions, simulated AOD is underestimated with respect to the high resolution run. Relative to FRA10, the negative bias in AOD increases from an average of -9.4%, to -13.1% to -15.8% as the aerosol resolution is decreased to 40 km, 80 km, and 160 km, respectively. The mechanisms behind this underestimation are investigated by exploring differences between the FRA10 and AA80

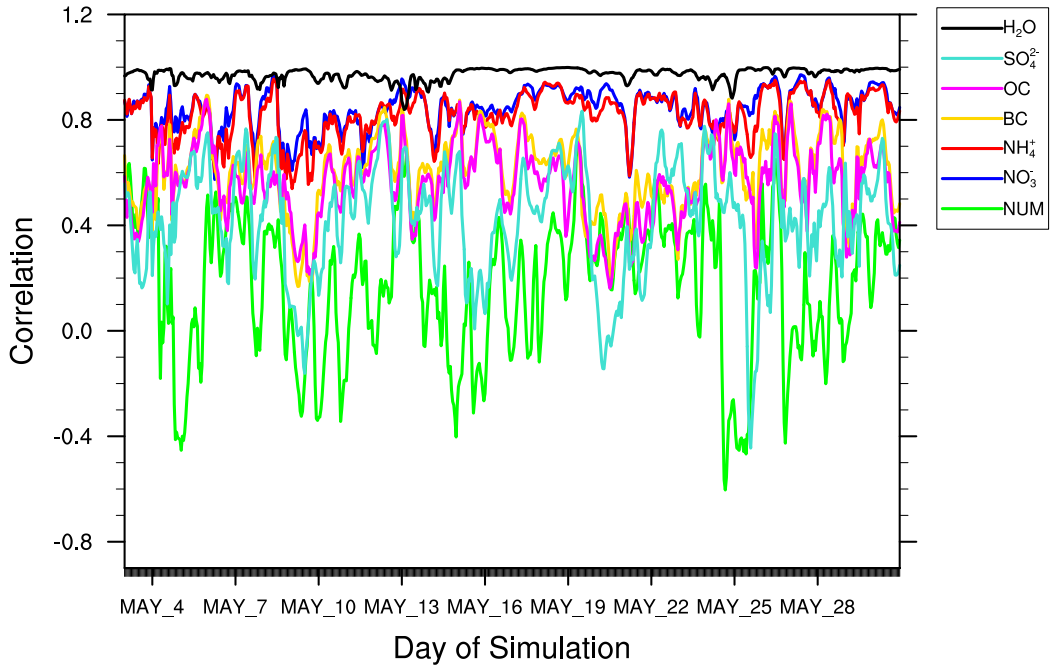

Figure 4.4: Pattern correlation between the hourly spatial differences in AOD and the hourly spatial differences in column amount accumulation mode number (NUM, in $\#/m^2$), and column amount accumulation mode mass (in $\mu g/m^2$) of nitrate, ammonium, black carbon, organic carbon, sulphate, and aerosol water content. The correlations are calculated for the differences between the AA80 and FRA10 simulations.

simulations.

Figure 4.4 shows the pattern correlation between the hourly spatial differences in AOD in the FRA10 and AA80 simulations and the spatial differences in a number of aerosol parameters known to have an impact on AOD. The correlation analysis demonstrates that differences in AOD between the FRA10 and AA80 simulations are highly correlated to differences in accumulation mode aerosol water content, with an average correlation of 0.97 over the entire time period. Accumulation mode nitrate and ammonium also demonstrate high correlations, with averages of 0.84 and 0.82, respectively.

It is clear that uptake of water by accumulation mode aerosols plays an important role in the underestimation of AOD in the low aerosol resolution runs. Figure 4.5 shows the average spatial distribution of accumulation mode water content for

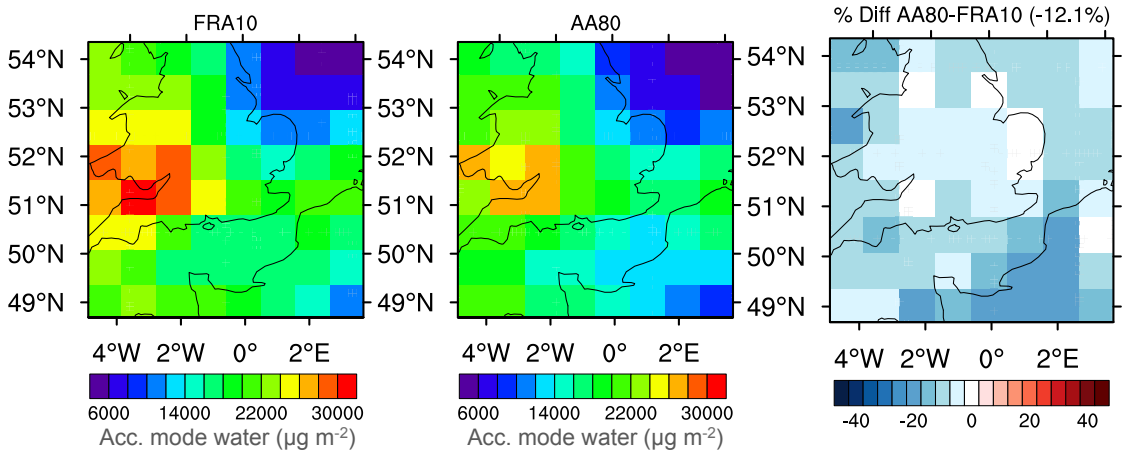

Figure 4.5: Simulated mean spatial distribution of column amount accumulation mode aerosol water content in $\mu g/m^2$ for the FRA10 simulation (first panel), the AA80 simulation (second panel), and the percent difference between the two (third panel), averaged from May 3 - 31, 2008. The number in brackets on the third panel represents the mean percentage difference in the two runs.

the FRA10 simulation, which has been coarsened to the 80 km grid (first panel), the AA80 simulation (second panel), and the percent difference between them (third panel). Compared to Figure 4.3, one can see the strong relationship between the two parameters, as confirmed by the correlation analysis.

This is not surprising as many studies have shown that aerosol water content has a large impact on aerosol optical properties. *Shinozuka et al.* [2007] used aircraft measurements to show that the fraction of ambient AOD due to water uptake is 37 ± 15% over continental U.S.; the fraction is likely even higher over marine environments. Using a box model, *Pilinis et al.* [1995], showed that the most important process in determining aerosol direct radiative forcing is increase in aerosol mass as a result of water uptake. In both the FRA10 and AA80 simulations aerosol water content makes up approximately two thirds of the total aerosol mass, making AOD highly sensitive to changes in water.

Investigation of aerosol water uptake in WRF-Chem

The question remains: what is causing differences in aerosol water content between the FRA10 and AA80 simulations? In WRF-Chem, the total aerosol water content is calculated using a program based on the Model for an Aerosol Reacting System (MARS) described in *Saxena et al.* [1986], which determines the amount of water taken up by sulphate (SO_4^{2-}), nitrate (NO_3^-), and ammonium (NH_4^-) aerosols. At thermodynamic equilibrium, the amount of water contained in these particles depends on temperature, relative humidity (RH), and aerosol amount/composition, which, in turn, depends on the concentrations of the gaseous precursors ammonia (NH_3), nitric acid vapour (HNO_3), and sulphuric acid vapour (H_2SO_4) [*Seinfeld and Pandis*, 2006]. This study was explicitly designed so that temperature and relative humidity are identical in both the FRA10 and AA80 simulations; therefore, the changes in aerosol water content must be due to changes in aerosol amount and/or composition.

Although the RH fields are the same in the two runs, different aerosol types react differently at particular levels of RH. At very low RH, inorganic aerosol particles are solid. As RH increases, the particles remain solid until the RH reaches a threshold level specific to the composition of the particle, at which point the particle absorbs water from the atmosphere and becomes an aqueous solution. This process is called deliquescence, and the RH at which the particle absorbs water is called the deliquescence relative humidity (DRH). An additional increase in RH leads to further uptake of water by the particle. Conversely, as the RH decreases, evaporation of water occurs; however, the particle remains supersaturated until a lower RH than its DRH, at which point the particle crystallises, becoming a solid once again [*Seinfeld and Pandis*, 2006]. Aerosols such as nitrate and ammonia exhibit this deliquescent behaviour, with a DRH of approximately 60% [*Saxena et al.*, 1986]. Sulphuric acid, on the other hand, is hygroscopic, meaning it readily absorbs water at nearly all RH and does not display this step-function behaviour in water absorption.

In the sulphate-ammonium-nitrate-water system, the relative amounts of these

aerosols are determined by competition between the following two thermodynamic equilibrium reactions [*Seinfeld and Pandis*, 2006]:

$$2\,NH_{3(g)} + H_2SO_{4(g)} \rightleftharpoons (NH_4)_2SO_{4(aq)}$$

$$NH_{3(g)} + HNO_{3(g)} \rightleftharpoons NH_4NO_{3(aq)}$$

In this system, the first reaction dominates; ammonia preferentially neutralises sulphuric acid due to its low saturation vapour pressure and drives the reaction to the aerosol phase. Therefore, ammonium nitrate (NH_4NO_3) is only formed only when there is sufficient ammonia to neutralise the amount of sulphate present, i.e. in areas of high concentrations of ammonia and/or low concentrations of sulphate. $(NH_4)_2SO_4$ is the preferred form of sulphate, meaning that each mole of sulphate will remove two moles of ammonia from the gas phase. It therefore makes sense to divide this system into two cases of interest: high-ammonia and low-ammonia.

In the low-ammonia case, there is insufficient NH_3 to neutralise the available sulphate. The sulphate present will tend to drive the nitrate to the gas phase. The partial pressure of ammonia is low, resulting in zero or near-zero levels of ammonium nitrate.

In the high-ammonia case, there is excess ammonia so that the aerosol phase is largely neutralised. The ammonia that does not react with sulphate will be available to react with nitric acid vapour to produce NH_4NO_3.

Essentially, at very low ammonia concentrations, ammonium sulphate primarily constitutes the aerosol composition. As ammonia increases, ammonium nitrate becomes a significant aerosol constituent. The aerosol liquid water content responds nonlinearly to these changes, reaching a minimum close to the transition between the two regimes. Figure 4.6 shows this minimum in the relationship between aerosol water content and various aerosol concentrations as a function of total ammonia. One can see that nitrate concentrations only increase with ammonia once sulphate has been neutralised. At this point, sulphate concentrations remain constant, and aerosol water content increases with increasing nitrate. In addition to these constraints, the existing

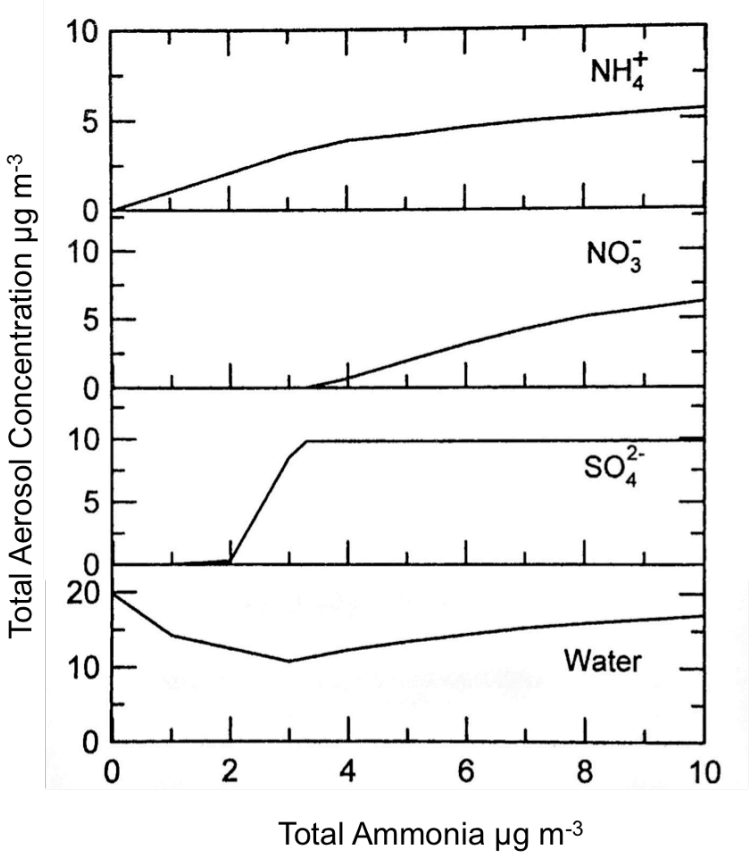

Figure 4.6: From *Seinfeld and Pandis* [2006]. Calculated aerosol composition as a function of total ammonia (temperature = 298 K, RH = 70%)

aerosol will only take up water if the relative humidity is sufficiently high (i.e. greater than the DRH) [*Seinfeld and Pandis*, 2006].

During the 28 day simulation, the mean aerosol water content in the AA80 run is 12.1% less than in the high resolution FRA10 run; this difference reaches up to 36% less in some regions (Figure 4.5). Exploring the aerosol and gaseous species within the equilibrium system, Figure 4.7 shows the mean percent difference of the total column amounts of sulphate (a), nitrate (b), ammonia (c), and nitric acid (d) between the FRA10 and AA80 simulations. Overall, the changes are small in the various species with average percent differences of +4.7%, -2.6%, -6.6%, and +6.1% for sulphate, nitrate, ammonia and nitric acid, respectively. Ammonia and nitrate are both slightly underestimated in the AA80 run; however, the magnitude and spatial distribution of the differences do not match the observed underestimation in aerosol water content.

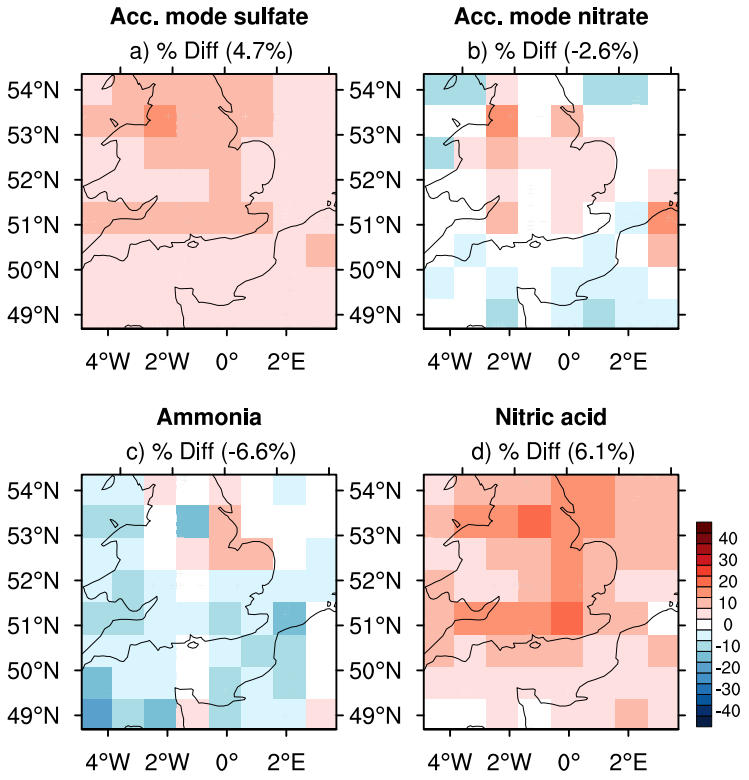

Figure 4.7: Percent differences between the AA80 and FRA10 (AA80 - FRA10) simulations in the mean spatial distribution of various species in the aerosol water equilibrium system. The means were taken over the evaluation period of May 3 - 31, 2008.

This is due to the fact that the aerosol species do not take up water under all conditions (as discussed above), and so looking at mean column differences over the full duration of the simulation may miss important information. To gain a better understanding of why aerosol water content is lower in the AA80 simulation and how it is affected by the chemical system, one must divide the system into regimes based on relative humidity and mass fraction of ammonia to sulphate, as is done in the MARS program in WRF-Chem.

To simplify the discussion, four main regimes from MARS are defined as: High RH and High Fraction of ammonia to sulphate (HRHF); High RH and Low Fraction (HRLF); Low RH and High Fraction (LRHF); and Low RH and Low Fraction (LRLF). High RH refers to a humidity greater than or equal to 40%, whereas a low RH is less than 40%. A value of 40% was used to approximate the RH of crystallisation of

Table 4.3: Results from regime analysis. The concentrations are expressed in mol/m^3. The four regimes represent the equilibrium conditions for the formation of sulphate and nitrate aerosol and are divided according to high and low relative humidity (HR, LR), and high and low fraction of ammonia to sulphate (HF, LF). The differences shown correspond to AA80 - FRA10.

	% of time	$[SO_4^{2-}]$	$[NO_3^-]$	$[NH_3]$	$[HNO_3]$	$[H_2O]$
Overall						
FRA10	100	2.73	13.6	13.0	20.7	245
AA80	100	2.85	13.3	11.3	21.4	226
Difference	-	+0.12	-0.3	-1.7	+0.7	-19
HRHF Regime						
FRA10	40	5.19	33.6	30.7	40.5	606
AA80	44	5.07	29.5	23.4	38.1	511
Difference	+4	-0.12	-4.1	-7.3	-2.4	-95
HRLF Regime						
FRA10	11	1.54	0.016	0.032	7.28	19.9
AA80	7	1.27	0.024	0.051	6.67	12.7
Difference	-4	-0.27	+0.008	+0.019	-0.61	-7.2
LRLF Regime						
FRA10	41	0.66	0.004	0.032	5.58	0.92
AA80	37	0.59	0.008	0.038	5.64	0.58
Difference	-4	-0.07	-0.004	+0.006	+0.06	-0.34

ammonium nitrate and ammonium sulphate. A high fraction of ammonia to sulphate refers to a fraction greater than or equal to 2.0, whereas a low fraction is less than 1.0. The model includes regimes for mass fractions between 1.0 and 2.0; however, they are not included in this analysis due to their relatively infrequent occurrence during the simulation. Because nitrate can only exist once there is sufficient ammonia to neutralise sulphate and can only absorb water at relative humidities above its DRH, the HRHF regime is the only regime in which nitrate can uptake water.

The amounts of each chemical species and the total water content within each of the regimes are compared in Table 4.3. The concentrations included in the analysis are measured in mol/m^3 and represent the average concentrations of the chemical species within a particular regime. LRHF is not included in the table because the aerosol water content is set to zero in this regime. This is due to the fact that although there may be sulphate and nitrate present, there is insufficient humidity to transition

them to their aqueous states. One point to note regarding the LRHF regime, however, is that the AA80 simulation spends approximately 12% of its time in this regime, compared to 8% for the FRA10. This may therefore be a small contributing factor to the underestimation in aerosol water in AA80.

Looking at the overall differences, one sees similar behaviour as Figure 4.7; there is a large decrease in aerosol water, with small changes in all other species. By exploring the different regimes, one can see that the chemical system spends most of its time within the HRHF and the LRLF regimes. One also sees that the average aerosol water content is lower in AA80 compared to FRA10 in all three regimes; however, the absolute values of the concentrations in the HRHF regime are orders of magnitude higher than in the other two regimes, indicating that the HRHF has the largest impact on total aerosol water content. This is the high-humidity, ammonia-rich regime described above; in this regime both sulphate and nitrate aerosol can uptake water. This is the *only* regime in WRF-Chem in which nitrate aerosol can contribute to the total aerosol water content. In the HRHF regime, the AA80 simulation underestimates both sulphate and nitrate aerosol, however, the underestimation in nitrate is roughly an order of magnitude larger than that of sulphate. Also note that even though there is less ammonia in AA80, this does not impact the amount of time the system spends within the HRHF regime, meaning there is enough ammonia present to fully neutralise sulphate, but there is less leftover to form nitrate within the HRHF regime. Thus, although there is a small decrease in nitrate overall, the decrease is much larger under the conditions that are most favourable for nitrate to take up water. This leads to less aerosol water in the AA80 run.

The above observations are confirmed by examining the vertical profiles of ammonia, accumulation mode nitrate, accumulation mode aerosol water content, and AOD from the FRA10 and AA80 simulations, shown in Figure 4.8. The vertical profiles of ammonia (Figure 4.8a) reveal a $\sim$30% underestimation at the surface in the AA80 simulation, with very little differences at higher altitudes. The vertical profiles of ni-

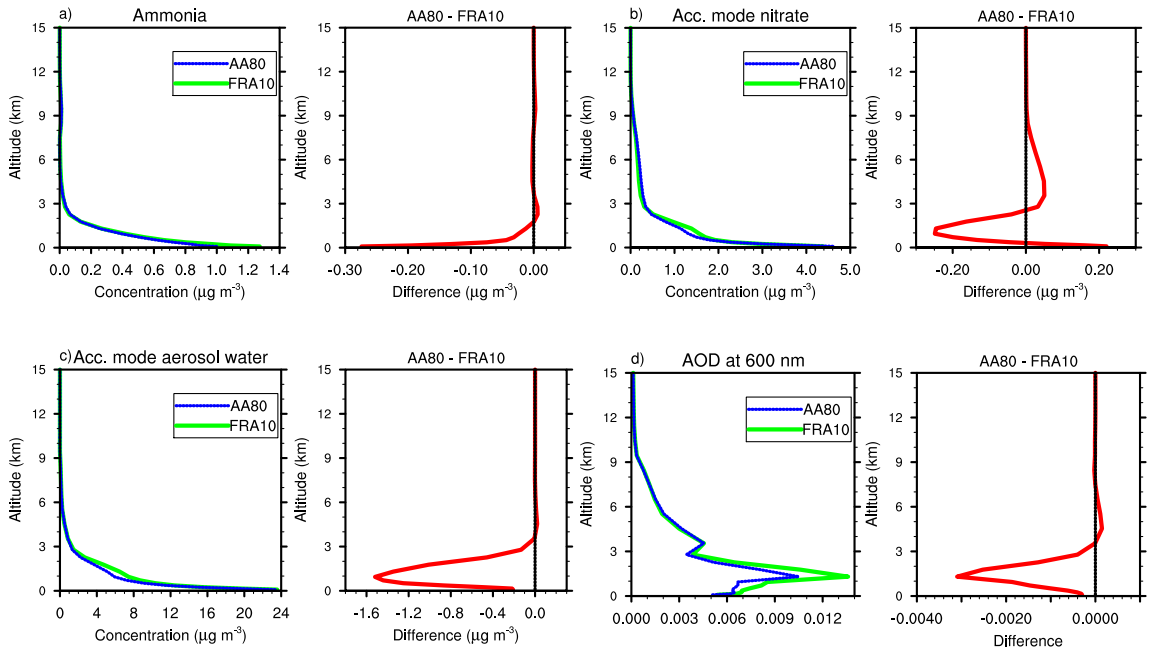

Figure 4.8: Vertical profiles of selected species in the gas-aerosol equilibrium system in $\mu g/m^3$ for the FRA10 and AA80 simulations (left column) and the absolute differences between the two simulations (AA80-FRA10, right column). The species include ammonia, (a), accumulation mode nitrate (b), accumulation mode aerosol water content (c), and AOD (d). The fields represent mean values over the analysis period of May 3 - 31, 2008.

trate (Figure 4.8b), however, show differences in the vertical distribution of nitrate at altitudes up to 9 km with the AA80 simulation having more nitrate at the surface, significantly less nitrate in the boundary layer (BL) and more nitrate above the BL compared to the FRA10 simulation. This appears to be the result of a smoother vertical distribution in the AA80 simulation compared with the sharper vertical gradients in FRA10. While the difference in total nitrate concentration between the two simulations is small (less than 3%), the differences in the BL reach up to 20%. The boundary layer is characterised as having high relative humidity and lower temperatures than the surface, which are the conditions under which nitrate most readily absorbs water. It is therefore this underestimation in BL nitrate that leads to an underestimation in aerosol water content in the BL(Figure 4.8c), and, ultimately, AOD (Figure 4.8d). Aerosol water content is largely unaffected by the small increases in nitrate at the

surface and above the BL since nitrate does not efficiently take up water under these conditions.

Understanding the mechanism causing the underestimation of BL nitrate in the low resolution simulation is complicated by the fact that nitrate is part of a coupled equilibrium system, which makes it difficult to isolate the way different processes affect nitrate at varying resolutions. The question remains: what factors contribute to the observed changes in nitrate? Does the underestimation of surface ammonia concentrations lead to a decrease in nitrate in the BL? If so, what is causing the underestimation in ammonia? While the complete explanation for the observed changes in nitrate is not fully understood, the following sections explore a number of mechanisms that may contribute to these changes.

Investigating changes in nitrate: Impact of equilibrium system

The non-linear nature of the nitrate equilibrium system makes it susceptible to changes in model resolution. In a previous study, *Metzger et al.* [2002] coupled a gas-aerosol equilibrium scheme to a global atmospheric chemistry-transport model and tested the effect of decreasing the full model resolution from 10°x 7.5° to 2.5°x 2.5° on aerosol nitrate. They found that boundary layer nitrate concentrations were 30-80% lower in the low resolution run. They attributed these large differences to the fact that aerosol nitrate formation non-linearly depends on the concentrations of its precursor gases.

To test whether the changes in boundary layer nitrate concentrations in the current study are related to changes in resolution of the aerosol and gaseous species within the equilibrium system, an alternative AA80 simulation was performed, where all aerosols and gases were averaged over the lower resolution grid *except* the species involved in the equilibrium, namely, sulphate aerosol, ammonium aerosol, ammonia, nitric acid, and nitrate aerosol. Figure 4.9 shows that the differences in aerosol water content between the FRA10 and the altered AA80 simulations virtually disappear, confirming that the underestimation in aerosol water content in the AA80 simulation can be attributed to

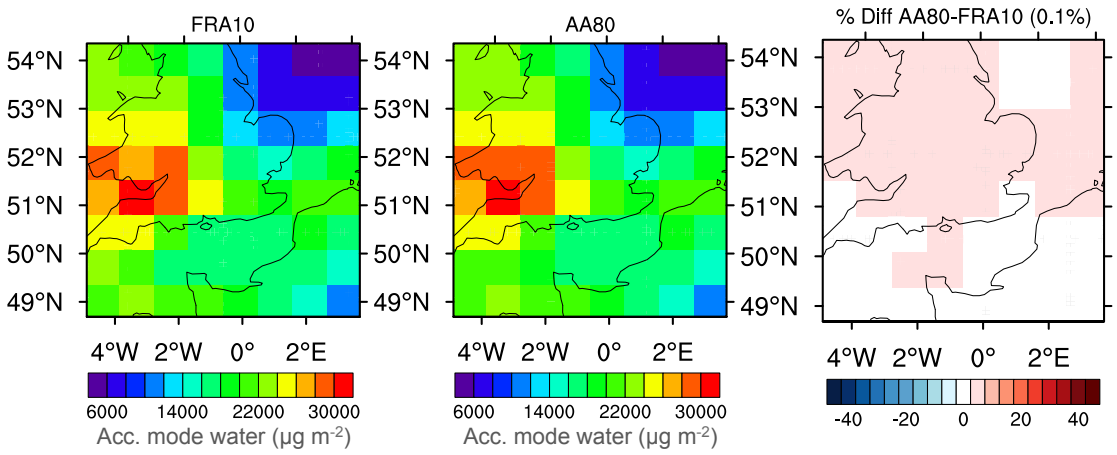

Figure 4.9: Mean spatial distribution of column amount of accumulation mode aerosol water content in $\mu g/m^2$ for the FRA10 simulation (first panel), an altered AA80 simulation where all aerosol and gaseous species are averaged over the lower resolution grid except for the species involved in the equilibrium system, (second panel) and the percent difference between the two (third panel) from May 3 - 31, 2008. The number in brackets on the third panel represents the mean percentage difference in the two runs.

neglecting the sub-grid variability of species within the nitrate equilibrium system.

To gain further insight into the influence of aerosol sub-grid variability on the nitrate equilibrium system, a number of sensitivity simulations are performed using a box model version of the system. The box model is identical to the coded version within WRF-Chem and simulates the gas-aerosol partitioning and subsequent aerosol water uptake. The box model requires as input the initial concentrations of the five species involved in the equilibrium (sulphate aerosol, ammonium aerosol, ammonia, nitric acid, and nitrate aerosol), temperature, and relative humidity and produces as output the equilibrium concentrations of each species as well as the aerosol water content at equilibrium. In the sensitivity tests, the input concentrations of four of the aerosol/gaseous species, as well as the temperature and relative humidity, are held constant and the input concentration of the fifth species is randomly sampled from a lognormal distribution. The standard deviation of this lognormal distribution characterises the spatial variability of the input aerosol concentration. A high standard deviation corresponds to a high spatial variability, thereby mimicking a high model

resolution. The sensitivity tests compare the difference in equilibrium concentrations when the input aerosol concentration has a high degree of variability versus a low degree of variability. The test is therefore analogous to measuring the response of the equilibrium system to a decrease in resolution of one aerosol/gaseous species while holding all other parameters constant.

Each test case consists of 1000 random samples; the high variability case has a standard deviation approximately 1.5 times greater than the low variability case, which matches the values of the standard deviations calculated from the WRF-Chem model output. The mean concentrations of the high variability and low variability lognormal distributions are identical and set to the mean concentration of that particular gas or aerosol from the FRA10 WRF-Chem simulation. This ensures that any differences in equilibrium concentrations are due solely to changes in aerosol/gas variability. The input concentrations of the other four aerosol and gaseous species are held constant over the 1000 samples; their values are also given by their corresponding mean concentrations in the FRA10 WRF-Chem simulation. The sensitivity tests are performed using mean concentrations at two different levels: model level 0 (0 km) and model level 6 (1 km), to compare how the equilibrium system responds to surface conditions versus boundary layer conditions.

The tests are conducted at six different relative humidities (0.50, 0.60, 0.70, 0.80, 0.90, 0.95) and four different temperatures (275K, 280K, 285K, 290K). The input variability of each of the five aerosol/gaseous species is changed from high to low one at a time, so that a total of 120 sensitivity tests are performed at each model level (5 aerosol/gaseous species x 6 relative humidities x 4 temperatures).

An example of the results from one sensitivity test is shown in Figure 4.10. In this particular test, the input concentrations of ammonia are randomly sampled at a high variability (in blue) and at a low variability (in red). The relative humidity is set to 0.70 and the temperature to 280K. The subplots show the effect of changing the variability of ammonia on the equilibrium concentrations of each aerosol and gaseous species, with

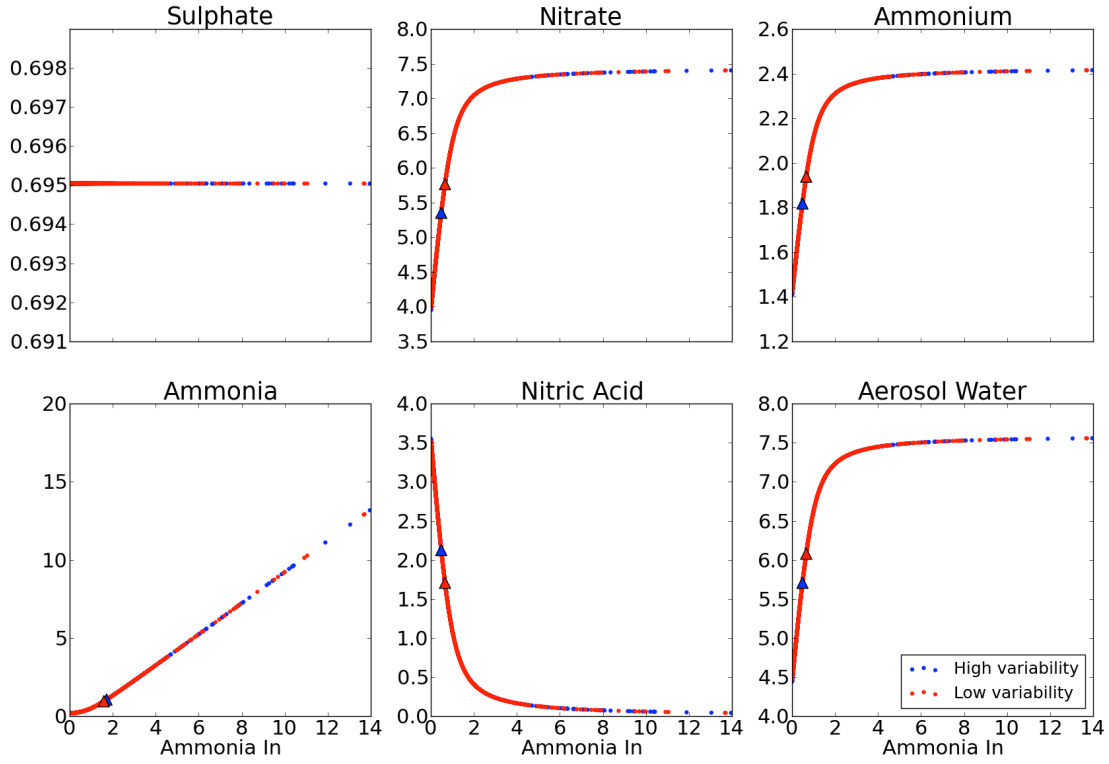

Figure 4.10: Example of sensitivity test where input ammonia concentrations are randomly sampled at high (blue) and low (red) variability (RH = 0.70, temperature = 280K). The subplots show the equilibrium concentrations (in $\mu g/m^3$) of individual aerosol/gaseous species as a function of input ammonia concentrations. The blue and red triangles represent the mean equilibrium concentrations of the aerosol/gaseous species in the high and low variability runs.

the blue and red triangles representing the mean equilibrium concentration of the high and low variability runs. This plot highlights the non-linear relationship between many of the species and ammonia. Remember that the means of the high and low variability input ammonia distributions are identical, so that if the relationships were linear, there would be no difference in the mean equilibrium concentrations. However, one can see that the mean concentration of nitric acid is lower in the low variability run, whereas the mean concentrations of nitrate, ammonium, and aerosol water are higher in the low variability run. There is also a small decrease in the mean equilibrium concentration of ammonia when the distribution of its input concentrations has a lower variability. The mean equilibrium concentrations of sulphate are unaffected by ammonia variability.

The results from all of the sensitivity tests are summarised in Figure 4.11 using

mean surface concentrations (left-hand side) and boundary layer concentrations (right-hand side) as inputs to the equilibrium calculations. The first row shows the effect of reducing the variability of each aerosol/gaseous species on ammonia. The y-axis represents the percent difference in the mean equilibrium concentrations of ammonia between the low variability and high variability runs (low - high). Each colour represents a different species whose variability was altered, e.g. the blue dots represent the runs when the variability of input sulphate was reduced. Each different dot within the same colour represents a test performed at a unique relative humidity and temperature value with darker colours corresponding to higher relative humidities and larger dots corresponding to higher temperatures. The second row shows the same for nitrate, and the third row shows the same for aerosol water.

Figure 4.11a shows that a reduction in the variability of nitrate, ammonia, and ammonium all result in lower ammonia concentrations at the surface by 10-15%. Reducing the variability of nitric acid has a small negative effect, and sulphate variability has a mixed effect on ammonia concentrations, depending on the relative humidity and temperature. The smallest differences tend to be at the lowest relative humidity and the highest temperature, but there is significant variation in these trends. In the boundary layer, one sees much higher percent differences, which is a consequence of lower ammonia concentrations having a higher sensitivity to changes in aerosol and gas variability. Reducing sulphate variability again produces mixed responses in mean ammonia equilibrium concentrations, and the rest of the aerosol/gaseous species result in lower ammonia concentrations by up to 30%.

Looking at the impact of aerosol and gas variability on nitrate (Figure 4.11b), one sees the opposite trend as ammonia. At the surface, reducing the variability of nitrate, ammonia, and ammonium results in higher mean nitrate concentrations up to 20%, whereas reducing sulphate and nitric acid variability have small effects. While most of the changes result in higher nitrate concentrations, one sees decreases in nitrate of close to 10% when the variability of sulphate, nitric acid, and nitrate is reduced at the lowest

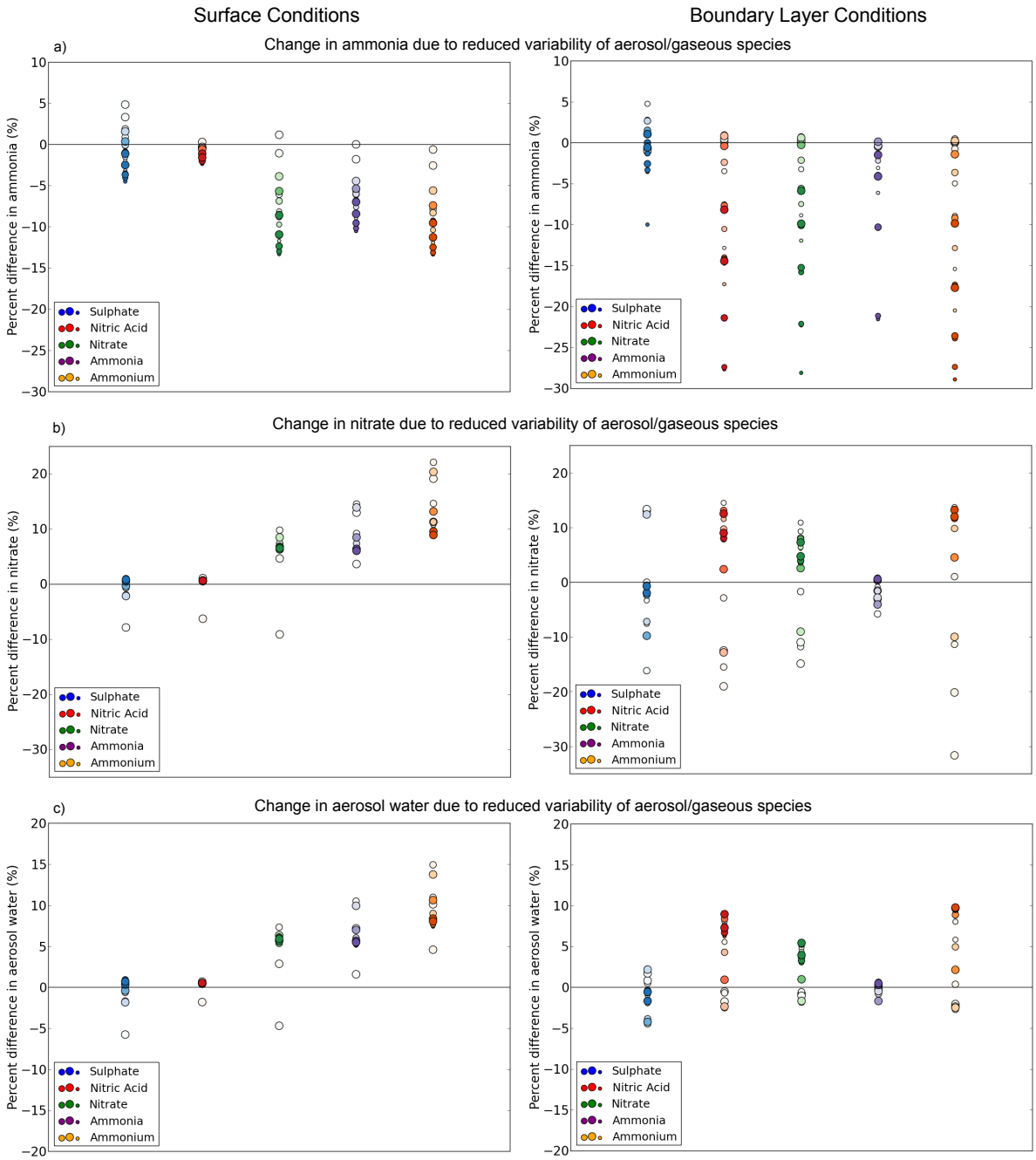

Figure 4.11: Summarises the results from the box model sensitivity tests for ammonia (first row), nitrate (second row), and aerosol water content (third row). The left-hand side uses mean surface conditions as input, and the right-hand side shows the same for boundary layer conditions. The markers show the difference in the mean ammonia (a), nitrate (b), aerosol water content (c) between the low and high variability runs. Each colour represents a different aerosol/gaseous species whose variability was reduced during the run. The different markers within one colour represent a test performed at a unique relative humidity and temperature value.

relative humidity and highest temperature. The boundary layer shows a much more variable picture. Reducing the variability of each aerosol and gaseous species can result in either an increase or a decrease in nitrate equilibrium concentrations, depending on the relative humidity and temperature conditions. While there is no strict trend, one tends to see decreases in nitrate concentrations at lower relative humidities and higher temperatures and increases in nitrate at higher relative humidities and lower temperatures.

Aerosol water content (third row) follows a similar trend to nitrate except that the percent differences in the boundary layer are smaller in magnitude. The effect on ammonium, nitric acid, and sulphate are not shown; however, nitric acid behaves similarly to ammonia, ammonium behaves similarly to nitrate, and sulphate shows no sensitivity to decreases in variability of the other species present.

Relating these sensitivity test results back to the observed changes in the WRF-Chem, there are a few key observations to note. Firstly, these tests highlight the complicated nature of this equilibrium system. By simply changing the degree of variability of one input parameter, large differences arise in equilibrium concentrations of all aerosol and gaseous species (except sulphate) within the equilibrium. To get a better sense of the complexity of this system, Figure 4.12 provides an example of a sensitivity test during which two input parameters are varied (in this case ammonia and nitrate, at a relative humidity of 0.70 and temperature of 280K). One can see that the relationships become significantly more scattered and less predictable. In the WRF-Chem simulations, the variability of all aerosol and gaseous species are changed simultaneously, which makes the subsequent impact on the equilibrium system difficult to predict.

Nevertheless, the sensitivity tests provide some insight. The differences in the some of the sensitivity runs are of similar magnitude to the observed differences between the FRA10 and AA80 simulations, meaning the equilibrium system could feasibly be the source of these differences in the WRF-Chem simulation. The majority of the

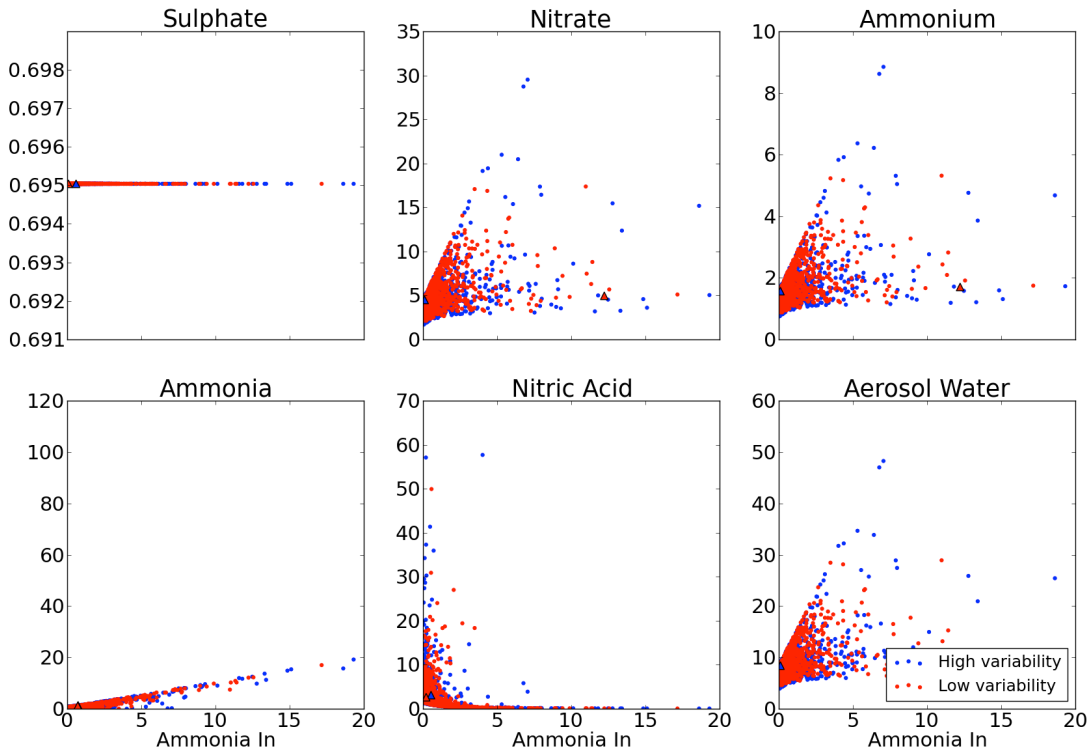

Figure 4.12: Example of sensitivity test where input ammonia concentrations and input nitrate concentrations were randomly sampled at high (blue) and low (red) variability (RH = 0.70, temperature = 280K). The subplots show the equilibrium concentrations (in $\mu g/m^3$) of individual aerosol/gaseous species as a function of input ammonia concentrations.

sensitivity tests show that lower aerosol and gas variability results in less ammonia and more nitrate at the surface, which follows the trend observed in the FRA10 and AA80 WRF-Chem simulations. While the impact on nitrate in the boundary layer is more variable, one does see decreases in mean nitrate concentrations, particularly at lower relative humidities and higher temperatures. Aerosol water shows a smaller negative effect, likely due to the fact that the largest decreases in nitrate occur under unfavourable conditions for water uptake. While there is likely more to the story than what is shown from these sensitivity tests, one can see that the non-linearities in the equilibrium system have significant effects on mean aerosol/gas concentrations and therefore may contribute to the observed differences in the FRA10 and AA80 simulations.

Investigating changes in nitrate: Impact of convective transport

Another mechanism known to have an impact on the gas-aerosol partitioning of nitrate is vertical mixing in the convective boundary layer. *Aan de Brugh et al.* [2012] used a single-column model that included an equilibrium aerosol scheme similar to WRF-Chem to test the effect of varying the equilibrium timescale on nitrate concentrations. They found that the gas-aerosol equilibrium scheme shows an average shift toward to aerosol phase when the equilibrium timescale is increased. They attributed this shift to vertical mixing, claiming that in the convective boundary layer, air from the upper boundary layer is mixed towards the surface. That air experienced a lower temperature and higher relative humidity and thus contains more aerosol nitrate and less nitric acid compared to the equilibrium at the surface. If a non-instantaneous equilibrium is assumed, the nitrate remains longer in the aerosol phase, resulting in a higher aerosol fraction at the surface.

It is possible that vertical mixing is also causing the observed differences in the FRA10 and AA80 simulations. In these simulations, nitrate-containing air in the boundary layer mixes with layers above and below. In the high resolution run, the mixing occurs as normal, with some nitrate-containing air being removed from the BL by mixing with adjacent layers. When nitrate concentrations are low or depleted in the high resolution run, further removal of nitrate can only occur after it has been replenished by advection or emission/secondary production. In the AA80 run, the removal mechanism occurs at a high resolution but nitrate concentrations are spread over the low resolution grid box. In this scenario, the nitrate concentrations are continuously averaged and re-distributed over the large grid area so that the nitrate that has been removed from the BL by the high-resolution mixing is instantaneously replenished by the averaging over neighbouring grid boxes. It is therefore possible that more nitrate is being depleted from the BL in the low resolution run due to the continuous spreading of nitrate over areas where it has already been removed by convective transport.

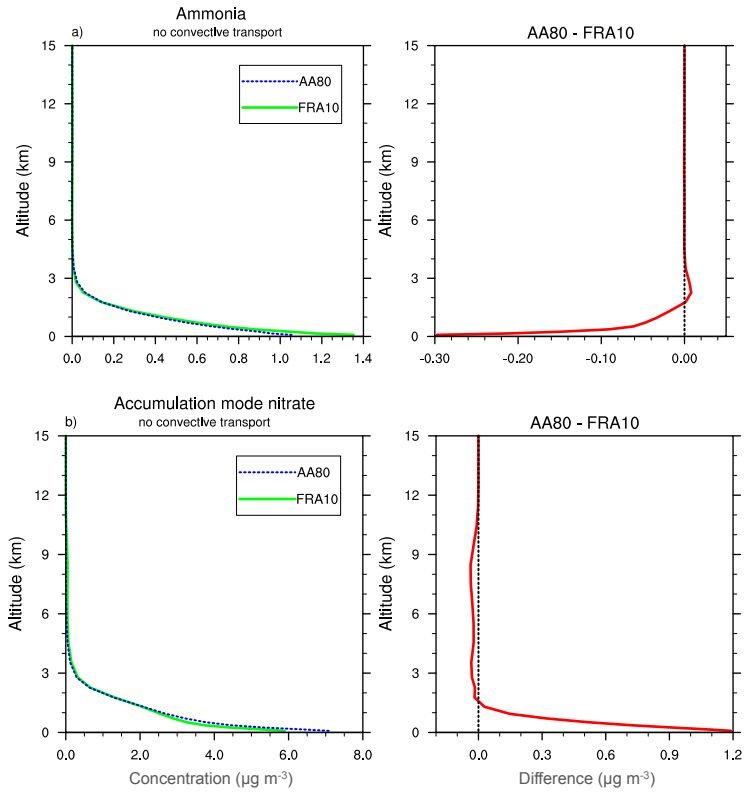

Figure 4.13: Vertical profiles of ammonia (a) and accumulation mode nitrate (b) concentrations in $\mu g/m^3$ for the FRA10 and AA80 simulations (left column) and the absolute difference between the two simulations (AA80-FRA10, right column) with convective transport of aerosols and trace gases turned off. The fields represent mean values over the analysis period of May 3 - 31, 2008.

To test whether convective transport plays a role in the underestimation of nitrate in the BL, the FRA10 and AA80 simulations were repeated but with convective transport turned off. Figures 4.13 and 4.14 show the results of these simulations. Figure 4.13 demonstrates the effect of turning off convection on the vertical profiles of ammonia (a) and accumulation mode nitrate (b). Ammonia shows very little difference from the original FRA10 and AA80 simulations, i.e. the underestimation of ammonia at the surface in AA80 persists when convective transport is turned off. However, a different picture emerges for nitrate. The underestimation of nitrate in the BL in the original AA80 simulation disappears when convective transport is turned off and results in a higher overestimation at the surface. This result, in fact, agrees with observations from the sensitivity tests in the previous section, which showed a tendency to simulate

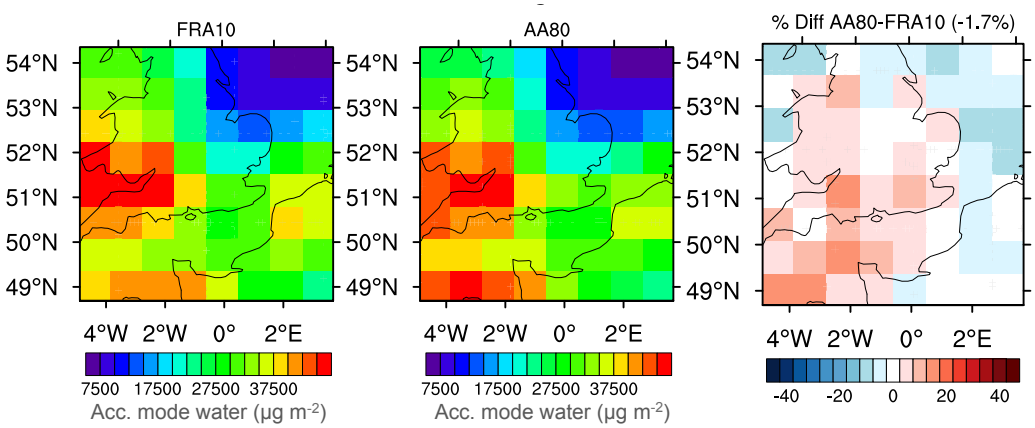

Figure 4.14: Mean spatial distribution of column amount of accumulation mode aerosol water content in $\mu g/m^2$ for the FRA10 simulation (first panel), the AA80 simulation (second panel) and the percent difference between the two (third panel) from May 3 - 31, 2008 with convective transport turned off. The number in brackets on the third panel represents the mean percentage difference in the two runs.

less ammonia and more nitrate at the surface at lower resolutions. With the disappearance of the underestimation of BL nitrate, one no longer sees an underestimation in aerosol water content (Figure 4.14).

At first glance, this appears to explain the observed differences in aerosol water content between the FRA10 and AA80 simulations. However, further investigation reveals a more complicated picture. To explore the impact of convective transport in more detail, the analysis focuses on a 5-day period from May 3 - 7 during which there was a large convective rainfall event confined to one side of the domain (see the top panel in Figure 4.16). Figure 4.15 shows the column aerosol water content for this period with convective transport turned on (a) and turned off (b). In the original AA80 simulation, one sees the underestimation in aerosol water content, this time confined to the lefthand side of the domain. This is to be expected as the relative humidity is much higher on this side of the domain during this time period (not shown), which also contributes to the large convective rainfall event. Once again, when convective transport is turned off, the underestimation in aerosol water largely disappears. The mean vertical profile of nitrate for this period looks nearly identical to the mean for the whole period, both with and without convective transport (also not shown).

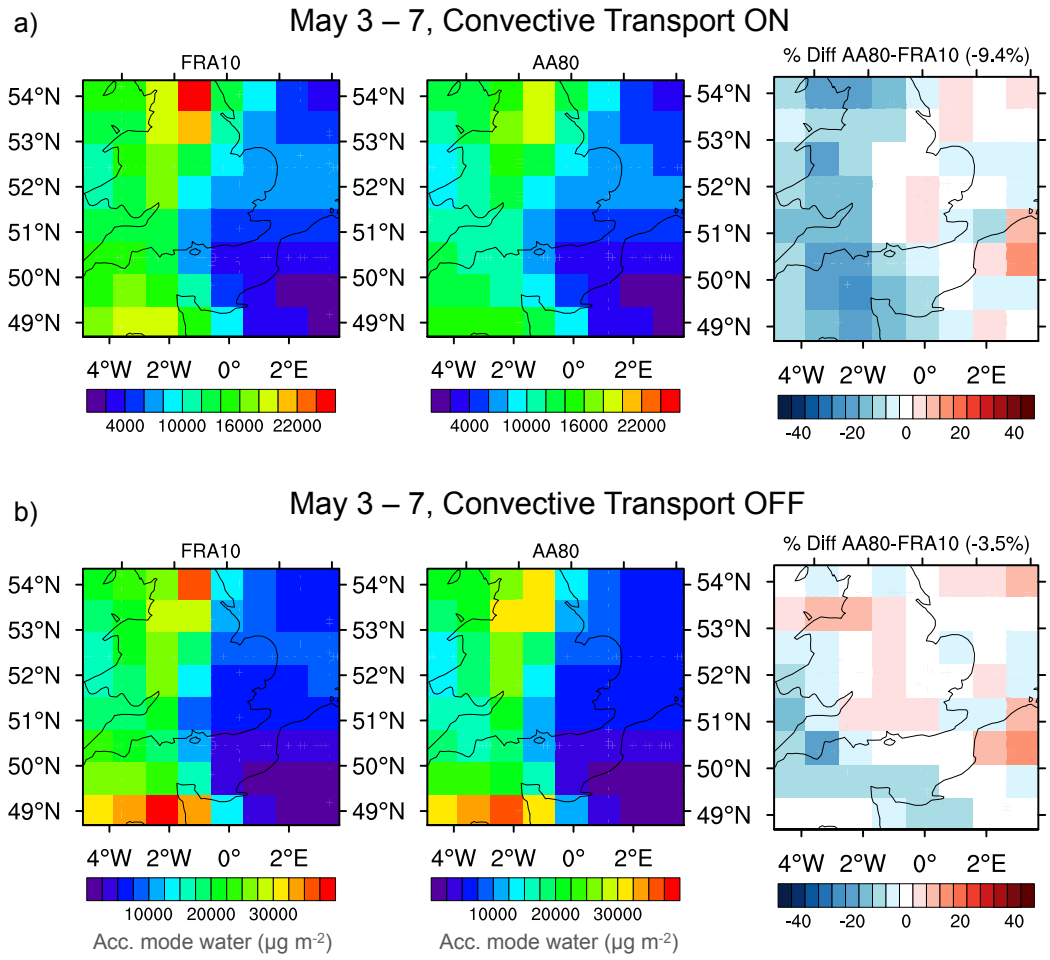

Figure 4.15: Mean spatial distribution of column amount of accumulation mode aerosol water content in $\mu g/m^2$ for the FRA10 simulation (first panel), the AA80 simulation (second panel) and the percent difference between the two (third panel) for the period of May 3 - 7, 2008, with convective transport turned on (a) and turned off (b).

However, if one examines the two sides of the domain separately, a different story develops. Figure 4.16 shows the mean vertical profile of accumulation mode nitrate, split up by area — the lefthand side where there is significant convection, and the righthand side where there is no convection. The top row shows the spatial distribution of the cumulative convective rainfall from May 3 - 7; the second row shows the vertical profiles of nitrate when convective transport is left on; and the third panel shows the same vertical profiles for the simulations where convective transport is turned off. The middle panels show that nitrate is underestimated in the BL in the AA80 simulation on both sides of the domain, even though there is very little convection on the righthand

side. Thus when convective transport is turned off, one sees the underestimation in nitrate disappear on the side of the domain where there is significant convective transport; however, the underestimation persists on the righthand side of the domain, where there is no convection.

This reveals that although convective transport likely plays a role in the underestimation of nitrate in the BL, it does not explain the full story. It is possible that a combination of convective effects, which tend to cause decreases in BL nitrate under conditions of high relative humidity, and non-linearities in the equilibrium system, which tend to cause decreases in BL nitrate under conditions of low relative humidity, lead to the observed differences in the FRA10 and AA80 simulations.

Investigating changes in nitrate: Other processes

A number of other processes were explored to evaluate their impact on observed differences in nitrate between the FRA10 and AA80. It was hypothesised that wet deposition could deplete nitrate in the BL in a similar mechanism as described for convective transport. In the high resolution run, nitrate is removed by wet deposition. Once it is removed, additional nitrate cannot be removed until concentrations are replenished either by advection or secondary production. However, in the aerosol-averaged simulation, nitrate can be instantaneously replenished over areas where it is currently raining thereby depleting more nitrate than in the high resolution run, even though the rainfall amount is the same. While this mechanism offers a potential explanation, there were very small correlations between rainfall amount and differences in nitrate in the two runs, indicating that it was likely not a strong contributor to the underestimation of BL nitrate in AA80.

Several additional simulations were performed during which specific processes were systematically turned off, including dry deposition and gas-phase chemistry. An additional AA80 simulation using high resolution emission fields was also tested. The underestimation of BL nitrate persisted in all of these runs, indicating that they had

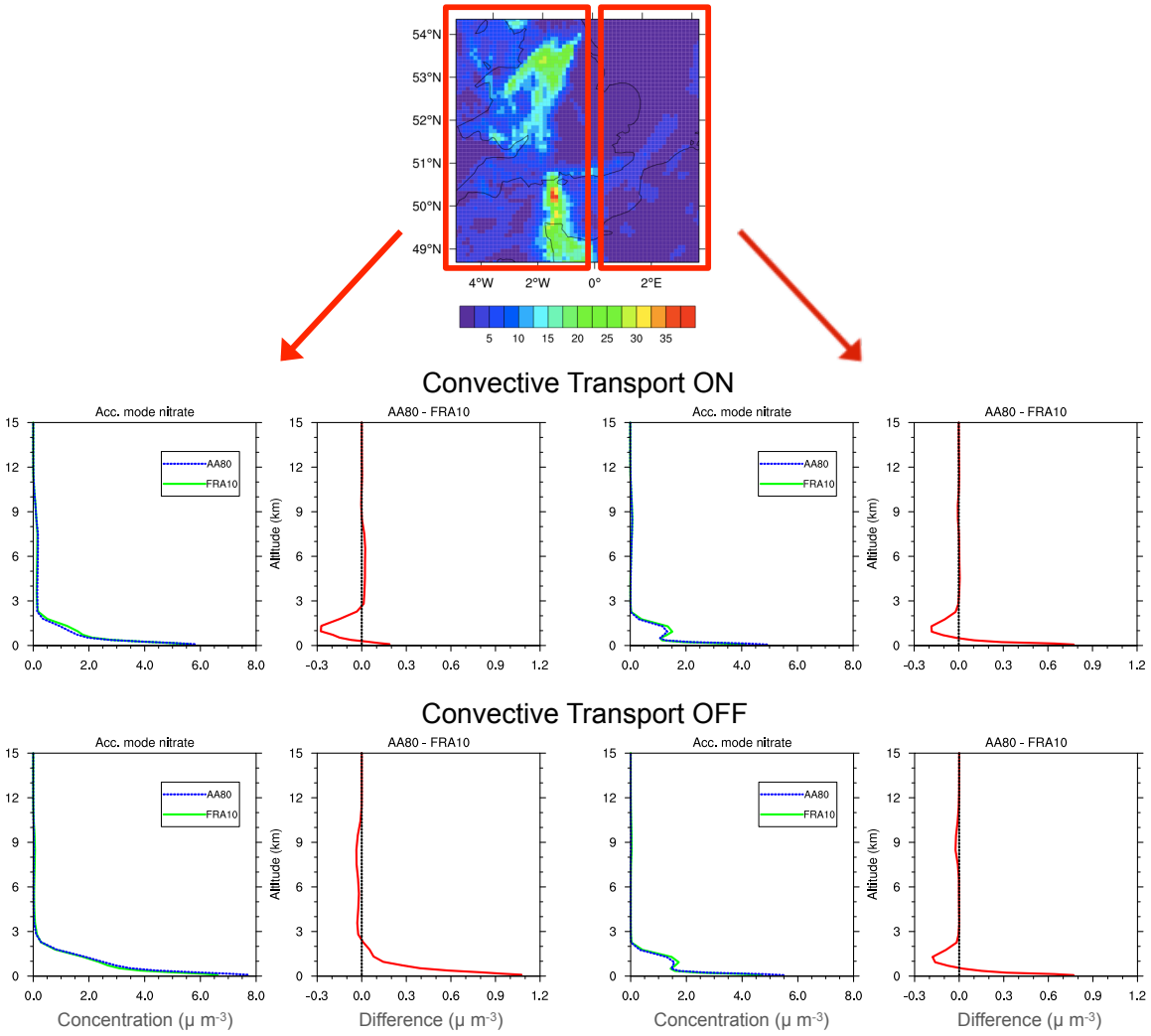

Figure 4.16: Demonstrates the impact of convective transport on the vertical profile of nitrate. The top panel shows the cumulative convective rainfall from May 3 - 7, 2008 (in mm). The middle panel shows the vertical profile of accumulation mode nitrate (in μg/m^3) for the FRA10 (green) and AA80 (blue) and the differences between them (red) for both side of the domain. The third panel shows the same, but with convective transport turned off.

little effect on the changes in nitrate between the two runs.

4.2.2 Effect of aerosol sub-grid variability on CCN

This section explores the impact of neglecting aerosol sub-grid variability on concentrations of CCN. CCN is a measure of the number of particles that can act as initial sites for condensation of water vapour at a given supersaturation that lead to the

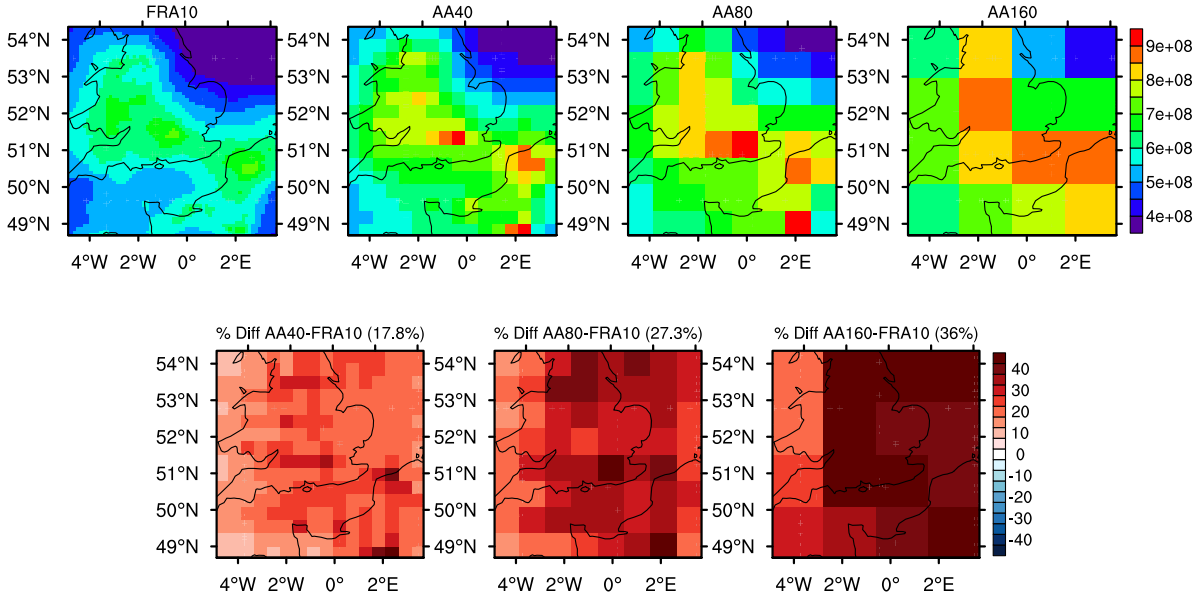

Figure 4.17: Simulated spatial distribution of CCN at 0.5% supersaturation (in #/cm^2) for the FRA10, AA40, AA80, and AA160 runs (top row). The bottom row represents the percent difference between each run and FRA10. The number in brackets in the bottom row represents the average percentage difference in the two runs. The fields represent the mean value over the evaluation period of May 3 - 31, 2008.

formation of cloud droplets and/or cloud ice particles. Figure 4.17 presents results of simulated CCN at 0.5% supersaturation for the FRA10, AA40, AA80, and AA160 simulations. At lower resolutions, the simulated CCN is overestimated with respect to the high resolution run in all regions. Compared to FRA10, the overestimation of CCN increases from an average of 17.8%, to 27.3% to 36.0% as the aerosol resolution is decreased to 40 km, 80 km, and 160 km, respectively. Again, the mechanisms causing this overestimation are investigated by exploring differences between the FRA10 and AA80 simulations.

In WRF-Chem, CCN is calculated as the sum of aerosol number concentrations from each mode, weighted by a factor that depends on supersaturation, particle size, and hygroscopicity (ability of a substance to hold water). Figure 4.18 shows the mean spatial distribution of accumulation mode number concentration for the FRA10 simulation (first column), the AA80 simulation (second column), and the percent difference between them (third column). The AA80 accumulation mode number concentration

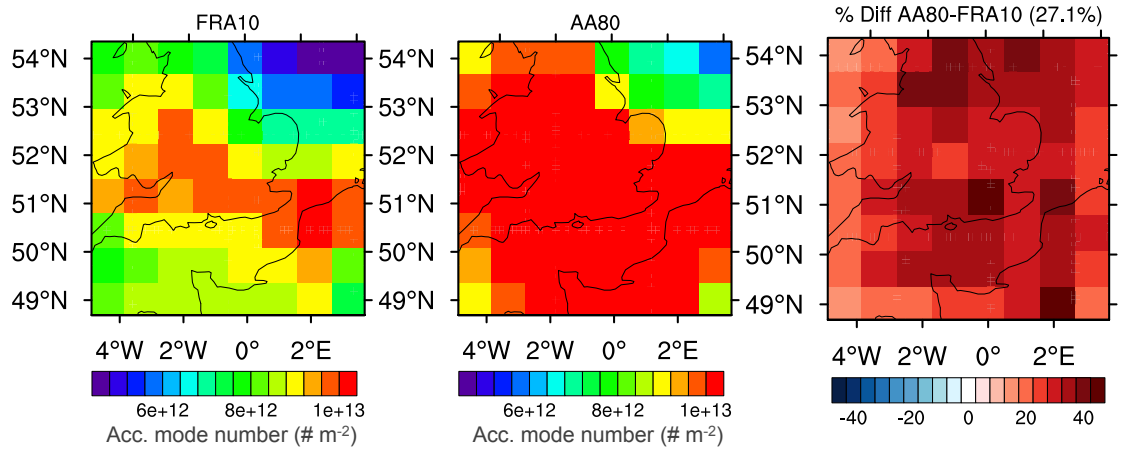

Figure 4.18: Spatial distribution of column amount of accumulation mode number concentration (#/m^2) for the FRA10 simulation coarsened to the low resolution grid (first panel), the AA80 simulation (second panel) and the percent difference between the two (third panel). The number in brackets on the third panel represents the average percentage difference in the two runs. The fields represent the mean value over the evaluation period of May 6 - 31, 2008.

is also significantly overestimated compared to the high resolution run by an average of 27.1%. One can readily see that the overestimation in CCN is nearly equivalent in magnitude and spatial distribution to the overestimation in accumulation mode number concentration, indicating that changes in CCN are dominated by changes in accumulation mode number. Pattern correlation analysis confirms that differences in CCN and accumulation mode number are indeed highly correlated with an average correlation of 0.99 (not shown). There are also small overestimations in mean Aitken mode (+10%) and coarse mode (+3%) number concentrations in AA80; however, at 0.5% supersaturation, one would expect accumulation mode number to be the dominant contributor to CCN. When the supersaturation is increased to 3%, the overestimation in CCN decreases to 17.2%, indicating a larger contribution from Aitken mode aerosols where the discrepancies between the high and low resolution runs are smaller.

The marked increase in CCN and accumulation mode number concentration is also apparent in their vertical profiles, shown in Figure 4.19. The increase in both CCN and accumulation mode number concentration exists at all altitudes from 0 to 12 km,

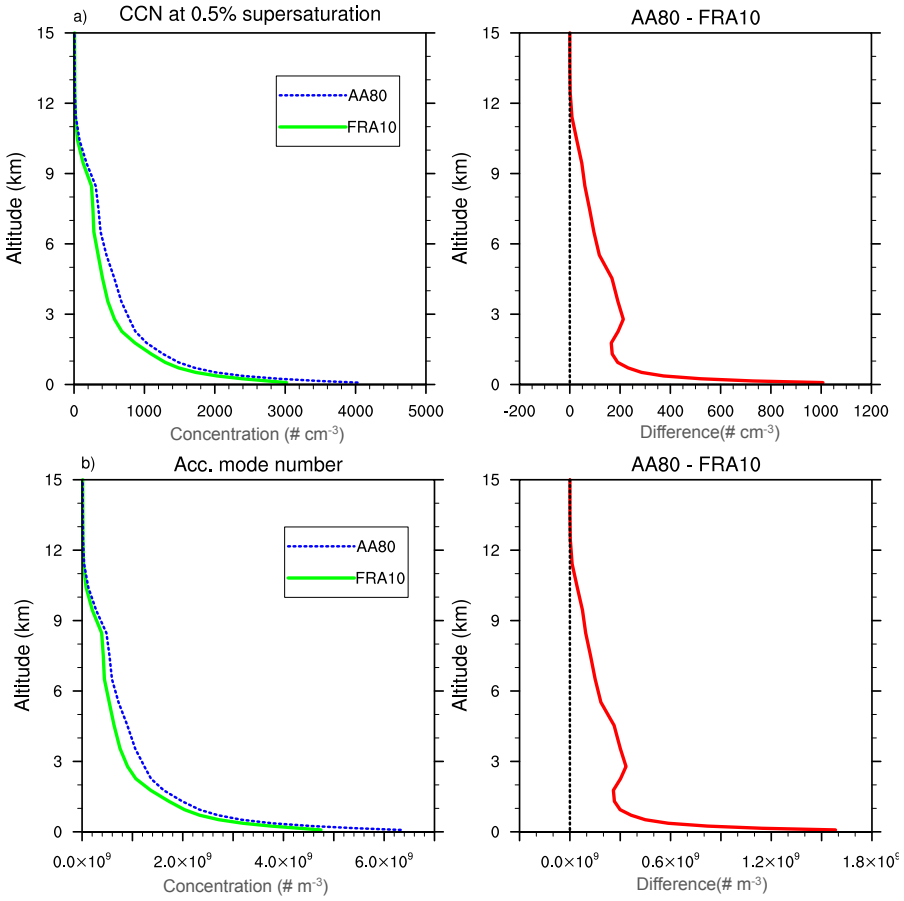

Figure 4.19: Vertical profiles for the FRA10 and AA80 simulations and the differences between them of CCN at 0.5% supersaturation (a, in #/cm^3), and accumulation mode number concentration (b, in #/m^3). FRA10 simulations are in green, the AA80 in dashed blue and the differences in red. The fields represent the mean value over the evaluation period of May 3 - 31, 2008.

with the largest increase at the surface.

At altitudes above 2 km, the aerosol number concentration is significantly affected by the rate of new particle production by nucleation. In the AA80 simulation, the nucleation rate is 25% higher in the upper troposphere than in the FRA10 simulation. A higher nucleation rate results in a higher concentration of Aitken mode particles in the upper troposphere, which leads to higher accumulation mode number concentration as there are more particles available to grow into the larger mode. These results are highlighted in Figure 4.20, which shows the increase in nucleation rate and the corresponding increase in Aitken mode number concentrations above the surface,

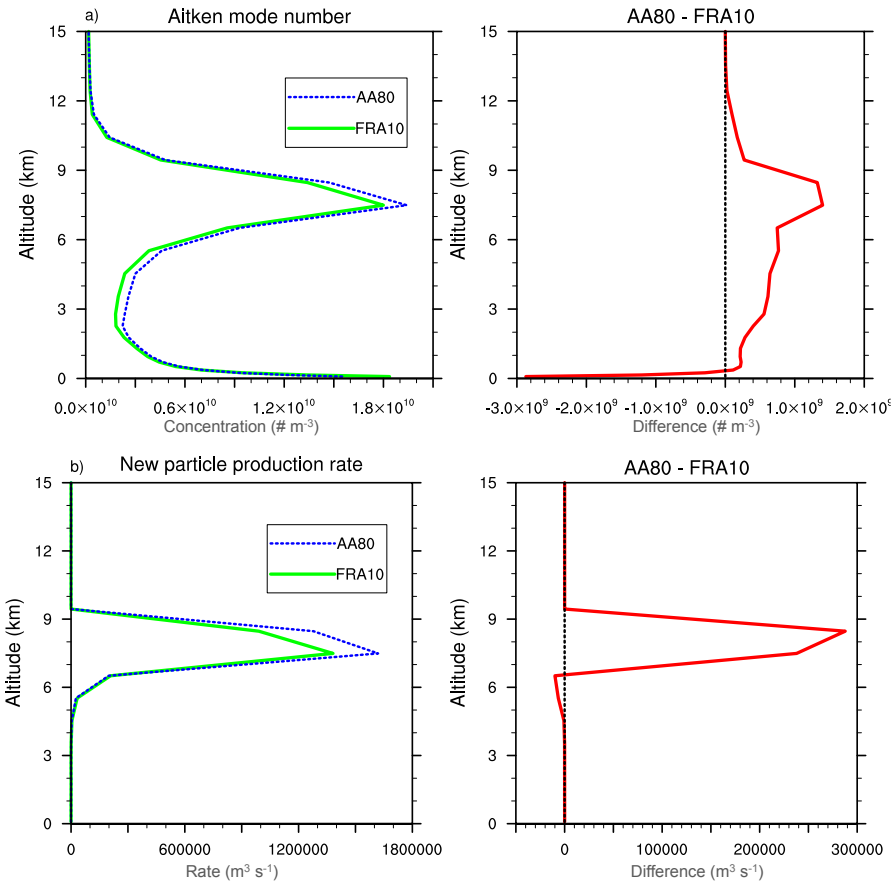

Figure 4.20: Vertical profiles for the FRA10 and AA80 simulations and the differences between them of Aitken mode number concentration (a, in #/m^3), and new particle production rate (b, in m^3/s). FRA10 simulations are in green, the AA80 in dashed blue and the differences in red. The fields represent the mean value over the evaluation period of May 3 - 31, 2008.

particularly between 6 and 9 km where the difference in nucleation rate is greatest.

The standard WRF-Chem nucleation scheme was used in these simulations. This scheme is a simple parameterisation of homogeneous nucleation in the sulphuric acid-water system [*Kulmala et al.*, 1998]. The nucleation rate, J, is parameterised by:

$$J = e^{\chi} \tag{4.1}$$

$$\chi = c_1 N_{sulph} - c_2 \frac{N_{sulph}}{T} - \frac{c_3}{T} - c_4 N_{sulph} RH + c_5 \frac{X_{al}}{T} - c_6 \frac{X_{al}\delta}{RH} \tag{4.2}$$

where $c_{1,2...}$ represents empirically determined constants, N_{sulph} is the number of

moles of sulphuric acid vapour, T is temperature, RH is relative humidity, X_{al} is the mole fraction of sulphuric acid in the critical nucleus (a parameter that depends on moles of sulphuric acid vapour, temperature, relative humidity and relative acidity), and δ is a temperature-dependent parameter. Because the meteorological parameters are identical in the full resolution and the aerosol averaged simulations, the non-linear dependence of the nucleation rate on sulphuric acid vapour concentration must be the source of the discrepancy between the FRA10 and AA80 simulations.

The sulphuric acid vapour concentration, $[SA]$, is determined by its chemical production (or source term), and loss due to nucleation and condensation. The change in sulphuric acid vapour at each time step can be represented by the following expression [**?**]:

$$\frac{d[SA]}{dt} = k \cdot [OH][SO_2] - J \cdot n^* - CS \tag{4.3}$$

where k is the chemical rate constant, n^* is the number of sulphuric acid molecules in the critical cluster, and CS is the condensational sink term. Sulphuric acid vapour is produced by the reaction of the hydroxyl radical (OH) and sulphur dioxide gas (SO_2). Inspection of the changes in sulphuric acid vapour between the FRA10 and AA80 runs shows very little difference; however, the concentration of OH is overestimated in the AA80 simulation by 15 - 20% in the upper troposphere, which one can see in its vertical profiles in Figure 4.21. The impact of this overestimation in OH on sulphuric acid and, ultimately, the nucleation rate can be observed in Figure 4.22, which shows the concentration of OH (a), the sulphuric acid production tendency (b), and the nucleation rate (c) at 7.5 km — the altitude at which the nucleation rate is greatest. One can see the similarities in the spatial patterns of all three parameters, with the highest values occurring over land, particularly over the UK. All three parameters also show large overestimations in the AA80 simulation, with particularly similar spatial differences in the sulphuric acid production tendency and the nucleation rate. It is therefore likely that, even though there are very little differences in the overall

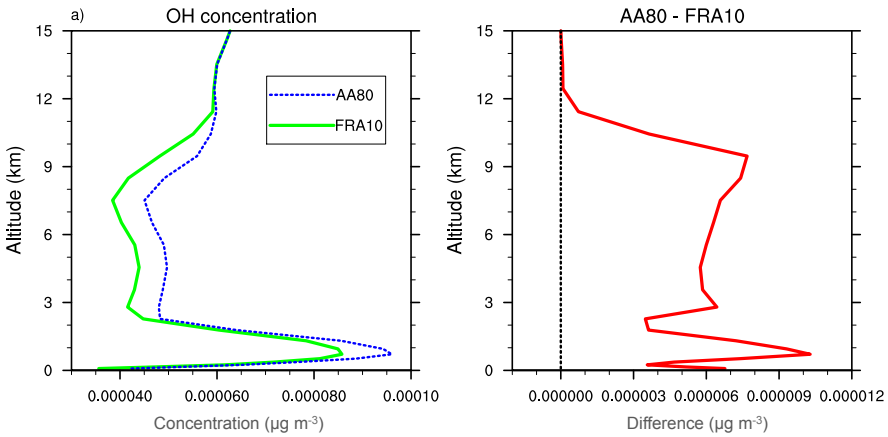

Figure 4.21: Vertical profiles of OH (in $\mu g/m^3$) for the FRA10 and AA80 simulations and the differences between them. FRA10 simulations are in green, the AA80 in dashed blue and the differences in red. The fields represent the mean value over the evaluation period of May 3 - 31, 2008.

concentrations of sulphuric acid between the two runs, the overestimation in OH leads to an increased rate of oxidation of sulphur dioxide, causing an increase in the chemical production tendency of sulphuric acid in the AA80 run. The excess sulphuric acid produced is then available for new particle production in the upper troposphere.

Although OH chemistry in the upper troposphere involves a myriad of complex reactions, the concentration of OH has been found to largely depend on its primary production rate from ozone photolysis [*Jaeglé et al.*, 2001]. Ozone production is known to be dependent on its precursor concentrations in a non-linear manner, particularly NO_x (NO + NO_2). Previous work has shown that ozone production is relatively inefficient at high concentrations of NO_x found in near-source areas compared with low concentrations typical of remote regions [*Sillman et al.*, 1990]. This non-linearity can therefore have a large impact on model-simulated ozone concentrations due to the artificial mixing of its precursor gases over large grid areas, resulting in excessive production of ozone and, consequently, hydroxide concentrations [*Esler et al.*, 2004]. In the AA80 simulation, the artificial dilution of aerosols and trace gases is likely the cause of the higher rate of ozone production, which is up to 3.5 times greater than in the FRA10 simulation (not shown).

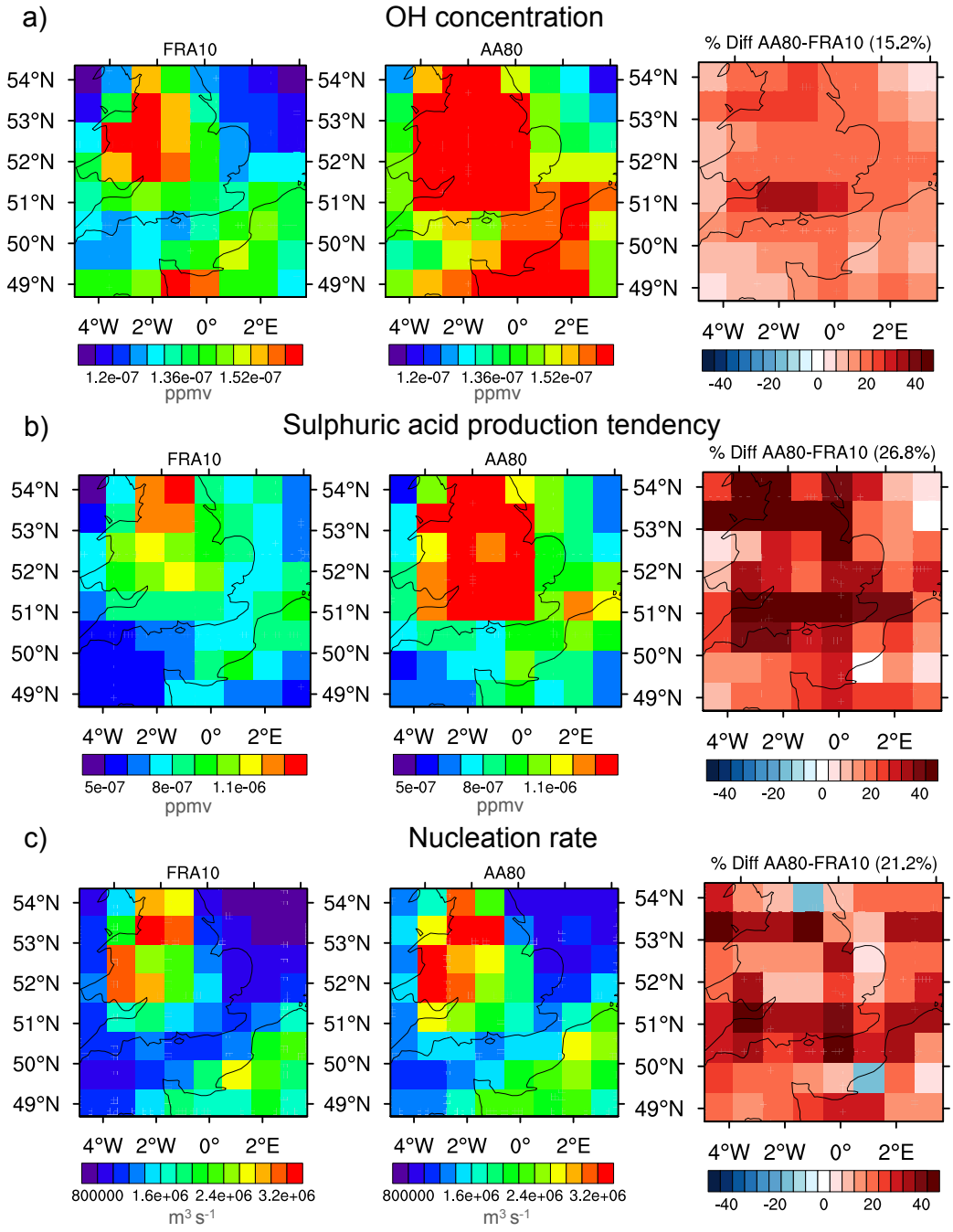

Figure 4.22: Spatial distribution of OH concentration in the upper troposphere (model level 15) in ppmv (a) for the FRA10 simulation coarsened to the low resolution grid (first panel), the AA80 simulation (second panel) and the percent difference between the two (third panel). Figures (b) and (c) show the same for sulphuric acid production tendency (in ppmv) and nucleation rate (in m^3/s), respectively. The number in brackets on the third panel represents the average percentage difference in the two runs. The fields represent the mean value over the evaluation period of May 3 - 31, 2008.

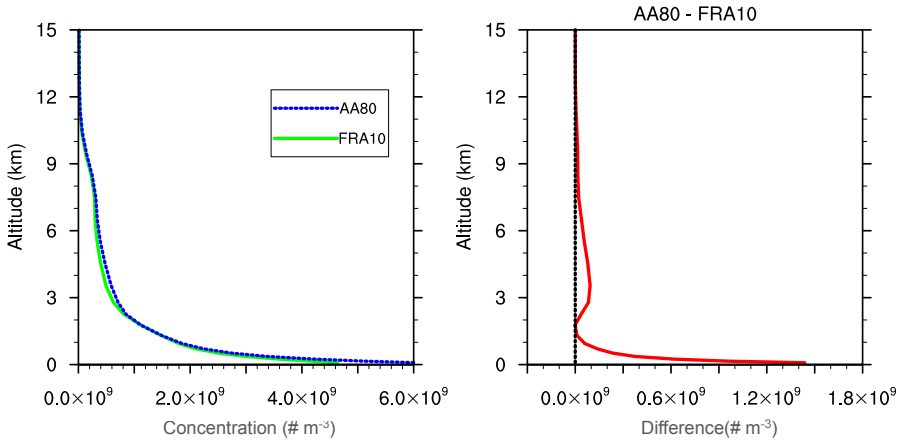

Figure 4.23: Vertical profile of accumulation mode number concentration (in $\#/m^3$) from the FRA10 and altered AA80 simulations and the differences between. The altered AA80 simulation averages only the aerosol fields, instead of both gas and aerosol fields. The profiles represent the mean value over the evaluation period of May 3 - 31, 2008.

To test this hypothesis, an alternative AA80 simulation was performed where only the aerosol fields were averaged over a lower resolution grid, and the gaseous fields remained on the original high resolution grid. In this case, the differences in ozone and OH concentrations were essentially zero, leading to a near zero difference in nucleation rate. As a result, the differences in accumulation mode number concentration at altitudes above the surface largely disappear. Figure 4.23 shows the vertical profile of accumulation mode number concentration from FRA10 and the alternative AA80 simulation with high resolution gas fields. One can see that the overestimation observed in the original AA80 run at altitudes greater than 2 km is significantly reduced. However, surface accumulation mode number concentrations are still overestimated, which cannot be explained by the increase in nucleation rate. Accounting for the overestimation in the rate of nucleation, the overall bias reduces from +27.3% to +10.3%.

Convective transport also plays a role in the overestimation due to nucleation. This mechanism lofts gaseous species to altitudes above the boundary layer where ozone and hydroxide production is more efficient and where their lifetimes are longer. Turning off convective transport of aerosol and gaseous species produces a similar result to

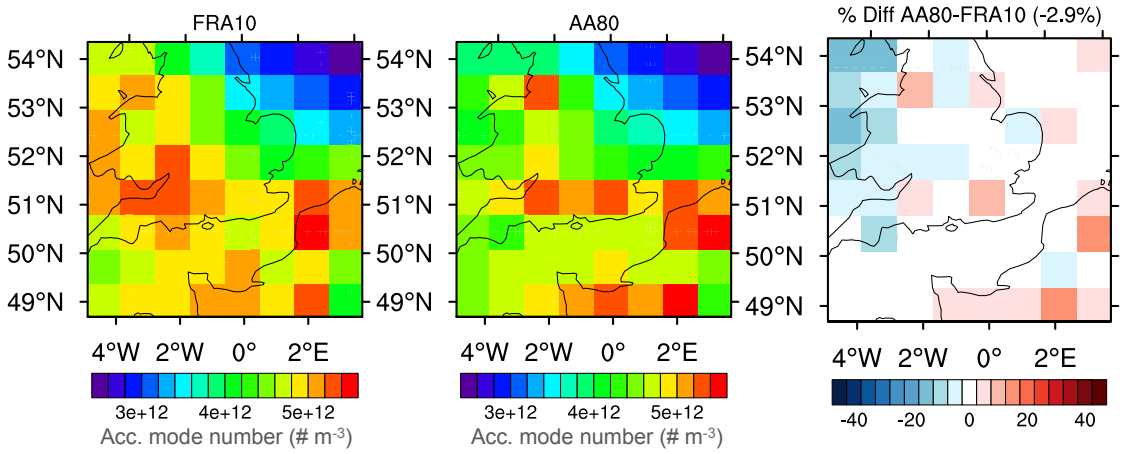

Figure 4.24: Spatial distribution of column amount of accumulation mode number concentration ($\#/m^2$) for the FRA10 simulation coarsened to the low resolution grid (first panel), the AA80 simulation (second panel) and the percent difference between the two (third panel). In both simulations nucleation and dry deposition have been switched off. The number in brackets on the third panel represents the average percentage difference in the two runs. The fields represent the mean value over the evaluation period of May 3 - 31, 2008.

the altered AA80 simulation, reducing the overestimation of CCN from +27.3% to +10.7%.

In summary, dilution of aerosol and gaseous fields over an 80 km grid results in an increase in ozone production, which is lofted to higher altitudes and leads to higher concentrations of OH in the upper troposphere. Enhanced OH concentrations result in faster oxidation of SO_2, producing higher concentrations of sulphuric acid, which promotes the formation of new aerosol particles in the upper troposphere. Higher number concentrations at altitudes above 2 km lead to increased CCN. This mechanism accounts for a significant portion of the total bias in CCN.

The overestimation in accumulation mode number at the surface is related to dry deposition processes. When both nucleation and aerosol/gas dry deposition processes are turned off, the difference between FRA10 and AA80 virtually disappears, as shown in Figure 4.24. The likely mechanism behind the overestimation due to dry deposition is that by simulating aerosols over a lower resolution grid than the underlying terrain, aerosols in coastal regions that are normally deposited over land are being spread

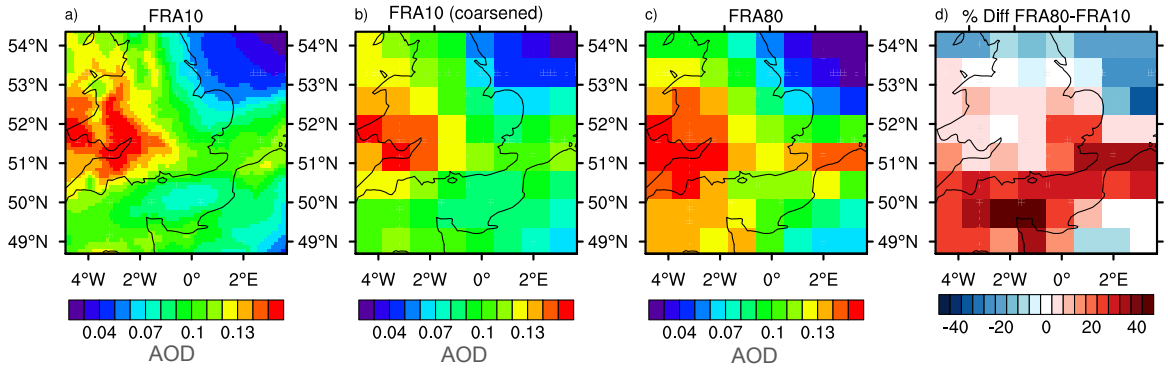

Figure 4.25: Demonstrates a traditional comparison of the spatial distribution of AOD at two different model resolutions. AOD is simulated at 10 km resolution (a) and 80 km resolution (c). The AOD fields from the higher resolution run are coarsened to the low resolution grid (b) before taking the percent difference between the two runs (d)

over the ocean where the deposition velocities are set to zero, causing a build up of aerosol over oceans and other bodies of water. Examining the spatial distribution of the differences in accumulation mode number at the surface shows a strong overestimation over the ocean areas and the English Channel. The nature of this particular domain may amplify this affect due to the extensive coastal regions within the domain. The magnitude of this dry depositional effect on a global scale is unclear and requires further investigation.

4.2.3 Full resolution comparisons

As discussed in the introduction, a common method for investigating the impact of sub-grid variability on model predictions of the aerosol effect on climate is to vary a model's resolution and analyse the resulting effect this has on aerosol fields. While this method can provide some insight into the differences in model behaviour at different grid spacings, it is limited in its ability to pinpoint the processes that contribute to these differences. This makes it difficult for modellers to determine which processes benefit the most from increased resolution.

This difficulty is highlighted by comparing results from the FRA10 and FRA80

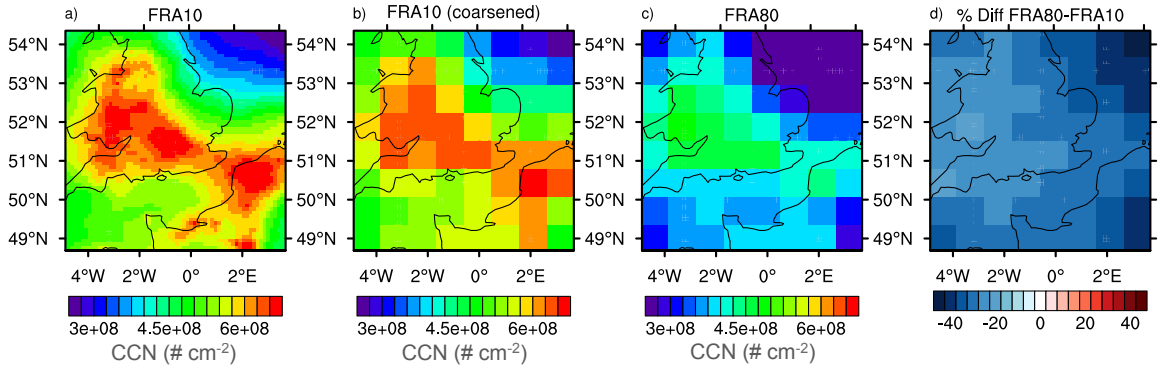

Figure 4.26: Demonstrates a traditional comparison of the spatial distribution of CCN at 0.5% supersaturation (in #/cm^2) at two different model resolutions. CCN is simulated at 10 km resolution (a) and 80 km resolution (c). The CCN fields from the higher resolution run are coarsened to the low resolution grid (b) before taking the percent difference between the two runs (d)

simulations, where the full resolution of the model has been changed from 10 km to 80 km. Figures 4.25 and 4.26 show mean AOD and CCN fields for each of these runs, respectively.

Figure 4.25a shows AOD at 10 km resolution and Figure 4.25c at 80 km. The AOD fields from the higher resolution run are coarsened to the low resolution grid (Figure 4.25b) before taking the percent difference between the two runs (Figure 4.25d). The changes in AOD due to varying the full model resolution are drastically different from the changes in AOD due to varying the resolution of the aerosols only.

Decreasing the model resolution from 10 km to 80 km results in a 20 – 40% underestimation of AOD over the English channel region, and a 20% overestimation in AOD in the northern regions of the domain. Further investigation reveals that the differences in AOD are again linked to changes in aerosol water content; however, the underlying mechanisms causing the changes in aerosol water are much less clear. Not only are there changes in aerosol composition, as seen in the "aerosol averaged" comparisons, there are also large changes in average daily relative humidity and temperature, which further complicate the gas-aerosol thermodynamic equilibrium. Again, nitrate seems to play a more important role in the changes in aerosol water content compared to

sulphate; however, the differences in nitrate could be due not only to changes in aerosol and gaseous variability but also in relative humidity and temperature within the gas-aerosol equilibrium, as well as meteorological processes external to the equilibrium system, like rainfall and advection.

In fact, the amount of convective rainfall is more than 50% less in the FRA80 simulation compared to FRA10. Since wet deposition is an important aerosol removal mechanism, as is convective transport (shown in the previous sections), this decrease in rainfall likely masks many of the changes we observed due to aerosol variability.

Moving on to CCN, again the changes in CCN due to varying the full model resolution are starkly different from the changes due to varying aerosol resolution only (Figure 4.26). Whereas CCN was largely overestimated in the AA80 simulation, CCN is now significantly underestimated (on average -33.0%) in all regions of the FRA80 domain. While this underestimation is also linked to changes in accumulation mode number concentration as seen in the "aerosol averaged" simulations, the FRA80 simulation shows an underestimation in the nucleation rate of -24.3% at its peak. In the FRA80, there is on average 54.7% less convective rainfall, indicating that convection is significantly weakened in the low resolution run. While a decrease in rainfall could act to increase aerosol concentrations, a weakening of convective transport could significantly affect gas chemistry in the upper troposphere, thereby altering the nucleation rate and secondary formation of aerosols. These competing interactions, along with other changes in meteorology, make it difficult to gain an understanding of the processes governing the simulated underestimation in CCN in FRA80.

Additionally, while I was able to offer possible explanations to the changes seen in AOD and CCN in the FRA80 simulation, the insight to these changes came from the previous analysis of the AA80 simulation, further highlighting the usefulness of isolating the effect of aerosol variability.

4.3 Summary and discussion

This chapter investigated the impact of neglecting aerosol sub-grid variability on two important aerosol parameters: aerosol optical depth and cloud condensation nuclei, which serve as proxies for aerosol-radiation and aerosol-cloud interactions, respectively. It introduced a novel technique to allow one to isolate the effect of aerosol variability from other sources of model variability by varying the resolution of aerosol and trace gas fields while maintaining a constant resolution in the rest of the model. The technique involved averaging the high resolution aerosol and trace gas fields over a lower resolution grid and passing these averaged fields onto the rest of the high resolution model. The aerosol resolution was varied to 40 km, 80 km, and 160 km (AA40, AA80, and AA160) and compared to a baseline high resolution run at 10 km (FRA10).

Decreasing the resolution of the aerosol fields resulted in an underestimation of AOD by an average 10% (for AA40) to 16% (for AA160) over the whole domain, with some regions showing decreases of up to 30% in AA160. The changes in AOD were linked to changes in accumulation mode aerosol water content, which is determined by the sulphate-nitrate-ammonium gas/particle partitioning equilibrium. The aerosol equilibrium concentrations depend on relative humidity, temperature and the concentrations of their gaseous precursors - sulphuric acid, nitric acid, and ammonia. While relative humidity and temperature were identical in both the high resolution and aerosol averaged simulations, the aerosol and gaseous concentrations showed some differences. Most notably, nitrate aerosol concentrations in the boundary layer were approximately 20% less in the AA80 simulation compared to the FRA10. Water uptake by nitrate is most efficient in the boundary layer, where relative humidity is high and temperature is low; therefore, this underestimation of nitrate in the aerosol averaged runs lead to an underestimation of aerosol water. The underestimation of nitrate in the boundary layer was likely due to a combination of the response of the non-linear equilibrium system to changes in aerosol and gaseous variability and of

convective transport, which removes more nitrate in the low resolution run.

These results highlight the important role of nitrate in aerosol radiative effects. Measurements indicate that the mass fraction of nitrate can exceed that of sulphate in urban areas in Western Europe [*Brink et al.*, 1996]. Modelling studies have also shown that nitrate will be an increasingly important contributor to anthropogenic radiative forcing in the future as sulphate concentrations continue to decrease due to stricter regulations. *Adams et al.* [2001] predict present-day forcing of sulphate to decline from -0.95 W/m^2 to -0.85 W/m^2 by 2100, whereas forcing due to nitrate could increase from -0.19 W/m^2 to -1.28 W/^{2} using a future emissions scenario. Nitrate has also been shown to boost the scattering efficiency of sulphate and organic matter, and its gaseous precursor nitric acid has been shown to have a significant effect on cloud forcing through condensation of nitric acid gas onto growing droplets [*Xu and Penner*, 2012].

Over the past decade, GCMs have been incorporating nitrate aerosol in direct radiative forcing calculations. In the AeroCom Phase II direct radiative forcing study, eight of the sixteen models currently use an equilibrium parameterisation for nitrate and aerosol water uptake, and two more are in the process of incorporating them into their models [*Myhre et al.*, 2013b]. The results presented in this chapter indicate that accurate representation of aerosol radiative effects requires a realistic model of water uptake by aerosols, including sub-grid spatial variation in aerosol chemical composition.

It is interesting that variability in aerosol composition was found to play an important role in water uptake by aerosols even when relative humidity is constant. Several previous studies have shown that GCMs underestimate AOD due to inability to capture sub-grid variability of RH. [*Haywood et al.*, 1997] found that under conditions of high RH (90-100% range) and substantial sub-grid variability of RH and clouds, GCMs underestimate direct radiative forcing of aerosols by 73% in clear-sky conditions and by 60% in cloudy conditions. *Bian et al.* [2009] was able to isolate the effect

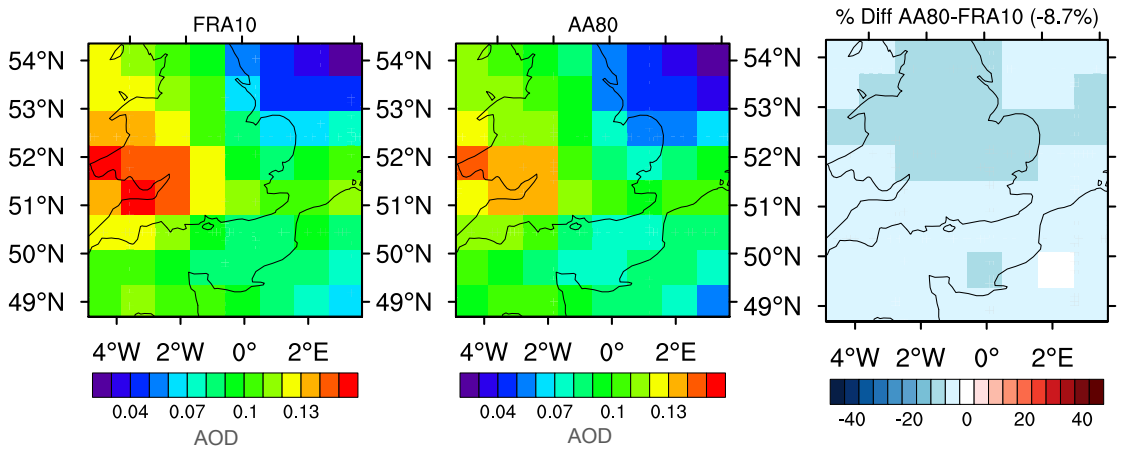

Figure 4.27: Demonstrates the effect of RH variability on AOD at 600 nm. The first panel shows the spatial distribution of AOD coarsened to the low resolution grid for the high resolution FRA10 simulation, the second panel shows AOD with low resolution RH (80 km grid), and the third panel shows the percent difference between them.

of RH variability on AOD by varying the resolution of RH fields while maintaining a constant resolution in all other model fields. They found that the globally averaged AOD was 11% higher when the resolution of RH was doubled from 2° x 2.5° to 1° x 1.5°. One can perform a similar comparison to *Bian et al.* [2009]'s work using the technique presented in this chapter. Instead of averaging aerosol and gaseous fields over a lower resolution grid, aerosols and other meteorological fields can be held at a constant resolution while relative humidity is averaged over the lower resolution grid. This allows for the comparison of the relative impact of RH variability on AOD to the results in Section 4.2.1, which discussed the impact of aerosol variability on AOD. Figure 4.27 shows the results of this comparison. AOD is underestimated by 8.7% when RH is coarsened from 10 km to 80 km. This is similar in magnitude to the results from *Bian et al.* [2009], although both of their high and low resolution simulations were at much lower resolutions than the simulations presented here. These results also show that the impact of RH variability is smaller than the impact of aerosol variability on AOD.

While the variability in relative humidity is certainly an important factor in determining aerosol radiative forcing, this study shows that even when using identical

resolution relative humidity, AOD is still underestimated at GCM resolutions. These results suggest that at least some of this underestimation in AOD in previous studies may be due to the impact of sub-grid variability of aerosol composition on water uptake as well as variability in RH. Similar results have been shown with modelling studies over the Netherlands, whose environment is characterised by its high concentrations of ammonia and nitric acid due to agricultural activity. *Roelofs et al.* [2010] compared global climate modelling results to observations over the Netherlands and found that AOD appeared to be strongly influenced by the diurnal cycle of RH in the lower boundary layer, which was further enhanced by uptake of nitric acid and ammonia by aerosol water. *Derksen et al.* [2011] used a 1D column model with detailed sulphate-nitrate equilibrium chemistry and found that the daily evolution of aerosol ammonium nitrate actually influenced the variability of AOD more than the daily variability of RH; however, this simulation was only carried out over one day.

The effect of neglecting aerosol variability on CCN was also presented in this chapter. Decreasing the resolution of aerosol and gaseous fields resulted in an overestimation of CCN by an average of 18% (for AA40) to 36% (for AA160) over the entire domain. The changes in CCN were linked to changes in accumulation mode number concentration, which was also overestimated by a similar degree. At the surface, the overestimation of CCN was related to differences in dry deposition processes over land and ocean when averaging aerosols over a lower resolution than the underlying terrain. At higher altitudes, the increase in accumulation mode number was influenced by enhanced trace gas chemistry. The artificial dilution of trace gases resulted in an increase in the production of ozone, leading to increased OH, which resulted in higher concentrations of sulphuric acid vapour. With more sulphuric acid vapour available for nucleation, the number of Aitken mode particles increased at high altitudes, leading to an increase in accumulation mode number. Convective transport again played an important role in the observed differences in CCN by lofting the trace gases into the troposphere where the gases have longer lifetimes and their reactions are more efficient.

Without convective transport, the overestimation of CCN due to gas chemistry does not occur.

Several previous studies have shown that ozone production is overestimated at lower model resolutions. *Esler et al.* [2004] explored the impact of averaging relatively long-lived precursor species such as ozone, NO_x, carbon monoxide and water vapour over different spatial scales and found that low resolution experiments had significantly higher ozone production rates and OH concentrations than high resolution experiments. *Wild and Prather* [2006] performed a similar experiment and found that the overestimation in ozone is still large at 120 km. This is due to the fact that ozone production depends non-linearly on its gaseous precursor concentrations, and most of the production occurs on short time scales close to regions with high precursor emissions. Artificially diluting ozone and its precursor gases over a model grid box effectively increases the time scale over which its chemical production occurs. Also, artificial dilution of gas fields acts to exaggerate the importance of convection, enhancing the export of longer-lived gases to the mid- and upper troposphere where ozone production is more efficient [*Wild and Prather*, 2006].

It is clear that mixing of gases at global model grid-scales can result in large discrepancies in simulated and observed gaseous concentrations. And while it has been well-documented that gas-phase chemistry is dependent on model resolution, this study demonstrates that these gas-phase discrepancies can have a significant impact on aerosol parameters through secondary aerosol formation.

The results also showed that as the aerosol resolution was increased, the biases in both AOD and CCN decreased compared to the high resolution run. The improvement was better when the aerosol resolution was increased from 80 to 40 km than when it was increased from 160 to 80 km, implying that the added value of increasing resolution is greater at higher resolutions. This provides further motivation to continue to increase the computational capabilities of global climate models by increasing model resolution.

Comparisons were also made between the full resolution run at 10 km (FRA10)

and the full resolution run at 80 km (FRA80) in order to highlight the difficulty in identifying the mechanisms that cause differences in aerosol parameters at different model resolutions. The changes in AOD and CCN between these two runs were different in both sign and magnitude from the changes in AOD and CCN in the "aerosol averaged" runs where only the aerosol resolution was varied. In these comparisons, it was not feasible to determine if discrepancies between the high and low resolution simulations were due to neglecting sub-grid variability of meteorological, dynamical, or aerosol processes. Large differences in meteorological parameters such as convective rainfall and relative humidity could be masking effects caused by neglecting aerosol variability.

In conclusion, this chapter demonstrates that aerosol variability existing at sub-grid scales can have a significant impact on important aerosol parameters, such as AOD and CCN. Processes most affected by neglecting aerosol sub-grid variability were gas-phase chemistry and aerosol uptake of water through the aerosol/gas equilibrium reactions. The inherent non-linearities in these processes resulted in large changes when aerosol and gaseous species were artificially mixed over large spatial scales. These changes in aerosol and gas concentrations were exaggerated by convective transport, which transported these altered concentrations to altitudes where their effect was more pronounced. Future aerosol model development should focus on accounting for the effect of sub-grid variability on these processes at global scales in order to more accurately predict the aerosol effect on climate.

Chapter 5

Conclusions and Future Work

Aerosols have a significant effect on the global radiation budget through their interactions with radiation and clouds. However, estimates of total aerosol forcing are highly uncertain and are the dominant source of uncertainty in current estimates of total anthropogenic effect on climate (see *Boucher et al.* [2013]). A major cause of this uncertainty is the high degree of spatial and temporal variability of tropospheric aerosol properties and the processes that affect their lifetime.

Prediction of the aerosol effect on climate depends on the ability of three-dimensional numerical models to accurately estimate aerosol concentrations and their microphysical properties. However, a fundamental limitation of traditional grid-based models is their inability to capture variability on scales smaller than a model grid box, which typically ranges from 100 – 400 km for climate simulations. Past research has shown that aerosol properties display significant variability on scales smaller than these grid-boxes, which leads to discrepancies between observations and aerosol modelling schemes.

Observed variability in aerosol distribution and composition is rarely the result of one process; it is a complex interaction between meteorological and aerosol processes that contribute to aerosol variability on different scales. It is essential to determine the relative contribution of different processes to aerosol variability in order to quantify the important scales on which this variability occurs and reduce errors in aerosol

modelling.

This thesis uses a synthesis of aerosol observations, global climate model data, and a new aerosol modelling technique implemented within a regional-scale model to quantify the important scales of aerosol variability and the extent to which different sub-grid scale processes contribute to discrepancies in aerosol modelling. This work sheds new light on the impact of aerosol variability in climate modelling and provides direction for future model development on the handling of aerosol processes most affected by aerosol variability.

5.1 Conclusions

This thesis sought to address four research questions, as outlined in the introductory chapter. The contribution of this thesis to the answers of each of these questions is summarised below.

What are the important scales of variability of aerosols?

Previous research has documented that aerosol variability exists on a multitude of spatial scales, from micro to synoptic scale. Model studies have also shown that failing to resolve aerosol variability can introduce uncertainties and errors in predictions of aerosol-climate interactions. However, there is still a lack of understanding in terms of which scales are important to resolve in order to accurately describe the aerosol effect on climate. What scales are representative of important aerosol features in the atmosphere? How does this variability relate to total measured aerosol mass? Chapter 2 addressed these questions by quantifying the scales of black carbon (BC) aerosol plumes measured by the HIPPO aircraft campaign and comparing these plume scales to overall BC variability.

The HIPPO campaign flew pole-to-pole over the Pacific Ocean, spanning thousands of kilometres with nearly continuous vertical profiling. This dataset provided a unique opportunity to quantify black carbon plume scales over a large region of the globe

during different seasons. To quantify plume scales, a plume-detection algorithm was developed, which defined a plume as an occurrence of elevated mass mixing ratio above a background level. Because the HIPPO campaign consists of a series of slant vertical profiles, the plume scale in this analysis is a 'scale along the (slanted) flight track' rather than a horizontal or vertical scale. A total of 208 plumes were identified during the campaign. These plumes represent a large portion (71%) of the total mass of BC measured in the free troposphere during the campaign, confirming that these plumes are important features of BC in the atmosphere.

Statistical analysis of the observed plume characteristics showed that the median plume scale is 98 km. A plume compositing technique, which reflects the high number of small-scale plumes, quantified a typical BC plume scale of approximately 65 km. From these two analyses, it was concluded that a typical BC plume scale in the remote Pacific is in the range of 65 – 100 km. Autocorrelation analysis reveals that most of BC's variability occurs on scales smaller than 80 – 160 km. This range of total BC variability overlaps considerably with the range of BC plume scales, suggesting that a large portion of the BC variability can be accounted for by these plume structures.

Because BC plumes represent a large portion of total measured BC mass and typically exist on scales of 65 – 100 km, capturing the scales of these important structures is a key step in accurately describing BC's effect on climate.

How does a GCM's inability to resolve sub-grid scale variability affect model predictions of aerosols?

Coarse grid sizes used by global climate models (GCMs) are insufficient for adequately capturing aerosol variability and can result in significant discrepancies between simulated and measured aerosol properties. This thesis seeks to quantify how this inability to resolve sub-grid scale variability affects simulations of important aerosol features. Chapter 3 addressed this problem by comparing the scales of the observed HIPPO plumes to those simulated by the global model ECHAM-HAM at three different reso-

lutions: low, baseline, and high. These simulations used a flight track simulator so that model output was interpolated to the HIPPO flight track, allowing for a point-by-point comparison between observations and models.

The along-flight-track plume analysis showed that GCMs largely overestimate the scales of observed along-flight-track plumes. The median plume scale from the low resolution simulation was 2.3 times greater than the median scale of the observed plumes. Increasing the model resolution showed improvements in the representation of plume scales; however, the highest resolution simulation still overestimated the scales of BC plumes by 64%. Further analysis suggested that, due to the slanted nature of the flight track, the scales of the along-flight-track plumes may be dictated by their vertical extent and that improvement between modelled and measured plume scales could be achieved by increasing the model's vertical resolution.

However, a sensitivity test using two configurations of the HadGEM-UKCA global model that differed only in their description of convective scavenging, showed that improving the convective scavenging routine had an even greater impact on the simulated plume scales than model resolution. Therefore the disagreement between simulated and measured plumes may be due in part to a misrepresented aerosol process within the model. Further investigation of the impact of specific aerosol processes on simulated plume scales is required.

In the case of the HIPPO observations, it is unknown if the flight tracks were sampling the vertical component of larger-scale features or the horizontal extents of individual small-scale plumes or a combination of these two patterns. In the case of the model data, however, the flight-track-simulated plumes (FTS plumes) could be co-located to the 3D plumes through which they flew. The 3D plume analysis in Chapter 3 quantified the simulated horizontal and vertical scales of the three-dimensional plumes that were detected during the simulated HIPPO flights. This analysis showed that the FTS plumes were indeed sampling large-scale features multiple times. The horizontal scales of these 3D plumes were much larger than their vertical scales and the scales

of the FTS plumes, confirming that the FTS plumes were either sampling the vertical component or the internal variability of these larger-scale structures.

The identification of 3D plumes also enabled the investigation of the impact of increasing a model's resolution on three-dimensional plume scales. At the lowest model resolution, the average longitudinal scale was 1920 km and the average latitudinal scale was 1580 km. Doubling the horizontal resolution from low to baseline resulted in a 50% decrease in the average scales; doubling the horizontal resolution again from baseline to high resulted in a 30% decrease in the average horizontal scales. The smaller increase between baseline and high resolution could mean that the average horizontal scales of these BC plume structures are being resolved at the highest resolution. However, this needs to be verified by measurements that span large horizontal distances, such as satellite retrievals. Though most satellites have difficulty distinguishing aerosol type, aerosol optical depth could be used as a proxy for aerosol amount.

This chapter additionally investigated how model resolution affects black carbon variability in remote and near-source regions using two-dimensional autocorrelation analysis. This analysis showed that BC variability increases with increasing model resolution and that BC exhibits much higher variability near sources compared to the remote Pacific. This means that GCMs may have more difficulty representing BC in emission regions. The analysis also showed that BC variability was heavily influenced by the presence of plumes, confirming results from Chapter 2 which suggested that a large portion of observed BC variability can be accounted for by plume structures. The 2D autocorrelation functions of BC exhibited lower variability in Spring and Summer when high BC concentrations were distributed in large-scale plumes. The 2D autocorrelation functions also showed lower variability in the longitudinal direction, particularly in regions where large-scale BC plumes were spread out across the domain by longitudinal air flows. This again matches with the 3D plume analysis that showed 22 – 36% larger average longitudinal scales than latitudinal scales.

In summary, these results showed that the degree to which global climate models

resolve variability can have a significant impact on the scales of BC plumes. GCMs significantly overestimated the scales of along-flight-track variability; however, these scales were shown to be much smaller than the horizontal scales of the 3D plumes sampled by the flight track. Both the 3D plume scales and BC variability were significantly affected by model resolution; the degree to which GCMs accurately reproduce this variability requires further comparison to observations.

What processes contribute the most to aerosol variability?

Chapters 2 and 3 showed that aerosol variability exists on scales smaller than a global climate model grid box (100 km) and that increasing a model's resolution can have a significant impact on simulated variability. Furthermore, improving the description of an important aerosol process within a GCM was found to greatly affect simulated plumes scales. It is clear that in order to improve predictions of aerosols, models need to capture the scales of variability of important aerosol processes. This leads to the question: what processes contribute the most to aerosol variability?

To address this question, a novel technique was developed to simulate aerosol processes at varying resolutions while maintaining a constant resolution in all other fields. Past research has explored the effect of aerosol sub-grid variability by varying model resolution and evaluating the subsequent effect on aerosol fields. In these studies, aerosol fields are affected by changes in resolution of all model components, making it difficult to isolate and understand the impact of a particular aerosol process. The method presented in this thesis is able to separate the effect of neglecting sub-grid variability of aerosols from other sources of variability within the model. Chapter 4 implemented this technique in the regional-scale model WRF-Chem to quantify the effect of neglecting sub-grid aerosol variability on aerosol optical depth (AOD) and cloud condensation nuclei (CCN). The resolution of the aerosol and gaseous fields was varied from a 'high' resolution of 10 km to a 'low' resolution of 80 km, which represents an upper end resolution of current GCMs running climate simulations. The resolution

of the dynamics and meteorology was kept at a constant resolution of 10 km.

Decreasing the resolution of aerosols from 10 km to 80 km resulted in an underestimation of AOD by 13.1%. This was attributed to an underestimation in aerosol water content caused by less aerosol nitrate being distributed in the boundary layer in the low resolution run. Further investigation showed that neglecting aerosol variability strongly impacted the secondary production of aerosol nitrate due to the non-linear nature of the equilibrium reactions involved in its formation. Sensitivity tests showed that simply changing the degree of variability of the aerosol and gaseous species involved in the equilibrium can result in large differences in aerosol equilibrium concentrations. In addition to the non-linearities of the equilibrium system, convective transport was also found to have an impact on boundary layer concentrations of nitrate. This is likely due to the fact that in the aerosol averaged simulations, the high resolution mixing processes remove more low resolution aerosol, whose averaged fields are continuously being spread out over areas where aerosols have already been depleted (a full explanation can be found in Section 4.2.1). These results emphasise the importance of non-linearites associated with the simulation of aerosol water uptake. Because aerosol water content is usually a large contributor to total aerosol mass, small changes can have significant influences on aerosol optical depth. This study showed that neglecting aerosol variability can significantly alter the vertical profile of the aerosol composition, leading to measurable effects on aerosol water, and resultantly, AOD.

Neglecting the sub-grid variability of aerosols was also shown to impact simulations of CCN. Decreasing the resolution of aerosols from 10 km to 80 km resulted in an overestimation of CCN by 27.3%. This was caused by an overestimation in accumulation mode number concentration, which was the result of an increase in the nucleation rate leading to higher Aitken mode number concentrations and more growth into the accumulation mode. Non-linearities in gas-phase chemical reactions were found to be the source of the overestimation in the nucleation rate. Ozone production is less efficient at high concentrations; therefore, averaging the aerosol and gaseous fields over a lower

resolution grid increases the efficiency of ozone production. Higher concentrations of ozone lead to higher levels of OH, which increases the chemical production of sulphuric acid thereby increasing the rate of nucleation. Convective transport also played a role by lofting the gases to higher altitudes where gaseous production and nucleation are more efficient and gaseous lifetimes are longer. Without convective transport, the overestimation in OH and nucleation rate largely disappears.

These results show how changes in a seemingly unrelated process (e.g. ozone production) can lead to large differences in aerosol amounts, which can impact the climate system through their ability to act as CCN. The effects on both AOD and CCN highlight the sensitivity of chemical reactions and physical removal processes to aerosol sub-grid variability.

In summary, processes most affected by neglecting aerosol sub-grid variability are gas-phase chemistry and aerosol uptake of water through the aerosol/gas equilibrium reactions. The inherent non-linearities in these processes resulted in large changes in aerosol parameters when aerosol and gaseous species are artificially mixed over large spatial scales. These changes in aerosol and gas concentrations were exaggerated by convective transport, which transports these altered concentrations to altitudes where their effect is more pronounced.

How can we improve model simulations of aerosol variability?

The results from this thesis have provided insight into how we can improve model simulations of aerosol variability. It is important for models to capture the scales of aerosol plume structures, which account for a large degree of aerosol variability. Increasing a global climate model's vertical resolution may lead to improvement in the simulation of aerosol layers. Variability is higher near sources than in remote regions, indicating that models may benefit from higher resolutions in regions of high emissions. Additionally, GCMs at all resolutions showed higher variability in the latitudinal direction than the longitudinal direction, suggesting that capturing latitudinal variability may result in

greater improvements in aerosol modelling. While in practice these suggestions are difficult to implement in traditional grid-based models, much work has been done in developing adaptive grid, nesting, and stretched-grid models (see Future Work, Section 5.2.4). These results not only reveal important characteristics of aerosol variability, but can also be used to guide the development and implementation of variable-grid methods.

Improving the description of aerosol processes in GCMs also has a significant effect on aerosol variability and efforts should be focused on these improvements. In the case of the WRF-Chem simulations, processes that are found to be most affected by aerosol variability are non-linear chemical reactions and convective transport. Developing parameterisations that can handle or account for the effect of aerosol variability on these particular processes is essential for accurately predicting aerosol-radiation and aerosol-cloud interactions.

Aerosol water content is sensitive to changes in aerosol variability. While the effect of neglecting sub-grid variability on aerosol water content has been studied before, many previous studies have focused on the effects of the spatial resolution of relative humidity on calculated AOD [*Bian et al.*, 2009; *Haywood et al.*, 1997; *Pilinis et al.*, 1995]. It is clear from these past studies that neglecting the sub-grid variability of relative humidity can significantly impact aerosol water content. This thesis finds that aerosol composition can have just as large, if not larger, effect on aerosol water content; therefore it is important for future models to consider the effects of variability in both relative humidity and aerosol composition.

We have also seen that nitrate is likely to become a larger contributor to total aerosol mass in the future as emissions of sulphate decrease due to air pollution legislation. This study showed that small changes in overall nitrate concentrations can impact total AOD through its interaction with aerosol water content and that it is necessary to accurately simulate the vertical profile of nitrate, particularly in regions with high ammonia and nitric acid emissions. As an increasing number of global climate

models incorporate nitrate and its equilibrium system into their aerosol modelling schemes [*Myhre et al.*, 2013b], modellers must account for the fact that neglecting aerosol variability can result in large differences in equilibrium aerosol and gas concentrations. One possible method is to delay the timescale of the equilibrium to mimic greater mixing of aerosol and gaseous species. This method was tested by *Aan de Brugh et al.* [2012] in a single column model with promising results.

Additionally, non-linearities in gas-phase chemistry have been known to cause problems at lower model resolutions. Much work has been done on the issue of using global model resolutions in the modelling of gas-phase chemistry like ozone and OH production [e.g. *Sillman et al.*, 1990; *Jaeglé et al.*, 2001; *Wild and Prather*, 2006]; however, this problem is not usually addressed in terms of its effect on aerosol concentrations. Future modelling studies may benefit from a synthesis of these two approaches.

5.2 Future Work

5.2.1 Additional observational comparisons

As highlighted in the results from Chapter 3, while horizontal plume scales are significantly affected by increasing the model's horizontal resolution, it is not clear how these horizontal plume scales compare to observed horizontal plume scales due to the nature of the HIPPO flight track being unable to sample these large-scale features. An informative next step in this specific project is to use observations of aerosols from satellite retrievals for comparison to GCM output. There are several caveats to using satellite data that would have to be considered in the design of this study. One could use two-dimensional AOD data retrieved from the Moderate Resolution Imaging Spectrometer (MODIS) instrument, which would require altering the 3D plume detector to two dimensions. This also has the risk of combining distinct plumes at different altitudes into one larger plume, producing artificially large horizontal plume scales. Alternatively, one could use the lidar instrument CALIOP, which is able to

retrieve aerosol information in the vertical dimension but has a much narrower horizontal swath. This could be alleviated by sampling longer timescales in order to increase horizontal coverage. In both cases, as long as the model output and satellite data were sampled over the same spatial and temporal scales, comparisons between simulated and observed scales could be made.

Another option could be to use MACC reanalysis data, which is a combination of state-of-the-art atmospheric modelling data and Earth observational data. This dataset provides three-dimensional coverage of the globe at a higher resolution than GCMs and has been produced through assimilations of satellites and in situ observations.

This additional project would enable one to determine if the ECHAM horizontal plume scales are being resolved at the highest resolution, or if simulated plumes may benefit from further increases in GCM resolution.

5.2.2 Effect of aerosol processes on plume scales

In Chapter 3, improving the convective scavenging routine in HadGEM-UKCA had a large impact on the along-flight-track plume scales. This result can be taken a step further by testing the effect of different processes on three-dimensional plume scales. In *Kipling et al.* [*in prep*], the effect of turning off various aerosol processes on the vertical profile of black carbon was investigated. A similar analysis could be applied to the three-dimensional plume scales in order to determine which processes have the largest impact on the scales of aerosol variability and plumes in the atmosphere. One could deduce that processes with the largest impact would benefit most from a representation of sub-grid variability.

5.2.3 Regional differences in aerosol variability

In Chapter 4, the nitrate equilibrium system was found to have a significant impact on aerosol optical depth. This is likely influenced by the fact that the simulation was performed over a region with relatively high ammonia and nitric acid emissions. Correspondingly, many aerosol processes are likely to display regional dependencies. The results from this thesis could be further enhanced by additional analyses over regions that are characterised by different aerosol types and processes. For example, the results from simulations over the UK where nitrate concentrations are relatively high could be compared to a simulation over South America where biomass burning events are common; or over the Congo where there are strong aerosol-convection interactions; or over China where emissions of black carbon and other short-lived air pollutants are high. These additional simulations would provide insight into the regional differences in the processes that affect aerosol sub-grid variability.

5.2.4 Implications for future aerosol modelling

One of the major challenges to future modelling is determining how to account for the sub-grid variability of aerosol processes. The conclusions in Section 5.1 highlighted some important implications of the results presented in this thesis for the future of aerosol climate modelling. More details on how to guide model development in this area are provided below.

One solution to increasing a model's ability to simulate aerosol variability is to increase model resolution until aerosol plumes are sufficiently resolved. At this stage, increasing model resolution requires a huge computational cost and is not viable for many purposes, including long-term climate simulations of aerosols. New methods are being developed to run models with variable grid resolutions to target areas where sub-grid variability is significant. Using an adaptive grid or stretched grid is a relatively new concept where the resolution of the model is not constant over the model

domain but rather changes continuously and automatically to allow for more detailed simulations in particular regions. Another way to change a model's resolution in a particular area is through nested grids. In this type of simulation, the global model runs at a coarse resolution with a limited-area nested domain running at a higher resolution over a region of interest with boundary data supplied from the coarse global grid.

These types of model simulations are currently being actively developed. Results from this thesis provide insight into the regions where aerosol variability is highest and where increases in model resolution would be the most beneficial. Additionally, the technique applied in Chapter 4 which varies the resolution of aerosols separately from the rest of the model, is a useful technique for testing the scale dependency of particular aerosol processes, which is necessary for incorporating them into variable-grid models. Similar tests were performed on physics parameterisations in the study by [*Gustafson et al.*, 2013], who investigated the scale dependency of different cloud microphysics schemes.

Another solution to increasing a model's ability to simulate aerosol variability is to account for sub-grid variability through parameterisations. The introductory chapter highlighted some of the current work in this area, including plume-in-grid simulations and using probability distribution functions (PDF) to account for emission heterogeneity and other aerosol processes. The results from Chapter 4 demonstrated that neglecting the sub-grid variability of processes such as gas-phase reactions, nucleation, aerosol water uptake, and convective transport can have significant effects on aerosol parameters and that development of parameterisations that account for sub-grid variability should focus on these processes. The plume-in-grid method has been previously applied to ozone chemistry in regional-scale models and shown to improve simulated ozone concentrations. Results from this thesis suggest that not only could this method improve prediction of gaseous concentrations, it could also be extended to evaluate the effect of improved gas emissions on nucleation rates to determine if the plume-in-grid

technique leads to improved CCN concentrations.

Other studies have focused on the importance of capturing emission heterogeneity and have developed parameterisations to attempt to account for sub-grid scale heterogeneity of aerosol and gaseous emissions using PDFs. These techniques may be useful in modelling secondary nitrate production, which was shown to be highly sensitive to the emission heterogeneity of its precursor gases.

This section provides a few examples of techniques currently being used to account for aerosol variability. The results from this thesis have increased our understanding of the underlying mechanisms most affected by sub-grid variability and can help guide future development of these methods.

Bibliography

Aan de Brugh, J. M. J., J. S. Henzing, M. Schaap, W. T. Morgan, C. C. van Heerwaarden, E. P. Weijers, H. Coe, and M. C. Krol, Modelling the partitioning of ammonium nitrate in the convective boundary layer, *Atmospheric Chemistry and Physics*, *12*(6), 3005–3023, doi:10.5194/acp-12-3005-2012, 2012.

Ackermann, I., H. Hass, M. Memmesheimer, A. Ebel, F. Binkowski, and U. Shankar, Modal aerosol dynamics model for Europe: Development and first applications, *Atmospheric Environment*, *32*(17), 2981–2999, doi:10.1016/S1352-2310(98)00006-5, 1998.

Adams, P. J., J. H. Seinfeld, D. Koch, L. Mickley, and D. Jacob, General circulation model assessment of direct radiative forcing by the sulfate-nitrate-ammonium-water inorganic aerosol system, *Journal of Geophysical Research: Atmospheres*, *106*(D1), 1097–1111, doi: 10.1029/2000JD900512, 2001.

Albrecht, B., Aerosols, cloud microphysics, and fractional cloudiness, *Science*, *245*(4923), 1227–1230, doi:10.1126/science.245.4923.1227, 1989.

Anderson, T. L., R. J. Charlson, D. M. Winker, J. A. Ogren, and K. Holmen, Mesoscale variations of tropospheric aerosols, *Journal of the Atmospheric Sciences*, *60*(1), 119–136, 2003.

Asmi, A., et al., Number size distributions and seasonality of submicron particles in Europe 2008-2009, *Atmospheric Chemistry and Physics*, *11*(11), 5505–5538, doi:10.5194/acp-11-5505-2011, 2011.

Barmpadimos, I., J. Keller, D. Oderbolz, C. Hueglin, and A. S. H. Prevot, One decade of parallel fine (PM2.5) and coarse (PM10-PM2.5) particulate matter measurements in Europe: trends and variability, *Atmospheric Chemistry and Physics*, *12*(7), 3189–3203, doi:10.5194/acp-12-3189-2012, 2012.

Benkovitz, C. M., and S. E. Schwartz, Evaluation of modeled sulfate and SO2 over North America and Europe for four seasonal months in 1986-1987, *Journal of Geophysical Research-Atmospheres*, *102*(D21), 25,305–25,338, 1997.

Benkovitz, C. M., C. M. Berkowitz, R. C. Easter, S. Nemesure, R. Wagener, and S. E. Schwartz, Sulfate over the North Atlantic and adjacent continental regions: Evaluation for October and November 1986 using a three-dimensonal model driven by observation-derived meteorology, *Journal of Geophysical Research: Atmospheres*, *99*(D10), 20,725–20,756, doi:10.1029/94JD01634, 1994.

Bian, H., M. Chin, J. M. Rodriguez, H. Yu, J. E. Penner, and S. Strahan, Sensitivity of aerosol optical thickness and aerosol direct radiative effect to relative humidity, *Atmospheric Chemistry and Physics*, *9*(7), 2375–2386, doi:10.5194/acp-9-2375-2009, 2009.

Bond, T. C., et al., Bounding the role of black carbon in the climate system: A scientific assessment, *Journal of Geophysical Research: Atmospheres*, *118*(11), 5380–5552, doi:10.1002/jgrd.50171, 2013.

Boucher, O., et al., Clouds and aerosols, in *Climate Change 2007: The Physical Science Basis. Contribution of Working Group I to the Fourth Assessment Report of the Intergovernmental Panel on Climate Change*, edited by T. F. Stocker, D. Qin, G.-K. Plattner, M. Tignor, S. K. Allen, J. Boschung, A. Nauels, Y. Xia, V. Bex, and P. M. Midgley, chap. 7, Cambridge University Press, 2013.

Bourgeois, Q., and I. Bey, Pollution transport efficiency toward the Arctic: Sensitivity to aerosol scavenging and source regions, *Journal of Geophysical Research: Atmospheres*, *116*(D8), doi:10.1029/2010JD015096, 2011.

Brink, H., J. Veefkind, A. Waijers-Ijpelaan, and J. van der Hage, Aerosol light-scattering in The Netherlands, *Atmospheric Environment*, *30*(24), 4251–4261, doi:10.1016/1352-2310(96)00091-X, 1996.

Brock, C. A., et al., Characteristics, sources, and transport of aerosols measured in spring 2008 during the aerosol, radiation, and cloud processes affecting arctic climate (ARCPAC) project, *Atmospheric Chemistry and Physics*, *11*(6), 2423–2453, doi:10.5194/acp-11-2423-2011, 2011.

Brook, J. R., A. H. Wiebe, S. A. Woodhouse, C. V. Audette, T. F. Dann, S. Callaghan, M. Piechowski, E. DabekZlotorzynska, and J. F. Dloughy, Temporal and spatial relationships in fine particle strong acidity, sulphate, PM10 and PM2.5 across multiple Canadian locations, *Atmospheric Environment*, *31*(24), 4223–4236, doi:10.1016/S1352-2310(97)00248-3, 1997.

Brunner, D., et al., An evaluation of the performance of chemistry transport models by comparison with research aircraft observations. Part 1: Concepts and overall model performance, *Atmospheric Chemistry and Physics*, *3*, 1609–1631, 2003.

Cakmur, R. V., R. L. Miller, and O. Torres, Incorporating the effect of small-scale circulations upon dust emission in an atmospheric general circulation model, *Journal of Geophysical Research: Atmospheres*, *109*(D7), D07,201, doi:10.1029/2003JD004067, 2004.

Cameron, M. A., M. Z. Jacobson, A. D. Naiman, and S. K. Lele, Effects of plume-scale versus grid-scale treatment of aircraft exhaust photochemistry, *Geophysical Research Letters*, *40*(21), 5815–5820, doi:10.1002/2013GL057665, 2013.

Cassiani, M., J. F. Vinuesa, S. Galmarini, and B. Denby, Stochastic fields method for sub-grid scale emission heterogeneity in mesoscale atmospheric dispersion models, *Atmospheric Chemistry and Physics*, *10*(1), 267–277, doi:10.5194/acp-10-267-2010, 2010.

Chen, F., and J. Dudhia, Coupling an advanced land surface-hydrology model with the Penn State-NCAR MM5 modeling system. Part I: Model implementation and sensitivity, *Monthly Weather Review*, *129*(4), 569–585, doi:10.1175/1520-0493(2001)129⟨0569:CAALSH⟩2.0.CO;2, 2001.

Chou, M., and M. Suarez, An efficient thermal infrared radiation parameterization for use in general circulation models, *Tech. Rep. 104606*, NASA Tech. Memorandum, 1994.

Christensen, M. W., and G. L. Stephens, Microphysical and macrophysical responses of marine stratocumulus polluted by underlying ships: Evidence of cloud deepening, *Journal of Geophysical Research: Atmospheres*, *116*(D3), D03,201, doi:10.1029/2010JD014638, 2011.

Costabile, F., W. Birmili, S. Klose, T. Tuch, B. Wehner, A. Wiedensohler, U. Franck, K. König, and A. Sonntag, Spatio-temporal variability and principal components of the particle number size distribution in an urban atmosphere, *Atmospheric Chemistry and Physics*, *9*(9), 3163–3195, doi:10.5194/acp-9-3163-2009, 2009.

Cross, E., et al., Soot particle studies instrument inter-comparison project overview, *Aerosol Science and Technology*, *44*(8), 592–611, doi:10.1080/02786826.2010.482113, 2010.

Cusack, M., N. Prez, J. Pey, A. Wiedensohler, A. Alastuey, and X. Querol, Variability of sub-micrometer particle number size distributions and concentrations in the Western Mediterranean regional background, *Tellus B*, *65*(0), 2013.

Daher, N., S. Hasheminassab, M. M. Shafer, J. J. Schauer, and C. Sioutas, Seasonal and spatial variability in chemical composition and mass closure of ambient ultrafine particles in the megacity of Los Angeles, *Environ. Sci.: Processes Impacts*, *15*, 283–295, doi:10.1039/C2EM30615H, 2013.

Dentener, F., et al., Emissions of primary aerosol and precursor gases in the years 2000 and 1750 prescribed data-sets for AeroCom, *Atmospheric Chemistry and Physics*, *6*(12), 4321–4344, doi:10.5194/acp-6-4321-2006, 2006.

Derksen, J., G.-J. Roelofs, R. Otjes, G. de Leeuw, and T. Rckmann, Impact of ammonium nitrate chemistry on the AOT in Cabauw, the Netherlands, *Atmospheric Environment*, *45*(31), 5640 – 5646, doi:10.1016/j.atmosenv.2011.02.052, 2011.

Diehl, T., A. Heil, M. Chin, X. Pan, D. Streets, M. Schultz, and S. Kinne, Anthropogenic, biomass burning, and volcanic emissions of black carbon, organic carbon, and SO_2 from 1980 to 2010 for hindcast model experiments, *Atmospheric Chemistry and Physics Discussions*, *12*(9), 24,895–24,954, doi:10.5194/acpd-12-24895-2012, 2012.

Eilers, P., A perfect smoother, *Analytical Chemistry*, *75*(14), 3631–3636, doi:10.1021/ac034173t, 2003.

Esler, J. G., G. J. Roelofs, M. O. Köhler, and F. M. O'Connor, A quantitative analysis of grid-related systematic errors in oxidising capacity and ozone production rates in chemistry transport models, *Atmospheric Chemistry and Physics*, *4*(7), 1781–1795, doi:10.5194/acp-4-1781-2004, 2004.

Fast, J. D., J. Gustafson, William I., R. C. Easter, R. A. Zaveri, J. C. Barnard, E. G. Chapman, G. A. Grell, and S. E. Peckham, Evolution of ozone, particulates, and aerosol direct radiative forcing in the vicinity of Houston using a fully coupled meteorology-chemistry-aerosol model, *Journal of Geophysical Research-Atmospheres*, *111*(D21), D21,305, doi:10.1029/2005JD006721, 2006.

Galmarini, S., J.-F. Vinuesa, and A. Martilli, Modeling the impact of sub-grid scale emission variability on upper-air concentration, *Atmospheric Chemistry and Physics*, *8*(2), 141–158, doi:10.5194/acp-8-141-2008, 2008.

Ganzeveld, L., J. Lelieveld, and G.-J. Roelofs, A dry deposition parameterization for sulfur oxides in a chemistry and general circulation model, *Journal of Geophysical Research: Atmospheres*, *103*(D5), 5679–5694, doi:10.1029/97JD03077, 1998.

Garcia-Menendez, F., A. Yano, Y. Hu, and M. T. Odman, An adaptive grid version of CMAQ for improving the resolution of plumes, *Atmospheric Pollution Research*, *1*(4), 239–249, 2010.

Garrett, T. J., C. Zhao, and P. C. Novelli, Assessing the relative contributions of transport efficiency and scavenging to seasonal variability in Arctic aerosol, *Tellus B*, *62*(3), 190–196, doi:10.1111/j.1600-0889.2010.00453.x, 2010.

Generoso, S., F.-M. Bréon, Y. Balkanski, O. Boucher, and M. Schulz, Improving the seasonal cycle and interannual variations of biomass burning aerosol sources, *Atmospheric Chemistry and Physics*, *3*(4), 1211–1222, doi:10.5194/acp-3-1211-2003, 2003.

Gerard, L., An integrated package for subgrid convection, clouds and precipitation compatible with meso-gamma scales, *Quarterly Journal of the Royal Meteorological Society*, *133*(624), 711–730, doi:10.1002/qj.58, 2007.

Girard, E., and B. Bekcic, Sensitivity of an Arctic regional climate model to the horizontal resolution during winter: implications for aerosol simulation, *International Journal of Climatology*, *25*(11), 1455–1471, doi:10.1002/joc.1205, 2005.

Grell, G., and D. Devenyi, A generalized approach to parameterizing convection combining ensemble and data assimilation techniques, *Geophysical Research Letters*, *29*(14), 1693, doi:10.1029/2002GL015311, 2002.

Grell, G., S. Peckham, R. Schmitz, S. McKeen, G. Frost, W. Skamarock, and B. Eder, Fully coupled online chemistry within the WRF model, *Atmospheric Environment*, *39*(37), 6957–6975, doi:10.1016/j.atmosenv.2005.04.027, 2005.

Guenther, A., P. Zimmerman, and M. Wildermuth, Natural volatile organic-compound emission rate estimates for united-states woodland landscapes, *Atmospheric Environment*, *28*(6), 1197–1210, doi:10.1016/1352-2310(94)90297-6, 1994.

Gustafson, J., W. I., Y. Qian, and J. D. Fast, Downscaling aerosols and the impact of neglected subgrid processes on direct aerosol radiative forcing for a representative global climate model gird spacing, *Journal of Geophysical Research*, *116*(D13), 2011.

Gustafson, W. I., P.-L. Ma, H. Xiao, B. Singh, P. J. Rasch, and J. D. Fast, The Separate Physics and Dynamics Experiment (SPADE) framework for determining resolution awareness: A case study of microphysics, *Journal of Geophysical Research: Atmospheres*, *118*(16), 9258–9276, doi:10.1002/jgrd.50711, 2013.

Harrison, R. M., D. Laxen, S. Moorcroft, and K. Laxen, Processes affecting concentrations of fine particulate matter (PM2.5) in the UK atmosphere, *Atmospheric Environment*, *46*, 115–124, doi:10.1016/j.atmosenv.2011.10.028, 2012.

Haywood, J., and O. Boucher, Estimates of the direct and indirect radiative forcing due to tropospheric aerosols: A review, *Reviews of Geophysics*, *38*(4), 513–543, doi:10.1029/1999RG000078, 2000.

Haywood, J. M., V. Ramaswamy, and L. J. Donner, A limited-area-model case study of the effects of sub-grid scale variations in relative humidity and cloud upon the direct radiative forcing of sulfate aerosol, *Geophysical Research Letters*, *24*(2), 143–146, doi: 10.1029/96GL03812, 1997.

Held, I., and M. Suarez, A proposal for the intercomparison of the dynamical cores of atmospheric general circulation models, *Bulletin of the American Meteorological Society*, *75*, 1994.

Hewitt, H. T., D. Copsey, I. D. Culverwell, C. M. Harris, R. S. R. Hill, A. B. Keen, A. J. McLaren, and E. C. Hunke, Design and implementation of the infrastructure of HadGEM3: the next-generation Met Office climate modelling system, *Geoscientific Model Development*, *4*(2), 223–253, doi:10.5194/gmd-4-223-2011, 2011.

Hidy, G. M., Surface-level ne particle mass concentrations: from hemispheric distributions to megacity sources, *Journal of Air Waste Management Association*, *59*, 770–789, 2009.

Holzer, M., T. Hall, and R. Stull, Seasonality and weather-driven variability of transpacific transport, *Journal of Geophysical Research-Atmospheres*, *110*(D23), D23,103, doi: 10.1029/2005JD006261, 2005.

Hong, S.-Y., Y. Noh, and J. Dudhia, A new vertical diffusion package with an explicit treatment of entrainment processes, *Monthly Weather Review*, *134*(9), 2318–2341, doi: 10.1175/MWR3199.1, 2006.

Jacobson, M., and J. Seinfeld, Evolution of nanoparticle size and mixing state near the point of emission, *Atmospheric Environment*, *38*(13), 1839–1850, doi:10.1016/j.atmosenv.2004.01.014, 2004.

Jaeglé, L., D. J. Jacob, W. H. Brune, and P. O. Wennberg, Chemistry of HOx radicals in the upper troposphere, *Atmospheric Environment*, *35*(3), 469 – 489, doi:10.1016/S1352-2310(00)00376-9, 2001.

Jimenez, J. L., et al., Evolution of organic aerosols in the atmosphere, *Science*, *326*(5959), 1525–1529, doi:10.1126/science.1180353, 2009.

Jobson, B., S. McKeen, D. Parrish, F. Fehsenfeld, D. Blake, A. Goldstein, S. Schauffler, and J. Elkins, Trace gas mixing ratio variability versus lifetime in the troposphere and stratosphere: Observations, *Journal of Geophysical Research-Atmospheres*, *104*(D13), 16,091–16,113, doi:10.1029/1999JD900126, 1999.

Junge, C., Residence time and variability of tropospheric trace gases, *Tellus*, *26*(4), 477–488, 1974.

Karamchandani, P., C. Seigneur, K. Vijayaraghavan, and S. Y. Wu, Development and application of a state-of-the-science plume-in-grid model, *Journal of Geophysical Research-Atmospheres*, *107*(D19), 4403, doi:10.1029/2002JD002123, 2002.

Karamchandani, P., K. Vijayaraghavan, S.-Y. Chen, C. Seigneur, and E. Edgerton, Plume-in-grid modeling for particulate matter, *Atmospheric Environment*, *40*(38), 7280–7297, doi:10.1016/j.atmosenv.2006.06.033, 2006.

Kazil, J., et al., Aerosol nucleation and its role for clouds and earth's radiative forcing in the aerosol-climate model ECHAM5-HAM, *Atmospheric Chemistry and Physics*, *10*(22), 10,733–10,752, doi:10.5194/acp-10-10733-2010, 2010.

Kiliyanpilakkil, V. P., and N. Meskhidze, Deriving the effect of wind speed on clean marine aerosol optical properties using the A-Train satellites, *Atmospheric Chemistry and Physics*, *11*(22), 11,401–11,413, doi:10.5194/acp-11-11401-2011, 2011.

Kinne, S., et al., An AeroCom initial assessment of optical properties in aerosol component modules of global models, *Atmospheric Chemistry and Physics*, *6*(7), 1815–1834, doi:10.5194/acp-6-1815-2006, 2006.

Kipling, Z., P. Stier, J. P. Schwarz, A. E. Perring, J. R. Spackman, G. W. Mann, C. E. Johnson, and P. J. Telford, Constraints on aerosol processes in climate models from vertically-resolved aircraft observations of black carbon, *Atmospheric Chemistry and Physics*, *13*(12), 5969–5986, doi:10.5194/acp-13-5969-2013, 2013.

Kipling, Z., et al., What controls the vertical distribution of aerosol? Relationships between process sensitivity in HadGEM3–UKCA and inter-model variation from AeroCom Phase II, in prep.

Klich, C. A., and H. E. Fuelberg, The role of horizontal model resolution in assessing the transport of CO in a middle latitude cyclone using WRF-Chem, *Atmospheric Chemistry and Physics*, *14*(2), 609–627, doi:10.5194/acp-14-609-2014, 2014.

Koch, D., and A. D. Del Genio, Black carbon semi-direct effects on cloud cover: review and synthesis, *Atmospheric Chemistry and Physics*, *10*(16), 7685–7696, doi:10.5194/acp-10-7685-2010, 2010.

Koch, D., et al., Evaluation of black carbon estimations in global aerosol models, *Atmospheric Chemistry and Physics*, *9*(22), 9001–9026, 2009.

Kohler, H., The nucleus in and the growth of hygroscopic droplets, *Trans. Faraday Soc.*, *32*, 1152–1161, doi:10.1039/TF9363201152, 1936.

Kulmala, M., T. Vesala, and P. Wagner, An analytical expression for the rate of binary condensational particle growth: Comparison with numerical results, *Journal of Aerosol Science*, *23, Supplement 1*(0), 133–136, doi:10.1016/0021-8502(92)90367-5, 1992.

Kulmala, M., A. Laaksonen, and L. Pirjola, Parameterizations for sulfuric acid/water nucleation rates, *Journal of Geophysical Research: Atmospheres*, *103*(D7), 8301–8307, doi:10.1029/97JD03718, 1998.

Kulmala, M., H. Vehkamki, T. Petj, M. D. Maso, A. Lauri, V.-M. Kerminen, W. Birmili, and P. McMurry, Formation and growth rates of ultrafine atmospheric particles: a review of observations, *Journal of Aerosol Science*, *35*(2), 143–176, doi:10.1016/j.jaerosci.2003.10.003, 2004.

Kumar, T. K., H. Gadhavi, A. Jayaraman, M. S. Suman, and S. V. B. Rao, Temporal and spatial variability of aerosol optical depth over south india as inferred from MODIS, *Journal of Atmospheric and Solar-Terrestrial Physics*, *94*(0), 71–80, doi:10.1016/j.jastp.2012.12.010, 2013.

Lamarque, J.-F., et al., Historical (1850–2000) gridded anthropogenic and biomass burning emissions of reactive gases and aerosols: methodology and application, *Atmospheric Chemistry and Physics*, *10*(15), 7017–7039, doi:10.5194/acp-10-7017-2010, 2010.

Lee, S., Effect of aerosol on circulations and precipitation in deep convective clouds, *Journal of the Atmospheric Sciences*, *69*(6), 1957–1974, doi:10.1175/JAS-D-11-0111.1, 2012.

Leung, L., and S. Ghan, A subgrid parameterization of orographic precipitation, *Theoretical and Applied Climatology*, *52*(1-2), 95–118, doi:10.1007/BF00865510, 1995.

Lin, S.-J., and R. B. Rood, Multidimensional flux-form semi-Langrangian transport schemes, *Monthly Weather Review*, *124*, 2046–2070, doi:10.1175/1520-0493(1996)124⟨2046:MFFSLT⟩2.0.CO;2, 1996.

Lin, Y., R. Farley, and H. Orville, Bulk parameterization of the snow field in a cloud model, *Journal of Climate and Applied Meteorology*, *22*(6), 1065–1092, doi:10.1175/1520-0450(1983)022⟨1065:BPOTSF⟩2.0.CO;2, 1983.

Liu, H., D. Jacob, I. Bey, R. Yantosca, B. Duncan, and G. Sachse, Transport pathways for Asian pollution outflow over the Pacific: Interannual and seasonal variations, *Journal of Geophysical Research-Atmospheres*, *108*(D20), 8786, doi:10.1029/2002JD003102, 2003.

Mann, G. W., K. S. Carslaw, D. V. Spracklen, D. A. Ridley, P. T. Manktelow, M. P. Chipperfield, S. J. Pickering, and C. E. Johnson, Description and evaluation of GLOMAP-mode: a modal global aerosol microphysics model for the UKCA composition-climate model, *Geoscientific Model Development*, *3*(2), 651–734, doi:10.5194/gmdd-3-651-2010, 2010.

Marcella, M. P., and E. A. B. Eltahir, Effects of mineral aerosols on the summertime climate of southwest Asia: Incorporating subgrid variability in a dust emission scheme, *Journal of Geophysical Research: Atmospheres*, *115*(D18), doi:10.1029/2010JD014036, 2010.

Matsui, H., et al., Spatial and temporal variations of aerosols around Beijing in summer 2006: Model evaluation and source apportionment, *Journal of Geophysical Research: Atmospheres*, *114*(D2), doi:10.1029/2008JD010906, 2009.

McComiskey, A., and G. Feingold, The scale problem in quantifying aerosol indirect effects, *Atmospheric Chemistry and Physics*, *12*(2), 1031–1049, doi:10.5194/acp-12-1031-2012, 2012.

McKeen, S. A., E.-Y. Hsie, M. Trainer, R. Tallamraju, and S. C. Liu, A regional model study of the ozone budget in the eastern United States, *Journal of Geophysical Research: Atmospheres*, *96*(D6), 10,809–10,845, doi:10.1029/91JD00052, 1991.

Metzger, S., F. Dentener, M. Krol, A. Jeuken, and J. Lelieveld, Gas/aerosol partitioning 2. Global modeling results, *Journal of Geophysical Research: Atmospheres*, *107*(D16), 17–1–17–23, doi:10.1029/2001JD001103, 2002.

Mlawer, E., S. Taubman, P. Brown, M. Iacono, and S. Clough, Radiative transfer for inhomogeneous atmospheres: RRTM, a validated correlated-k model for the longwave, *Journal of Geophysical Research-Atmospheres*, *102*(D14), 16,663–16,682, doi:10.1029/97JD00237, 1997.

Monin, A. S., and A. M. Obukhov, Basic laws of turbulent mixing in the surface layer of the atmosphere, *Tr. Akad. Nauk SSSR Geofiz Inst*, *24*, 163–187, 1954.

Moteki, N., and Y. Kondo, Dependence of laser-induced incandescence on physical properties of black carbon aerosols: Measurements and theoretical interpretation, *Aerosol Science and Technology*, *44*(8), 663–675, doi:10.1080/02786826.2010.484450, 2010.

Myhre, G., J. E. Jonson, J. Bartnicki, F. Stordal, and K. P. Shine, Role of spatial and temporal variations in the computation of radiative forcing due to sulphate aerosols: A regional study, *Quarterly Journal of the Royal Meteorological Society*, *128*(581), 973–989, doi:10.1256/0035900021643610, 2002.

Myhre, G., C. Myhre, B. H. Samset, and T. Storelvmo, Aerosols and their relation to global climate sensitivity, *Nature Education Knowledge*, *4*(5), 2013a.

Myhre, G., et al., Radiative forcing of the direct aerosol effect from AeroCom Phase II simulations, *Atmospheric Chemistry and Physics*, *13*(4), 1853–1877, doi:10.5194/acp-13-1853-2013, 2013b.

Nicolas, J., E. Yubero, C. Pastor, J. Crespo, and A. Carratala, Influence of meteorological variability upon aerosol mass size distribution, *Atmospheric Research*, *94*(2), 330–337, doi:10.1016/j.atmosres.2009.06.007, 2009.

O'Connor, F. M., G. D. Carver, N. H. Savage, J. A. Pyle, J. Methven, S. R. Arnold, K. Dewey, and J. Kent, Comparison and visualisation of high-resolution transport modelling with aircraft measurements, *Atmospheric Science Letters*, *6*(3), 164–170, doi:10.1002/asl.111, 2005.

O'Connor, F. M., et al., Evaluation of the new UKCA climate-composition model – Part 2: The troposphere, *Geoscientific Model Development*, *7*(1), 41–91, doi:10.5194/gmd-7-41-2014, 2014.

Petroff, A., and L. Zhang, Development and validation of a size-resolved particle dry deposition scheme for application in aerosol transport models, *Geoscientific Model Development*, *3*(2), 753–769, doi:10.5194/gmd-3-753-2010, 2010.

Pierce, J. R., G. Theodoritsi, P. J. Adams, and S. N. Pandis, Parameterization of the effect of sub-grid scale aerosol dynamics on aerosol number emission rates, *Journal of Aerosol Science*, *40*(5), 385–393, doi:10.1016/j.jaerosci.2008.11.009, 2009.

Pilinis, C., S. N. Pandis, and J. H. Seinfeld, Sensitivity of direct climate forcing by atmospheric aerosols to aerosol size and composition, *Journal of Geophysical Research: Atmospheres*, *100*(D9), 18,739–18,754, doi:10.1029/95JD02119, 1995.

Putaud, J. ., et al., A European aerosol phenomenology-3: Physical and chemical characteristics of particulate matter from 60 rural, urban, and kerbside sites across Europe, *Atmospheric Environment*, *44*(10), 1308–1320, doi:10.1016/j.atmosenv.2009.12.011, 2010.

Qian, Y., J. Gustafson, W. I., and J. D. Fast, An investigation of the sub-grid variability of trace gases and aerosols for global climate modeling, *Atmospheric Chemistry and Physics*, *10*(14), 6917–6946, doi:10.5194/acp-10-6917-2010, 2010.

Ram, K., M. M. Sarin, and S. N. Tripathi, A 1 year record of carbonaceous aerosols from an urban site in the Indo-Gangetic Plain: Characterization, sources, and temporal variability, *Journal of Geophysical Research: Atmospheres*, *115*(D24), doi:10.1029/2010JD014188, 2010.

Ramanathan, V., and G. Carmichael, Global and regional climate changes due to black carbon, *Nature Geoscience*, *1*(4), 221–227, doi:10.1038/ngeo156, 2008.

Redemann, J., et al., Suborbital measurements of spectral aerosol optical depth and its variability at subsatellite grid scales in support of CLAMS 2001, *Journal of the Atmospheric Sciences*, *62*(4), 993–1007, 2005.

Ridley, D. A., C. L. Heald, J. R. Pierce, and M. J. Evans, Toward resolution-independent dust emissions in global models: Impacts on the seasonal and spatial distribution of dust, *Geophysical Research Letters*, *40*(11), 2873–2877, doi:10.1002/grl.50409, 2013.

Riemer, N., and M. West, Quantifying aerosol mixing state with entropy and diversity measures, *Atmospheric Chemistry and Physics*, *13*(6), 15,615–15,662, doi:10.5194/acpd-13-15615-2013, 2013.

Riipinen, I., et al., Organic condensation: a vital link connecting aerosol formation to cloud condensation nuclei (CCN) concentrations, *Atmospheric Chemistry and Physics*, *11*(8), 3865–3878, doi:10.5194/acp-11-3865-2011, 2011.

Robles González, C., M. Schaap, G. de Leeuw, P. J. H. Builtjes, and M. van Loon, Spatial variation of aerosol properties over Europe derived from satellite observations and comparison with model calculations, *Atmospheric Chemistry and Physics*, *3*(3), 521–533, doi:10.5194/acp-3-521-2003, 2003.

Rodriguez, S., et al., A study on the relationship between mass concentrations, chemistry and number size distribution of urban fine aerosols in Milan, Barcelona and London, *Atmospheric Chemistry and Physics*, *7*(9), 2217–2232, 2007.

Roeckner, E., et al., The atmospheric general circulation model ECHAM5. Part I: Model description, *Report 349*, Max Planck Institute for Meteorology, Hamburg, Germany, 2003.

Roelofs, G.-J., H. ten Brink, A. Kiendler-Scharr, G. de Leeuw, A. Mensah, A. Minikin, and R. Otjes, Evaluation of simulated aerosol properties with the aerosol-climate model echam5-ham using observations from the impact field campaign, *Atmospheric Chemistry and Physics*, *10*(16), 7709–7722, doi:10.5194/acp-10-7709-2010, 2010.

Rosenfeld, D., U. Lohmann, G. B. Raga, C. D. O'Dowd, M. Kulmala, S. Fuzzi, A. Reissell, and M. O. Andreae, Flood or drought: How do aerosols affect precipitation?, *Science*, *321*(5894), 1309–1313, doi:10.1126/science.1160606, 2008.

Sandu, I., J.-L. Brenguier, O. Geoffroy, O. Thouron, and V. Masson, Aerosol impacts on the diurnal cycle of marine stratocumulus, *Journal of the Atmospheric Sciences*, *65*(8), 2705–2718, doi:10.1175/2008JAS2451.1, 2008.

Sardar, S. B., P. M. Fine, and C. Sioutas, Seasonal and spatial variability of the size-resolved chemical composition of particulate matter (PM10) in the Los Angeles Basin, *Journal of Geophysical Research: Atmospheres*, *110*(D7), doi:10.1029/2004JD004627, 2005.

Saxena, P., A. B. Hudischewskyj, C. Seigneur, and J. H. Seinfeld, A comparative study of equilibrium approaches to the chemical characterization of secondary aerosols, *Atmospheric Environment*, *20*(7), 1471–1483, doi:10.1016/0004-6981(86)90019-3, 1986.

Schell, B., I. Ackermann, H. Hass, F. Binkowski, and A. Ebel, Modeling the formation of secondary organic aerosol within a comprehensive air quality model system, *Journal of Geophysical Research-Atmospheres*, *106*(D22), 28,275–28,293, doi:10.1029/2001JD000384, 2001.

Schulz, M., et al., Radiative forcing by aerosols as derived from the AeroCom present-day and pre-industrial simulations, *Atmospheric Chemistry and Physics*, *6*, 5225–5246, 2006.

Schwartz, S. E., Sulphate aerosols and climate, *Nature*, *340*(6234), 515–516, doi:10.1038/340515b0, 1989.

Schwarz, J. P., J. R. Spackman, R. S. Gao, L. A. Watts, P. Stier, M. Schulz, S. M. Davis, S. C. Wofsy, and D. W. Fahey, Global-scale black carbon profiles observed in the remote atmosphere and compared to models, *Geophysical Research Letters*, *37*, L23,804, doi:10.1029/2010GL046007, 2010a.

Schwarz, J. P., et al., Single-particle measurements of midlatitude black carbon and light-scattering aerosols from the boundary layer to the lower stratosphere, *Journal of Geophysical Research-Atmospheres*, *111*(D16), D16,207, doi:10.1029/2006JD007076, 2006.

Schwarz, J. P., et al., The detection efficiency of the single particle soot photometer, *Aerosol Science and Technology*, *44*(8), 612–628, doi:10.1080/02786826.2010.481298, 2010b.

Seinfeld, J. H., and S. N. Pandis, *Atmospheric Chemistry and Physics*, Wiley, 2006.

Shaw, W. J., K. J. Allwine, B. G. Fritz, F. C. Rutz, J. P. Rishel, and E. G. Chapman, An evaluation of the wind erosion module in DUSTRAN, *Atmospheric Environment*, *42*(8), 1907–1921, doi:10.1016/j.atmosenv.2007.11.022, 2008.

Shinozuka, Y., and J. Redemann, Horizontal variability of aerosol optical depth observed during the ARCTAS airborne experiment, *Atmospheric Chemistry and Physics*, *11*(16), 8489–8495, doi:10.5194/acp-11-8489-2011, 2011.

Shinozuka, Y., A. D. Clarke, S. G. Howell, V. N. Kapustin, C. S. McNaughton, J. Zhou, and B. E. Anderson, Aircraft profiles of aerosol microphysics and optical properties over North America: Aerosol optical depth and its association with PM2.5 and water uptake, *Journal of Geophysical Research: Atmospheres*, *112*(D12), doi:10.1029/2006JD007918, 2007.

Shiraiwa, M., Y. Kondo, N. Moteki, N. Takegawa, L. K. Sahu, A. Takami, S. Hatakeyama, S. Yonemura, and D. R. Blake, Radiative impact of mixing state of black carbon aerosol in Asian outflow, *Journal of Geophysical Research: Atmospheres*, *113*(D24), doi:10.1029/2008JD010546, 2008.

Sillman, S., J. A. Logan, and S. C. Wofsy, A regional scale model for ozone in the United States with subgrid representation of urban and power plant plumes, *Journal of Geophysical Research: Atmospheres*, *95*(D5), 5731–5748, doi:10.1029/JD095iD05p05731, 1990.

Skamarock, W. C., and J. B. Klemp, A time-split nonhydrostatic atmospheric model for weather research and forecasting applications, *Journal of Computational Physics*, *227*(7), 3465–3485, doi:10.1016/j.jcp.2007.01.037, 2008.

Skamarock, W. C., J. B. Klemp, M. G. Duda, L. D. Fowler, S.-H. Park, and T. D. Ringler, A multiscale nonhydrostatic atmospheric model using centroidal voronoi tesselations and C-grid staggering, *Monthly Weather Review*, *140*(9), 3090–3105, doi: 10.1175/MWR-D-11-00215.1, 2012.

Slinn, W., Predictions for particle deposition to vegetative canopies, *Atmospheric Environment (1967)*, *16*(7), 1785–1794, doi:10.1016/0004-6981(82)90271-2, precipitation chemistry, 1982.

Slowik, J., et al., An inter-comparison of instruments measuring black carbon content of soot particles, *Aerosol Science and Technology*, *41*(3), 295–314, doi:10.1080/02786820701197078, 2007.

Snyder, D., A. P. Rutter, C. Worley, M. Olson, A. Plourde, R. Bader, T. Dallmann, and J. Schauer, Spatial variability of carbonaceous aerosols and associated source tracers in two cites in the midwestern United States, *Atmospheric Environment*, *44*(13), 1597–1608, doi:10.1016/j.atmosenv.2010.02.004, 2010.

Solomon, S., D. Qin, M. Manning, Z. Chen, M. Marquis, K. B. Averyt, M. Tignor, and H. Miller (Eds.), *Climate Change 2007: The Physical Science Basis. Contribution of Working Group I to the Fourth Assessment Report of the Intergovernmental Panel on Climate Change*, Cambridge University Press, 2007.

Spracklen, D. V., K. S. Carslaw, M. Kulmala, V.-M. Kerminen, G. W. Mann, and S.-L. Sihto, The contribution of boundary layer nucleation events to total particle concentrations on regional and global scales, *Atmospheric Chemistry and Physics*, *6*(12), 5631–5648, doi: 10.5194/acp-6-5631-2006, 2006.

Squizzato, S., M. Masiol, E. Innocente, E. Pecorari, G. Rampazzo, and B. Pavoni, A procedure to assess local and long-range transport contributions to PM2.5 and secondary inorganic aerosol, *Journal of Aerosol Science*, *46*, 64–76, doi:10.1016/j.jaerosci.2011.12.001, 2012.

Stevens, B., et al., Atmospheric component of the MPI-M Earth System Model: ECHAM6, *Journal of Advances in Modeling Earth Systems*, *5*(2), 146–172, doi:10.1002/jame.20015, 2013.

Stickel, J., Data smoothing and numerical differentiation by a regularization method, *Computers & Chemical Engineering*, *34*(4), 467–475, doi:10.1016/j.compchemeng.2009.10.007, 2010.

Stier, P., J. H. Seinfeld, S. Kinne, J. Feichter, and O. Boucher, Impact of nonabsorbing anthropogenic aerosols on clear-sky atmospheric absorption, *Journal of Geophysical Research-Atmospheres*, *111*(D18), D18,201, doi:10.1029/2006JD007147, 2006.

Stier, P., et al., The aerosol-climate model ECHAM5-HAM, *Atmospheric Chemistry and Physics*, *5*, 1125–1156, 2005.

Stockman, G., and L. G. Shapiro, *Computer Vision*, 1st ed., Prentice Hall PTR, Upper Saddle River, NJ, USA, 2001.

Stockwell, W., P. Middleton, J. Chang, and X. Tang, The 2nd generation regional acid deposition model chemical mechanism for regional air-quality modeling, *Journal of Geophysical Research-Atmospheres*, *95*(D10), 16,343–16,367, doi:10.1029/JD095iD10p16343, 1990.

Stohl, A., Characteristics of atmospheric transport into the Arctic troposphere, *Journal of Geophysical Research-Atmospheres*, *111*(D11), D11,306, doi:10.1029/2005JD006888, 2006.

Stroud, C. A., et al., Impact of model grid spacing on regional- and urban- scale air quality predictions of organic aerosol, *Atmospheric Chemistry and Physics*, *11*(7), 3107–3118, doi:10.5194/acp-11-3107-2011, 2011.

Stuart, G. S., R. G. Stevens, A.-I. Partanen, A. K. L. Jenkins, H. Korhonen, P. M. Forster, D. V. Spracklen, and J. R. Pierce, Reduced efficacy of marine cloud brightening geoengineering due to in-plume aerosol coagulation: parameterization and global implications, *Atmospheric Chemistry and Physics*, *13*(20), 10,385–10,396, doi:10.5194/acp-13-10385-2013, 2013.

Targino, A. C., K. J. Noone, and E. Ostrom, Airborne in situ characterization of dry aerosol optical properties in a multisource influenced marine region, *Tellus Series B-Chemical and Physical Meteorology*, *57*(3), 247–260, 2005.

Telford, P. J., N. L. Abraham, A. T. Archibald, P. Braesicke, M. Dalvi, O. Morgenstern, F. M. O'Connor, N. A. D. Richards, and J. A. Pyle, Implementation of the Fast-JX Photolysis scheme (v6.4) into the UKCA component of the MetUM chemistry-climate model (v7.3), *Geoscientific Model Development*, *6*(1), 161–177, doi:10.5194/gmd-6-161-2013, 2013.

Textor, C., et al., Analysis and quantification of the diversities of aerosol life cycles within AeroCom, *Atmospheric Chemistry and Physics*, *6*, 1777–1813, 2006.

Textor, C., et al., The effect of harmonized emissions on aerosol properties in global models – an AeroCom experiment, *Atmospheric Chemistry and Physics*, *7*(17), 4489–4501, doi:10.5194/acp-7-4489-2007, 2007.

Thornhill, D. A., et al., Spatial and temporal variability of particulate polycyclic aromatic hydrocarbons in Mexico City, *Atmospheric Chemistry and Physics*, *8*(12), 3093–3105, 2008.

Twomey, S., Pollution and planetary albedo, *Atmospheric Environment*, *8*(12), 1251–1256, doi:10.1016/0004-6981(74)90004-3, 1974.

van der Gon, H. D., J. Kuenen, and T. Butler, A Base Year (2005) MEGAPOLI Global Gridded Emission Inventory (1st Version). Deliverable D1., *MEGAPOLI Scientific Report 10-13*, 2010.

van der Werf, G. R., J. T. Randerson, L. Giglio, G. J. Collatz, P. S. Kasibhatla, and J. Arellano, A. F., Interannual variability in global biomass burning emissions from 1997 to 2004, *Atmospheric Chemistry and Physics*, *6*, 3423–3441, 2006.

Venkatachari, P., L. M. Zhou, P. K. Hopke, D. Felton, O. V. Rattigan, J. J. Schwab, and K. L. Demerjian, Spatial and temporal variability of black carbon in New York City, *Journal of Geophysical Research-Atmospheres*, *111*(D10), doi:10.1029/2005JD006314, 2006.

Vignati, E., J. Wilson, and P. Stier, M7: An efficient size-resolved aerosol microphysics module for large-scale aerosol transport models, *Journal of Geophysical Research: Atmospheres*, *109*(D22), 2156–2202, doi:10.1029/2003JD004485, 2004.

Vinken, G. C. M., K. F. Boersma, D. J. Jacob, and E. W. Meijer, Accounting for non-linear chemistry of ship plumes in the GEOS-Chem global chemistry transport model, *Atmospheric Chemistry and Physics*, *11*(22), 11,707–11,722, doi:10.5194/acp-11-11707-2011, 2011.

von Hardenberg, J., L. Vozella, C. Tomasi, V. Vitale, A. Lupi, M. Mazzola, T. P. C. van Noije, A. Strunk, and A. Provenzale, Aerosol optical depth over the Arctic: a comparison of ECHAM-HAM and TM5 with ground-based, satellite and reanalysis data, *Atmospheric Chemistry and Physics*, *12*(15), 6953–6967, doi:10.5194/acp-12-6953-2012, 2012.

Wainwright, C. D., J. R. Pierce, J. Liggio, K. B. Strawbridge, A. M. Macdonald, and R. W. Leaitch, The effect of model spatial resolution on Secondary Organic Aerosol predictions: a case study at Whistler, BC, Canada, *Atmospheric Chemistry and Physics*, *12*(22), 10,911–10,923, doi:10.5194/acp-12-10911-2012, 2012.

Walters, M., Comments on "the differentiation between grid spacing and resolution and their application to numerical modeling", *Bulletin of the American Meteorological Society*, *81*(10), 2475–2477, doi:10.1175/1520-0477(2000)081⟨2475:CAACOT⟩2.3.CO;2, 2000.

Wang, M., et al., The multi-scale aerosol-climate model PNNL-MMF: model description and evaluation, *Geoscientific Model Development*, *4*(1), 137–168, doi:10.5194/gmd-4-137-2011, 2011.

Warneke, C., et al., Biomass burning in Siberia and Kazakhstan as an important source for haze over the Alaskan Arctic in April 2008, *Geophysical Research Letters*, *36*, L02,813, doi:10.1029/2008GL036194, 2009.

Weigum, N. M., P. Stier, J. P. Schwarz, D. W. Fahey, and J. R. Spackman, Scales of variability of black carbon plumes over the Pacific Ocean, *Geophysical Research Letters*, *39*(15), 15,804, doi:10.1029/2012GL052127, 2012.

Wesely, M., Parameterization of surface resistances to gaseous dry deposition in regional-scale numerical-models, *Atmospheric Environment*, *23*(6), 1293–1304, doi:10.1016/0004-6981(89)90153-4, 1989.

Wild, O., and M. J. Prather, Global tropospheric ozone modeling: Quantifying errors due to grid resolution, *Journal of Geophysical Research: Atmospheres*, *111*(D11), doi:10.1029/2005JD006605, 2006.

Wild, O., X. Zhu, and M. Prather, Fast-j: Accurate simulation of in- and below-cloud photolysis in tropospheric chemical models, *Journal of Atmospheric Chemistry*, *37*(3), 245–282, doi:10.1023/A:1006415919030, 2000.

Williamson, D., Convergence of atmospheric simulations with increasing horizontal resolution and fixed forcing scales, *Tellus A*, *51*(5), 663–673, 1999.

Xu, L., and J. E. Penner, Global simulations of nitrate and ammonium aerosols and their radiative effects, *Atmospheric Chemistry and Physics*, *12*(20), 9479–9504, doi:10.5194/acp-12-9479-2012, 2012.

Zhang, K., et al., The global aerosol-climate model ECHAM-HAM, version 2: Sensitivity to improvements in process representations, *Atmospheric Chemistry and Physics Discussions*, *12*(3), 7545–7615, doi:10.5194/acpd-12-7545-2012, 2012.

Zhang, L., S. Gong, J. Padro, and L. Barrie, A size-segregated particle dry deposition scheme for an atmospheric aerosol module, *Atmospheric Environment*, *35*(3), 549 – 560, doi: 10.1016/S1352-2310(00)00326-5, 2001.

Zhang, Q., et al., Ubiquity and dominance of oxygenated species in organic aerosols in anthropogenically-influenced Northern Hemisphere midlatitudes, *Geophysical Research Letters*, *34*(13), doi:10.1029/2007GL029979, 2007.

Zhang, R., A. Khalizov, J. Pagels, D. Zhang, H. Xue, and P. McMurry, Variability in morphology, hygroscopicity, and optical properties of soot aerosols during atmospheric processing, *Proceedings of the National Academy of Sciences of the United States of America*, *105*(30), 10,291–10,296, doi:10.1073/pnas.0804860105, 2008.